The volatile contents of melt inclusions and implications for mantle degassing and ocean island evolution

Lowell Moore

Dissertation submitted to the faculty of the Virginia Polytechnic Institute and State University in partial fulfillment of the requirements for the degree of

Doctor of Philosophy
In
Geosciences

Robert J. Bodnar, Chair
Esteban Gazel
Mark J. Caddick
Megan S. Duncan

July 25, 2019
Blacksburg, VA

Keywords: Volatiles, Volcanoes, Melt inclusions, Mantle plumes

The volatile contents of melt inclusions and implications for mantle degassing and ocean island evolution

Lowell Moore

ABSTRACT

The amount of volatile elements dissolved in silicate melts is a controlling factor in a range of geologic processes, which include hazardous volcanic eruptions, economically-significant ore-forming systems, and global-scale volatile fluxes, which contribute to planetary evolution. While melt volatile contents are important, estimating the origin and fate of volatiles distributed within magmas is challenging because volatiles exsolve from the melt during eruption and are transferred into the atmosphere. Therefore, the stratigraphic record of volcanic and intrusive deposits does not contain direct information regarding the pre-eruptive volatile content of the melt. However, melt inclusions trapped within growing phenocrysts present an opportunity to sample the melt before it has completely degassed. Analysis of melt inclusions is challenging owing to a range of processes which occur after the melt inclusion is trapped and which overprint the original texture and composition of the inclusion at the time of entrapment. Thus, efforts to accurately determine the current composition of the melt inclusion sample and then infer the original composition of the trapped melt which that inclusion represents require a combination of microanalytical, numerical, and/or experimental methods.

In **Chapter 1**, we present a pedagogical approach for estimating the processes that affect the CO_2 content of a magma from its origin during melting a C-bearing source material to its exsolution into a free fluid phase during crystallization and degassing. In **Chapter 2**, we explore different experimental, microanalytical, and numerical methods which may be used to estimate the CO_2 contents of melt inclusions that contain fluid bubbles and describe the advantages and disadvantages of each approach. In **Chapter 3**, we apply some of the methods discussed in the previous chapters to estimate the pre-eruptive volatile content of Haleakala Volcano (Maui) and assess different melting mechanisms that may be active in the Hawaiian plume.

The volatile contents of melt inclusions and implications for mantle degassing and ocean island evolution

Lowell Moore

GENERAL AUDIENCE ABSTRACT

Volcanoes are features which form on the Earth's surface and are located above regions where material melts tens of kilometers (or more) below the surface. The process of melting is studied through laboratory experimentation, and therefore it is possible to estimate the composition of deep subsurface material based on the compositions of volcanic rocks which can be sampled on the Earth's surface. This sub-discipline of geologic research is called "igneous petrology."

A fundamental problem in igneous petrology is estimating the volatile content of the Earth's deep interior. Volatile elements are those elements such as hydrogen and carbon, which are stable as gasses in the atmosphere rather than in the mineral components of a rock. It is thought that the gasses produced from volcanic vents, of which the compositions are well known, represent volatile elements which were originally present as dissolved components in the melt. Experiments performed on volcanic rocks have demonstrated that volatile elements can be dissolved in melts at high pressures corresponding to depths within the Earth's crust, and these elements exsolve from the melt when it approaches the surface -- similar to how CO_2 can be dissolved in a carbonated beverage, which bubbles out when the beverage is opened.

The only geologically-persistent features which preserves the pre-eruptive volatile content of a melt (i.e. how much gas was dissolved before eruption) are droplets of melt which are accidentally trapped within crystals that grow from the melt as it cools near the Earth's surface -- these are called "melt inclusions." While melt inclusions are useful in this regard, they are challenging to apply to geologic problems because they undergo a range of physical and chemical changes after they are trapped, which can alter their composition from the original composition of the melt that was trapped.

This dissertation concerns the theory used to infer how volatile elements are distributed within the deep Earth, analytical and numerical methods used to gather

relevant information from melt inclusion samples, and an application of these methods to investigate the volatile content of the mantle below Hawaii. **Chapter 1** describes a framework for systematically determining the amount of CO_2 distrubuted within a given volcanic setting. **Chapter 2** compares different methods used to estimate the original volatile content of melt inclusions from Kamchatka, which have formed fluid bubbles -- a common feature present in melt inclusions. **Chapter 3** applies the methods described in the first two chapters to estimate how volatile elements are distributed within the Earth's mantle below Hawaii, and how the process of melting transfers them to the Earth's atmosphere.

Acknowledgements

This dissertation was made possible by the presence of a wonderful community of friends and scholars, and I owe them all a debt of gratitude. Many thanks go to my main advisors, Bob and Esteban, who provided a steady supply of mentorship, ideas, constructive criticism, and financial support since I arrived in Blacksburg. I also wish to thank the graduate students in the VT Department of Geosciences, who are unanimously pleasant, insightful, and entertaining. I consider myself lucky to have had the opportunity to share in their friendship and knowledge during my time at Virginia Tech.

In the last few years, I have also had the privilege to travel to many different laboratories and academic conferences, which gave me the opportunity to become acquainted with an "extended family" of colleagues from all over the Earth – a mixture of fluid inclusionists, volcanologists, and petrologists. In particular, I would like to thank Paul Wallace, Glenn Gaetani, Terry Plank, Maria Luce Frezzotti, Nobu Shimizu, Jay Thomas, Charles Farley, Luca Fedele, Brian Monteleone, and Will Nachlas for their sage advice and access to some of the best microanalytical facilities in the world.

Finally, I want to thank my fiancée, Kaysha Perrin, for agreeing to move to Blacksburg with me so that I could pursue a PhD in Geology. Without her, none of my academic work would exist, and I would probably be spending my days trying to sell beets on the side of the road.

Attributions

This dissertation includes the collaborative work of my co-authors and peer reviewers who contributed to these chapters which appear or are expected to appear as articles in peer-reviewed journals.

Chapter 1 was published as Moore, L.R., Bodnar, R.J. (2019) "A Pedagogical Approach to Estimating the CO_2 Budget of Magmas. Journal of the Geological Society," DOI: https://doi.org/10.1144/jgs2018-094, published online January 2019. ***L.R. Moore*** was responsible for designing and presenting example calculations, and writing and preparation the manuscript. *R.J. Bodnar* contributed to preparation and editing of the manuscript.

Chapter 2 was published as Moore, L.R., Mironov, N., Portnyagin, M., Gazel, E., Bodnar, R.J. (2018) "Volatile contents of primitive bubble-bearing melt inclusions from Klyuchevskoy volcano, Kamchatka: Comparison of volatile contents determined by mass-balance versus experimental homogenization," Journal of Volcanology and Geothermal Research, 358, 124-131. ***L.R. Moore*** was responsible for preparing and analyzing melt inclusion samples, data interpretation and presentation, and writing the manuscript. *N. Mironov* and *M. Portnyagin* provided sample material and contributed to data interpretation and editing of the manuscript. *E. Gazel* and *R.J. Bodnar* contributed to data interpretation and editing and preparation of the manuscript.

Chapter 3 has been submitted for publication in the journal *Geochimica et Cosmochimica Acta* as Moore, L.R., Gazel, E., Ballmer, M., Bodnar, R.J., "The volatile budget of Hawaiian magmatism: constraints from melt inclusions from Haleakala Volcano, East Maui, Hawaii." ***L.R. Moore*** was responsible for preparation and analysis of melt inclusion and whole rock samples, data interpretation and presentation, numerical modeling, and writing and preparation of the manuscript. *E. Gazel* collected and described samples in the field, contributed to data interpretation and presentation, and assisted in editing and preparing the manuscript. *M. Ballmer* was responsible for geodynamic modeling and interpretation and contributed to writing and editing the manuscript. *R.J. Bodnar* contributed to editing and preparation of the manuscript.

Table of contents

Introduction

Determining the degassing behavior of magmas is an exciting geochemical challenge. Volcanic explosions occur when gaseous components dissolved in the melt exsolve to create a voluminous and fragmented volcanic foam, and the explosivity of volcanic eruptions is in part linked to the initial concentration of volatile components in the melt. Life on Earth and (potentially) other planets depends on the presence and composition of fluids at the Earth's surface, and a thorough understanding of the life-mediating factors of a planetary system requires some knowledge of the magnitude and rate of volcanic degassing. Finally, the economic value represented by certain ore deposits depends on the efficiency with which metals can be concentrated within the fluids exsolved from a degassing magma, and information about the degassing process is necessary for determining the genesis of certain classes of ore deposit.

While the volatile content of a magma is a controlling factor in multiple petrologic processes, estimating the magnitude and rate of change of this parameter is challenging because volatile elements tend not to remain in the stratigraphy of volcanic deposits, with essentially all of the original volatile element budget transferred into the atmosphere. For this reason, most of our knowledge about volcanic degassing comes from field and remote sensing measurements of volcanic plumes and fumaroles at active volcanic settings. In volcanic settings that are no longer active, volatile contents of melts may be estimated using inclusions of melt and/or the exsolving fluid, which are trapped within crystals growing below the volcanic edifice. In an ideal case, an early-forming mineral, such as olivine, may trap a small aliquot (10s to 100s of microns in diameter) of melt before it begins to degas, and if this melt inclusion is quenched to a glass upon eruption, the composition of the glass may be used to represent the composition of the undegassed melt.

Melt inclusions typically contain a mixture of solid and fluid phases, which may have been trapped as a mixture, or which may consist of phases that have nucleated within the inclusion after trapping a homogeneous melt. Particles commonly found within melt inclusions may include a glassy matrix, silicate minerals, fluid bubbles, immiscible liquid globules, and mineral rims or condensates along phase boundaries. Therefore, the

composition of the melt that was originally trapped by the inclusion is represented by the integrated composition of all phases present within the inclusion (assuming that no mass transfer into or out of the inclusion occurred after trapping).

The primary goals of the research described in this dissertation are to describe some of the processes which transfer volatile elements (C in particular) from the deep Earth (upper mantle and lithosphere) to the surface and to constrain the rates of volatile transfer when possible. However, because the processes that affect the manner in which pre-eruptive melts are preserved in the melt inclusion record are still not well understood, a major subsidiary goal of this dissertation is to describe and evaluate the strengths and weaknesses of melt inclusion-related methodologies as well as approaches for estimating the volatile budget of a magma. To this end, the chapters of this dissertation are separated into a practical framework for estimating magma volatile budgets, a comparative assessment of different methods for determining the volatile budgets of melt inclusion samples, and a study which applies these techniques to estimate the volatile budget of the Hawaiian plume.

Chapter 1 of this dissertation describes a simplified pedagogical approach for estimating the CO_2 budget of a magma using combined information from whole rock, melt inclusion, and field measurements/remote sensing data. This CO_2 budget is conceptualized as a simple model where CO_2 enters the magma when a C-bearing source material partially melts. As the melt cools and decompresses, the CO_2 concentration of the melt increases due to crystallization of C-free silicate minerals and decreases due to exsolution of a CO_2-bearing fluid phase, and the latter process can be modeled quantitatively using experimentally-determined volatile-melt solubility relationships. Finally, the flux of CO_2 from the melt can be calculated based on the discharge rate of melt during ascent and the concentration of CO_2 in the melt estimated from the petrologic (melt inclusion) record, and the petrologically-determined CO_2 flux can thus be directly compared to a CO_2 fluxes determined using field sampling methods applied to the volcanic plume.

Chapter 2 of this dissertation compares volatile contents of primitive, bubble-bearing melt inclusions estimated using microanalytical, experimental, and numerical approaches. In the microanalytical approach, fluid and glass phases in the melt inclusion

are analyzed separately, and then a mass balance calculation is used to determine the total bulk CO_2 content of the inclusion. In the experimental approach, melt inclusions are heated to dissolve daughter phases (including bubbles) into the melt and then quenched into a single homogenous phase from which the total CO_2 content can be measured directly. In the numerical approach, the amount of CO_2 in melt inclusion bubble is calculated from the analyzed major element and volatile concentration of the glass and the composition of the host mineral. In general, the experimental method is more precise but requires more effort and resources, and the numerical and microanalytical approaches are less precise but require less effort and fewer resources.

Chapter 3 of this dissertation describes a study in which melt inclusions from fresh monogenetic cinder cones on Haleakala Volcano (Maui) were used to estimate how the volatile budget of melts from the Hawaiian hotspot differ during island evolution stages. Melt inclusions were analyzed using some of the microanalytical methods discussed in Chapter 2, and were found to contain up to ~1.3 wt% CO_2 and ~1.2 wt% H_2O, which indicate a range of trapping pressures from 5-7 kbar. Based on consistency with numerical crystal fractionation models, inclusions likely trapped melts which were derived from a primary melt containing approximately 7000 ppm H_2O and at least 7000 ppm CO_2, and which experienced 15-45% fluid-saturated polybaric fractional crystallization before melt inclusions were trapped. Because of the likelihood that melt inclusions trapped a partially degassed melt, volatile/trace element ratios (e.g. CO_2/Ba, H_2O/Ce) were used to suggest that the source volatile concentration of the Shield stage may be enriched in H_2O and CO_2 relative to the Post-shield stage. If this is the case, then it implies that the melting process associated with the post-shield stage preferentially melts material from the volatile-rich periphery of the plume.

Chapter 1: A Pedagogical Approach to Estimating the CO_2 Budget of Magmas

Abstract

On a planetary scale, the carbon cycle describes the movement of carbon between the atmosphere and the deep earth. Carbon species are involved in diverse Earth processes, ranging from sedimentary, metamorphic and igneous petrology to the long-term viability of life at the Earth's surface. Volcanoes, and their associated magmatic systems, represent the interface through which carbon is transferred from the deep earth to the surface. Thus, quantifying the CO_2 budget of volcanic systems is necessary for understanding the deep carbon cycle and, concomitantly, the CO_2 budget of the near surface, including the atmosphere. In this review, Kilauea volcano (Hawaii) is used as a case study to illustrate simple calculations that can account for processes that affect the amount and distribution of CO_2 in this relatively well-studied volcanic system. These processes include methods to estimate the concentration of CO_2 in a melt derived by partial melting of a source material, enrichment of CO_2 in the melt during fractional crystallization, exsolution of CO_2 from a fluid-saturated melt, trapping and post-entrapment modification of melt inclusions, and outgassing from the volcanic edifice. Our goal in this review is to provide straightforward example calculations that can be used to derive first-order estimates regarding processes that control the CO_2 budgets of magmas and which can be incorporated into global carbon cycle models.

Introduction

There is much interest today in the global carbon cycle and linkages between the various carbon reservoirs that extend from the deep mantle to the atmosphere. Much of the approximately 175 Mt of carbon per year (Burton et al., 2013) that is currently transferred from the Earth's interior to the surface is a result of magmatic and volcanic activity. Carbon dissolved in melts is transported towards the surface by ascending magmas and most of the dissolved carbon, in the form of CO_2, is eventually lost to the atmosphere as a result of degassing as magmas approach the surface (Figure 1). Accordingly, the CO_2 budgets of magmas provide constraints on the rate at which CO_2 is transferred from the solid earth to the atmosphere. Determining the CO_2 budgets of active, degassing volcanic systems is relatively straightforward and provides information concerning the mechanisms and magnitudes of fluid exsolution and outgassing today. However,

much less is known about CO_2 budgets and outgassing behavior in extinct or dormant volcanic systems, and such information is needed to better understand the style of past volcanic eruptions and volatiles such as CO_2 have important implications for ore-forming and other metasomatic processes. Developing a better understanding of magma CO_2 budgets may also advance our understanding of the extent to which volcanic processes have modulated the climate and contributed to global weathering, ocean acidity, and habitability of the Earth's surface in the past.

This review, and the reviews of Chiodini et al. (2018) and Allard et al. (2018), describes the processes that transfer carbon from the deep earth to the exosphere in active volcanic settings. Here, we quantify the path that carbon follows from a melting mantle source to exsolution from the melt into the atmosphere or preservation in the geologic record, with example calculations based on the CO_2 budget of the active Kilauea volcano (Hawaii). We selected Kilauea because it is well studied and is in a steady state of relatively continuous open-system degassing that permits comparison between observations of the volcanic plume and the petrology of erupted material (e.g. Gerlach et al., 2002). Specifically, these example calculations follow the processes of 1) melting a carbon-bearing source material, 2) melt evolution during fractional crystallization, volatile saturation, and exsolution of CO2 into a separate fluid phase (degassing), and finally 3) mass transfer of the exsolved carbon-bearing fluid into the atmosphere (outgassing).

Generation of CO_2 from the source region: Batch melting

Carbon is partitioned into the melt phase when a C-bearing source material melts, either in the mantle or in the crust. Carbon may occur in the melt as a variety of species, including CO, CO_2, or CO_3^{2-}, depending on the temperature and oxygen fugacity of the melt (Ni & Keppler, 2013). Usually, the total carbon concentration in the bulk mantle and in the melt generated by partial melting is expressed in terms of CO_2 abundance or concentration, and we will use this convention in this example. The source material may include mixtures of nominally anhydrous endmember lithologies (e.g., peridotite, pyroxenite, eclogite) with most of the C contained in accessory mineral phases (e.g., carbonates, graphite, diamond). Estimates of the average CO_2 concentration in the mantle vary from 10s of ppm (Trull et al., 1993; Canil et al., 1994) to 1000s of ppm (Javoy & Pineau, 1991) or higher (Luth, 1999).

As a first approximation, batch melting simulations can be used to relate the composition of the source material to the composition of the melt produced, provided that the degree of melting and bulk partition coefficient of the element(s) of interest are known or can be determined. The bulk partition coefficient is determined as a weighted average based on the proportions of each mineral comprising the source material, combined with experimentally-

determined mineral-melt partition coefficients for each element. Experimentally-determined mineral-melt partition coefficients relevant to various mantle lithologies are available in Salters et al. (2002), Rollinson (2014), White (2013), among others, and in online databases such as the GERM database (earthref.org/KDD). Using trace element partitioning data, the trace element composition of the melt is often used to constrain the melt fraction. However, it should be noted that the partitioning of elements between the source material and primary melt can vary with melt composition and thermodynamic conditions (temperature, pressure, oxygen fugacity, etc.) during melting. Therefore, because multiple factors can affect the partitioning behavior of elements during melting, the results of batch melting calculations can be model-dependent and poorly constrained. For more information regarding strategies for estimating the conditions of melting, the reader is referred to White (2013) and Rollinson (2014).

The batch melting equation is often expressed as a ratio,

$$\frac{C_L}{C_0} = \frac{1}{D(1-F)+F} \quad (1)$$

where C_L and C_0 are the concentrations of a component in the primary melt and source material, respectively, D is the bulk partition coefficient of the component, and F is the melt fraction. Note that as F approaches 1, C_L approaches C_0, which represents the endmember case in which complete melting of the source would produce a melt with a composition identical to that of the source material (Figure 2).

From melting experiments over a range of melt compositions, CO_2 has been found to behave as a highly incompatible element (e.g. Rosenthal et al., 2016). Therefore, when calculating the CO_2 concentration in a crystallizing primary melt below Kilauea, the mineral-melt partition coefficient D can be considered to be arbitrarily small. Therefore, we can apply the simplifying assumption that $\frac{C_L}{C_0}$ approaches $\frac{1}{F}$ as D approaches 0 because CO_2 behaves as a highly incompatible element and is partitioned into the melt phase during melting. The trace element compositions of Hawaiian shield lavas such as those erupted at Kilauea are consistent with ~4-15% melting (e.g., Dixon et al., 2008), so we can use an average value of $F = 0.1$ in our calculations. Estimates of the primary CO_2 concentration in Hawaiian melts vary from thousands of ppm to ~2 wt% (Gerlach et al., 2002; Dixon & Clague, 2001), and we use $C_L = 1\ wt\%$ (10,000 ppm) in this example. With these parameters specified and the simplifying assumptions described above, the calculated bulk CO_2 concentration in the source material is given by:

$$C_0 = C_L \times F = 1\ wt\% \times 0.1 = 0.1\ wt\% = 1000\ ppm$$

In addition to the challenges associated with constraining the conditions of melting described above, an additional limitation of the batch melting approach described above is that it assumes that all minerals in the source melt in proportions equal to their modal abundance (modal melting). If non-modal melting occurs, it is necessary to determine the proportion of each mineral phase that melts (Rollinson, 2014). For example, it is likely that carbonate minerals in the mantle source preferentially melt early in the melting process to produce a more CO_2-rich melt than would be predicted for modal-melting, and the effects of melting carbonated peridotite source are not well known (Dasgupta et al., 2007; Dasgupta et al., 2013). Furthermore, in the case of preferential melting of C-rich accessory minerals, the distinction between the breakdown of carbonate accessory minerals to produce a CO_2-rich melt and low degrees of partial melting to produce a carbonatite melt may not exist (Wirth & Rocholl, 2003; Frezzotti & Peccerillo, 2007). To compensate for these uncertainties, Dixon et al. (2008) used a mixture of nominally anhydrous lherzolite and carbonatite as a source composition (C_0) rather than a modal melting calculation to calculate the composition of alkaline lavas erupted in Hawaii's north arch (C_L), which likely melted a source material enriched in C. This is in contrast to the center of the plume where Kilauea is located and where incorporation of volatile-enriched material in the source region is less likely (Dixon & Clague, 2001).

Fractionation of CO_2 in melts: crystallization and degassing

The CO_2 concentration in the melt phase that migrates from the source region towards the surface is controlled by two competing processes: volatile exsolution and fractional crystallization. As the melt ascends from the region of melting and pressure decreases, the melt may reach fluid saturation and exsolve a CO_2-rich fluid. The loss of this CO_2 from the melt leads to a lower CO_2 concentration in the melt. If the melt stalls during ascent and begins to cool, removal of silicate and other components from the melt by crystallization of silicate and oxide phases (e.g., olivine, spinel, pyroxene) will lead to an increase in the concentration of CO_2 and other volatiles, which are generally more compatible in the residual melt than in crystallizing (non-carbonate) minerals. Distinguishing which of these two processes exerts the strongest control on the volatile

content of the melt is challenging, and this is especially true for CO_2 owing to its relatively low solubility in silicate melts at crustal pressures (Stolper & Holloway, 1988). While it may not be possible to predict with certainty the manner in which the CO_2 content will change as the melt crystallizes, degasses, and erupts, different samples representing different stages in melt evolution may preserve a record of the volatile content of melts as they evolve. For example, fluid (Miranov & Portnyagin, 2011; Oligialoro et al. 2018) and melt inclusions (Mironov et al., 2015) may record evidence of early degassing processes, while whole rock and matrix glass samples preserve a record of late degassing and fractional crystallization processes (Dixon & Clague, 2001; Lloyd et al., 2016). Thus, in order to constrain the volatile evolution of a degassing, crystallizing magma, it is necessary to consider information preserved by various geologic materials produced from the same overall eruptive event.

Fractional Crystallization

As a melt cools during its ascent from its source region, minerals may begin to crystallize from the melt. In the case of a silicate melt crystallizing silicate (non-carbonate) minerals, the degree of CO_2 enrichment in the melt phase resulting from fractional crystallization can be calculated using the Raleigh Law. Similar to the batch melting equation, the change in melt concentration is expressed as a ratio

$$\frac{C_f}{C_i} = F^{D-1} \tag{2}$$

where F is the fraction of melt remaining following crystallization of a fraction $(1 - F)$ of its total mass, and C_i and C_f are the initial and final concentrations of a component in the liquid (melt) after crystallization has occurred. Similar to the batch melting equation, the mineral-melt partition coefficient D is equal to the ratio of the concentrations of a component in the mineral and melt phases. Estimating the degree of crystallization of a primary melt is relatively straightforward when only a single phase is crystallizing, and this is likely the case for some of the more primitive basaltic melts at Kilauea in which only olivine is crystallizing. In this case, the amount of melt that has crystallized to produce olivine can be determined iteratively by adding olivine to the melt until it is in equilibrium with the melting mantle source (e.g. 90 mole percent

forsterite). For more information concerning strategies to evaluate the effects of crystallization on melt composition, the reader is referred to White (2013) and Rollinson (2014).

Similar to the previous example, the CO_2 concentration in a crystallizing primary melt below Kilauea can be estimated by assuming that the mineral-melt partition coefficient D is an arbitrarily small value (i.e., CO_2 remains in the melt phase) such that $\frac{C_f}{C_i}$ approaches F^{-1} (Figure 3). To determine the CO_2 concentration in a melt from Kilauea after some amount of fractional crystallization, we assume $F = 80\%$ for this example, i.e., 20% of the melt has crystallized (e.g. Anderson & Brown, 1993). Starting with a primary melt containing 1 wt% CO_2 from the previous example, 20% olivine crystallization would yield a melt with a CO_2 concentration of

$$C_f = 1\ wt\% \times 0.8^{-1} = 1.25\ \text{wt}\%$$

Even under conditions in which a basaltic primary melt is crystallizing only olivine, estimating the extent of crystallization is not trivial. The composition of olivine that is crystallizing is a function of both the oxygen fugacity of the melt and the melt composition, and the amount of crystallization $(1 - F)$ that is predicted depends on these parameters (e.g. Sobolev et al., 2005; Dixon et al., 2008; Matzen et al., 2011). For more evolved melt compositions in which several minerals are crystallizing simultaneously, a simple calculation such as the one illustrated here is not as easily applied and it is usually necessary to use the MELTS family of algorithms (e.g. Ghiorso & Sack, 1995; Ghiorso et al., 2002) or Petrolog3 (Danyushevsky & Plechov, 2011) to determine the identity, composition, and amounts of crystallizing minerals.

CO_2 solubility and fluid exsolution

The physical and chemical factors that control the solubility of CO_2 and other volatiles in melts have been constrained through decades of experimental and modeling studies (Moore, 2008). Experimental studies show that the solubility of CO_2 is strongly correlated with pressure (e.g., Mysen et al., 1976; Stolper & Holloway, 1988), and that melt composition also plays an important role in CO_2 solubility because of the potential for C to dissolve in the melt as carbonate ions (Fine & Stolper, 1986; Guillot & Sator, 2011). As more experimental data covering an increasing range of melt compositions and thermodynamic conditions has become available, the compositional range over which these models are valid has grown from tholeiites (Dixon et al., 1995) to include more

alkaline and silica undersaturated conditions as well as rhyolitic compositions (Dixon, 1997; Papale et al., 2006; Iacono-Marziano et al., 2012). A variety of software tools have also been developed that incorporate the experimental data to produce melt volatile solubility models that are applicable to a wider range of compositions and conditions (Newman & Lowenstern, 2002; Witham et al., 2012; Burgisser et al., 2015).

Iacono-Marziano et al. (2012) present a thermodynamically-based model that is empirically calibrated to account for the effect of melt composition on volatile solubility. For a volatile-saturated melt with a given major element composition, the model of Iacomo-Marziano et al. (2012) can be simplified and expressed as a system of three equations

$$\ln[CO_3^{2-}]^{ppm} = B^*_{CO_2} + a_{CO_2}\ln\left(P_{CO_2}\right) + C_{CO_2}\frac{P}{T} \quad (3)$$

$$\ln[H_2O]^{wt\%} = B^*_{H_2O} + a_{H_2O}\ln\left(P_{H_2O}\right) + C_{H_2O}\frac{P}{T} \quad (4)$$

$$P = P_{CO_2} + P_{H_2O} \quad (5)$$

where C_{CO_2}, C_{H_2O} a_{CO_2}, and a_{H_2O} are empirically defined constants (and do *not* represent CO_2 and H_2O activity), P_{CO_2} and P_{H_2O} are the partial pressures of CO_2 and H_2O in the fluid phase, and P and T are the equilibrium pressure and temperature (in bars and Kelvins, respectively). Note that the C concentration in the melt is expressed in terms of CO_3^{2-} and not as CO_2 ($0.27\ ppm\ C = 1\ ppm\ CO_2 = 1.49\ ppm\ CO_3^{2-}$). The model presented by Iacono-Marziano et al. (2012) includes multiple compositional parameters, including the number of non-bridging oxygens per mole of oxygen in the melt and other empirically calibrated compositional parameters (Table 1). To simplify the calculations in this example, these compositional terms are consolidated here into the terms $B^*_{CO_2}$ and $B^*_{H_2O}$, which can be considered as constant for a given melt composition.

In some cases, it is desirable to calculate a saturation pressure P corresponding to known concentrations of CO_3^{2-} and H_2O at a constant temperature. Given equations 3-5 and three unknown parameters, it is possible to determine the remaining three parameters analytically. However, for situations requiring multiple calculations, it is usually more convenient to use a numerical method to obtain the desired solution. To accomplish this,

equations (3) and (4) can be rewritten such that P_{CO_2} and P_{H_2O} are expressed as a function of P, and then P is determined numerically using a root-finding algorithm to identify the pressure P for which $P_{CO_2} + P_{H_2O} - P = 0$.

Using this method, we can calculate the saturation pressure of a primary melt from Hawaii described above (Table 1). For the calculation, we use an average primary melt composition for Kilauea estimated from petrologic modeling (Sobolev et al., 2005; Table 1) and the "anhydrous" calculation method as described by Iacono-Marziano et al. (2012). Based on the assumed volatile concentration of $X_{CO_3^{2-}} = 14900\ ppm$ (1 wt% CO_2), $X_{H_2O} = 1\ wt\%$, and a typical basaltic melt temperature of $1{,}473\ K$ (1200 °C), the calculated saturation pressure is ~9.7 kbar. Assuming a pressure gradient of 3.5 km per kbar, the calculated depth is ~34 km. This is less than the inferred depth of melting ~ 40 km below Kilauea (e.g. Ryan, 1988) and suggests that a primary melt with the composition used in this example would have been fluid-undersaturated. The pressure at 40 km is consistent with a higher CO_2 concentration (~1.25 wt%) or a melt that is more evolved (e.g. higher Al_2O_3 and lower MgO). If the saturation pressure is similar to the pressure at the depth of melting, the melt would become saturated in CO_2 immediately as it begins to ascend and decompress.

Fractional crystallization may promote or inhibit CO_2 exsolution because the concentration of CO_2 in the melt is enriched due to crystallization, and because the solubility of CO_2 in the melt is a function of melt composition, which changes during fractional crystallization. Specifically, the CO_2 solubility in the melt tends to decrease as the melt becomes more evolved. At the same time, as melt crystallizes less melt is available to dissolve the CO_2, and these combined effects can lead to oversaturation in CO_2 and degassing. However, this is less likely to be significant in the case of Kilauea, where evidence suggests that decompression and degassing begin deep in the melt conduit, before significant fractional crystallization occurs (Ryan, 1988; Anderson & Brown, 1993; Dixon et al., 1997).

Melt inclusions

As a consequence of decompression and fractional crystallization, magmas degas as they approach the surface and erupt. Most of the available information concerning the current flux of volatiles from the deep earth to the atmosphere is provided by remote sensing and *in-situ* sampling of fumaroles and volcanic vents (Burton et al. 2013). While these methods provide the most robust estimates of the CO_2 output of an actively degassing modern volcano, they cannot be applied to inactive or extinct volcanoes. It is also worth noting that a significant portion of the CO_2 transferred from the deep earth to the surface bypasses volcanic centers entirely as a part of widespread regional outgassing (Chiodini et al., 2004), even though the CO_2 might originate from the same primary melt that is outgassing CO_2 at the volcanic vent. For these reasons, it is sometimes advantageous to use petrologic information to constrain the flux of CO_2 from a degassing volcanic system.

As indicated in the previous section, the bulk compositions of lava and tephra samples provide information regarding the melt composition as a function of melting and fractional crystallization. However, because volatile solubility approaches zero with decreasing pressure, the volatile abundances of bulk lavas and tephras do not reliably record the degassing history of a volcanic system. In some cases, dredged submarine lavas may be used to estimate the volatile composition of the melt at ocean-bottom pressures (e.g. Dixon et al., 2008), and this composition can be used as a boundary condition when modeling the degassing process (e.g. Dixon & Clague, 2001). As an alternative, melt inclusions trapped by minerals that are crystallizing deep within magma reservoirs are often used to estimate the pre-eruptive CO_2 (and other) concentrations of melts associated with both recent and ancient volcanic events (Métrich and Wallace, 2008; Audétat & Lowenstern, 2013) because they trap a melt that is less likely to have degassed. This approach has been applied to estimate the CO_2 content of magmas from a range of tectonic environments which include convergent margin settings (Esposito et al., 2011; Johnson et al., 2009; Mironov et al., 2015; Aster et al., 2016; Rasmussen et al., 2017), mid-ocean ridge settings (e.g. Helo et al., 2011), and intraplate settings (Hartley et al., 2014; Tuohy et al., 2013; Moore et al., 2015).

Melt inclusions represent samples of melt trapped by a growing phenocryst, and are analogous to fluid inclusions (Roedder, 1979; Roedder, 1984). Melt inclusions may be classified petrographically in the same manner as fluid inclusions whereby "primary" melt inclusions are those trapped during crystal growth in irregularities in discrete growth episodes, and "secondary" melt inclusions are formed when melt is trapped as a fracture in a crystal heals. Groups of petrographically-related melt inclusions, which can be presumed to have been trapped at the same time, are referred to as "melt inclusion assemblages" (Bodnar & Student, 2006), and the degree to which the composition of a melt inclusion represents the composition of the melt present during the time of trapping can be evaluated by comparing the compositions of multiple inclusions within a melt inclusion assemblage (Esposito et al., 2014). Additionally, it is worth noting that the term "primary" melt inclusion does NOT imply that the melt inclusion trapped a "primary" melt. For example, consider the case of "primary melt inclusions" trapping an andesitic melt that has fractionated from a basaltic "primary melt." The term "melt inclusion" may refer to silicate melts as well as salt, carbonatite, and sulfide melts, and in some cases, crystallized melt inclusion with a high volatile content may be referred to as "high-density fluid inclusions".

A melt inclusion behaves as a "miniature magma chamber" in that it experiences fractional crystallization and fluid saturation as it cools. During this cooling process, the melt within the inclusion is likely to become volatile-saturated and exsolve CO_2 (Moore et al., 2015) and potentially other volatile elements (e.g. Esposito et al., 2016) into a separate fluid phase. However, unlike an actual magma chamber, melt inclusions behave as a closed system with respect to C provided that they do not leak (Maclennan, 2017). This is in contrast to some elements, such as H (Mironov & Portnyagin, 2011; Gaetani et al., 2012) and Fe (Danyushevsky et al., 2002) that can diffuse into and out of melt inclusions. Therefore, it is possible to determine the total CO_2 content of the inclusion using experimental, numerical, or mass balance techniques (Moore et al., 2018), and this value should represent the CO_2 content of the melt that was originally trapped in the inclusion. For example, microthermometry (Naumov et al., 2008) or Raman spectroscopy (Lamadrid et al., 2017) can be used to estimate the density of CO_2 fluid bubbles in melt inclusions and the total CO_2 content of the inclusion can be determined using a mass-

balance calculation (Steele-MacInnis et al., 2011; Hartley et al., 2014; Moore et al, 2015; Aster et al., 2016). In the case of a glassy melt inclusion containing a bubble, the total amount of CO_2 contained in the inclusion can be expressed as

$$X_{CO_2}^{inclusion} = \frac{m_{CO_2}^{glass} + m_{CO_2}^{bubble}}{m^{glass} + m^{bubble}} \approx X_{CO_2}^{glass} + \Delta X_{CO_2}^{bubble} \quad (6)$$

where $m_{CO_2}^{glass}$ and $m_{CO_2}^{bubble}$ represent the mass of CO_2 in the glass and bubble, and m^{glass} and m^{bubble} represent the total mass of each of the two phases. The total mass of the bubble is negligible compared to the mass of the glass for bubbles that contain CO_2 vapor and occupy only a few volume percent of the inclusion. As such, the concentration of CO_2 in the trapped melt can be calculated by adding the concentration of CO_2 in the glass $X_{CO_2}^{glass}$ to $\Delta X_{CO_2}^{bubble}$, the ratio of the mass of CO_2 in the bubble to the mass of the glass. This is calculated using a mass balance approach

$$\Delta X_{CO_2}^{bubble} = \frac{m_{CO_2}^{bubble}}{m^{glass}} = \frac{\rho_{CO_2}^{bubble} * V^{bubble}}{\rho^{glass} * (1 - V^{bubble})} \quad (7)$$

where $\Delta X_{CO_2}^{bubble}$ is the amount that the concentration of CO_2 in the inclusion changes when the CO_2 in the bubble is included, $\rho_{CO_2}^{bubble}$ is the density of CO_2 in the fluid bubble, ρ^{glass} is the bulk density of the glass, and V^{bubble} is the volume proportion of the bubble.

Melt inclusions from the 1959 Kilauea Iki eruption reported by Moore et al. (2015) typically contain bubbles with $\rho_{CO_2}^{bubble} = 0.1\ g/cm^3$, V^{bubble} = 0.03 (i.e. 3 volume percent), and $\rho^{glass} = 2.75\ g/cm^3$. These values yield a calculated contribution of CO_2 from the bubble of $\Delta X_{CO_2}^{inclusion} = 1124\ ppm$ (Figure 4). Given an assumed CO_2 concentration in the glass of $X_{CO_2}^{glass} = 300$ ppm from the range of concentrations reported by Anderson & Brown (1993), 21% of the CO_2 in this inclusion is contained in the glass, 79% is contained in the bubble, and the concentration of CO_2 in the melt trapped by the inclusion is

$$X_{CO_2}^{inclusion} \approx \frac{0.1\ g/cm^3 * 0.03}{2.75\ g/cm^3 * (1 - 0.03)} + 300\ ppm = 1424\ ppm$$

It should also be noted that largest uncertainty associated with the calculated CO_2 content of a melt inclusion is related to the volume proportion of the inclusion occupied by the vapor bubble. For example, if the volume proportion of the bubble in the calculation above is only constrained to within plus or minus 1 volume percent, this corresponds to approximately 33% relative uncertainty in the amount of CO_2 contained within the bubble. Accordingly, Moore et al. (2015) report CO_2 contents that vary from approximately 150 ppm to 1900 ppm in melt inclusions erupted from Kilauea and its East Rift Zone, although Tuohy et al. (2014) report limited variations in the major element content of the glass (approximately 8 to 10 wt% MgO). The variation in the CO_2 content of the melt inclusions exceeds the propagated analytical uncertainty described above and is also greater than the variability that would be produced by crystal fractionation implied by observed range in MgO concentration. This suggests that the variation in the CO_2 content of the melt is primarily controlled by the extent of degassing that had occurred.

Volatile saturation pressures of melts contained within olivine-hosted melt inclusions are often used to infer the conditions at which melt inclusions were trapped. This is particularly useful because barometers that can be applied to volcanic systems in which olivine is the only crystallizing phase are not available. For example, using the same assumptions from the volatile solubility calculation above and a melt containing 1424 ppm of CO_2 and a typical value of 0.5 wt% H_2O (Anderson & Brown, 1993), the calculated saturation pressure is 1.1 kbar. However, it should be noted that a calculated saturation pressure reflects the pressure at which the melt inclusion was trapped *only* if the melt was saturated in a separate fluid phase at the time of trapping. In other words, if volatile saturation at the time of trapping cannot be confirmed, then the pressure recorded by a melt inclusion represents a minimum trapping pressure because the inclusion could have trapped a melt that was volatile undersaturated.

Petrographic information may sometimes be used to assess whether volatile saturation has occurred. For example, the presence of phenocrysts containing CO_2-rich fluid inclusions suggests that a separate CO_2 phase was present, indicating that CO_2 degassing had occurred previously (Hansteen & Klügel, 2008; Mironov & Portnyagin, 2011; Oligialoro et al., 2018). In the case of melt inclusions from Kilauea reported by

Moore et al. (2015), it was noted that melt inclusion assemblages found in some of the crystals contained both CO_2-rich fluid inclusions and melt inclusions with varying proportions of CO_2-rich fluid, and suggests that volatile saturation was reached while the melt inclusions were being trapped. However, because the relative timing of inclusion entrapment could not be petrographically constrained, it is unclear which if any of the melt inclusions considered in that study were trapped before this episode of heterogeneous fluid entrapment. Alternatively, the state of volatile saturation can be determined if the pressure at which the host mineral crystallized can be determined independently of the volatile-melt saturation pressure. For example, Maclennan (2017) describes a group of olivine-hosted melt inclusions from Iceland with saturation pressures significantly less than equilibrium pressures estimated from cotectic pyroxene crystallization. In that case, it was observed that the melt inclusion trapping pressures were significantly greater than the calculated saturation pressures. These results suggest that the inclusions could have trapped a volatile-undersaturated melt similar to the undegassed melts that have been previously reported in several mid-ocean ridge settings (Saal et al., 2002; Shimizu et al., 2016; Le Voyer et al. 2016; Matthews et al., 2017).

Total CO_2 flux

The final stage in the transfer of CO_2 from the deep earth to the atmosphere occurs at the surface during volcanic outgassing. Estimating the flux of CO_2 due to outgassing is complicated by the potential for CO_2-bearing melts to form. These may originate from the same region of melting and be partitioned into different magma reservoirs and outgas from different volcanic edifices or by diffuse regional degassing (e.g. Chiodini et al., 2004). Evidence of multiple reservoirs is particularly well documented for Hawaii where outgassing occurs both through a main summit reservoir and from multiple rift zones that are supplied by the lateral transport of melt (Poland et al., 2014). Therefore, in this example, we assume a steady state between the rate at which CO_2-bearing magma is supplied to the summit reservoir below Kilauea and the rate of outgassing of CO_2 in the gas plume, as described by Gerlach et al. (2002), and we ignore the possible distribution of magma into multiple magma reservoirs. In this case, the flux of CO_2 from a volcano can be related to the melt supply rate and the CO_2 concentration in

the melt (e.g. Wallace, 2005). This relationship is based on the assumption that the melt degasses almost entirely as it ascends and erupts, and can be quantified following a mass balance approach:

$$m_{CO_2} = X_{CO_2}^{melt} V^{melt} \rho^{melt} \tag{8}$$

where m_{CO_2} is the mass flux of CO_2 leaving the volcanic system, $X_{CO_2}^{melt}$ is the concentration of CO_2 in the undegassed melt, V_{melt} is the volume flux of the melt, and ρ_{melt} is the bulk density of the melt.

Many geophysical, petrologic, and remote sensing studies have been conducted at Kilauea and these studies provide information needed to solve the mass balance equation above (Figure 5). For example, Gerlach et al. (2002) infer a CO_2 flux of $m_{CO_2} = 9000\ t/day$ based on gas measurements of the volcanic plume. The bulk density of the degassing magma was estimated to be $\rho_{melt} = 2600\ kg/m^3$, based on the temperature and composition of the melt. Geophysical data of Cayol et al (2000) indicate that the eastern flank of Kilauea is swelling at a rate of $V_{melt} = 0.18\ km^3/y$, and this was assumed to represent the rate of magma generation in the subsurface. Given these assumptions described by Gerlach et al. (2002), the primary melt contains

$$X_{CO_2}^{melt} = \frac{m_{CO_2}}{V^{melt}\rho^{melt}} = \frac{9000\frac{t}{day}}{0.18\frac{km^3}{y} * 2600\frac{kg}{m^3}} = \frac{3.28 * \frac{10^9 kg}{y}}{0.18 * \frac{10^9 m^3}{y} * 2600\frac{kg}{m^3}}$$
$$\approx 7000\ ppm\ CO_2$$

Because the rate of outgassing is related to the concentration of CO_2 in the melt, it is possible to compare the CO_2 concentration recorded by melt inclusions to the rate of outgassing determined by gas measurements from the volcanic plume. For example, Moore et al. (2015) report melt inclusions from Kilauea containing up to ~3000 ppm CO_2. Given the same melt production rate reported by Cayol et al. (2000), this concentration suggests either that the melt inclusions trapped a partially degassed melt or that the average CO_2 flux is approximately half of the value reported by Gerlach et al. (2002) and is more consistent with fluxes reported by Greenland et al. (1985; 0.58 Mt/y) and Hager et al. (2008; 1.79 Mt/y). Cayol et al. (2000) used geophysical methods to

estimate the melt production rate based on swelling of the volcanic edifice. Alternatively, Robinson & Eakins (2006) calculated the melt production rate to be approximately 0.25 km^3/year using a combination of radiometric age dating and high-resolution bathymetry. If this latter melt production rate is used instead of the rate (0.18 km^3/y) provided by Cayol et al. (2000), then the CO_2 flux from Gerlach et al. (2002) is consistent with a concentration of CO_2 in the melt of 5000 ppm, which is more similar to the composition of melt inclusions reported by Moore et al. (2015). As the calculations above demonstrate, estimates of CO_2 flux based on melt inclusions are sensitive to the melt volume flux that is used. The melt production rate for Hawaii is highly variable both at the island scale as recorded by ocean bathymetry (Vidal & Bonneville, 2004; Van Ark & Lin, 2004) and at the volcano scale as shown by the stratigraphy of lava flows present at Kilauea (Peterson & Moore, 1987). In addition to the geophysical approach described by Cayol et al. (2000) the melt volume flux may also be constrained using methods that include field and remote sensing observations of lava flow morphology and extent (Walker, 1973; Kilburn & Lopes, 1991; Favalli et al., 2010) as well as thermal monitoring techniques (Wright et al., 2001; Harris et al., 2005).

A disadvantage of using petrologic information (e.g. melt inclusions, dredged submarine lavas) to infer the CO_2 flux of a volcanic system is that determining the extent to which CO_2 has been lost by degassing is challenging. As described above, it is likely that the CO_2 contents of melt inclusions reported by Moore et al. (2015) and Tuohy (2014) represent melt compositions after some amount of degassing had occurred, and in the absence of information concerning the concentration of CO_2 in the primary melt (C_L), the amount of CO_2 that may have been lost by degassing cannot be determined. Therefore, melt inclusions from the petrologic record may be preferred for deriving an average flux of volatiles from volcanic systems over long periods of time. However, due to its relatively low solubility compared to other volatile components, CO_2 fluxes estimated in this manner likely represent a minimum estimate (Wallace et al., 2005).

Other geochemical data have also been used to estimate the CO_2 concentration of the primary melt associated with Kilauea. Dixon et al. (1997) used the observed CO_2 concentration and CO_2/P_2O_5 ratio of dredged submarine lavas and the P_2O_5 concentration calculated for the primary melt to obtain a CO_2 concentration of 1.3-4.9 wt%. Dixon &

Clague (2001) used a degassing model to obtain a similar result based on analyses of dredged submarine glasses from the Loihi seamount. More recently, Sides et al. (2014) obtained results roughly consistent with those of Dixon & Clague (2001) and the CO2 concentration inferred by Gerlach et al. (2002) by analyzing Nb concentrations in melt inclusion glasses from Kilauea lava fountains, and calculating the CO_2 concentration of the primary melt using the CO_2/Nb ratio of melts that are presumed to be fluid-undersaturated or to not to have lost a significant amount of CO_2 by degassing (e.g. Saal et al., 2002, Shimizu et al., 2016; Le Voyer et al., 2016; Matthews et al., 2017). Additionally, Baysean statistical methods have also been used to estimate the CO_2 concentration of the primary melt based on data from melt inclusions and measurements of the gas plume (Barsanti et al, 2009; Anderson & Poland, 2017).

Outlook and conclusions

In this review, we demonstrate the relationship between the CO_2 budget of a magma and the processes of melting, crystallization, fluid exsolution, degassing and outgassing. We also show that one can quantify the effects of these processes by using a combination of petrologic, geochemical, and remote sensing methods. As shown in the examples from Kilauea, an integrated approach that includes multiple types of information can be applied to develop a CO_2 budget for the volcanic system. Constraining the CO_2 budgets of magmas is fundamental to estimating the transfer of CO_2 from the deep earth to the atmosphere, and by using a combination of the available information preserved in bulk rock, fluid, and melt inclusion samples preserved in the geologic record, it is possible to estimate volcanic CO_2 fluxes in the past.

Acknowledgements

We thank Maria Luce Frezzotti for editorial handling of this manuscript in addition to organizing and providing us the opportunity to contribute to this special volume. We also thank reviewers Philippe Robidoux and Paul Wallace for their thorough and constructive reviews which improved the quality of the manuscript. This work was supported by NSF grant 1624589 to RJB.

References

Allard, P. (2018, this volume)

Anderson, A.T. and Brown, G.G. (1993) CO_2 contents and formation pressures of some Kilauean melt inclusions. American Mineralogist, 78, 794-803.

Anderson, K.R., Poland, M.P., Abundant carbon in the mantle beneath Hawai'I, Nature Geoscience, 10, 704-708.

Audétat, A., and Lowenstern, J.B. (2014) 13.6 - Melt Inclusions. In H.D. Holland, and K.K. Turekian, Eds. Treatise on Geochemistry (Second Edition), p. 143-173. Elsevier, Oxford.

Barsanti, M., Papale, P., Barbato, D., Moretti, R., Boschi, E., Hauri, E., Longo, A. (2009) Heterogeneous large total CO2 abundance in the shallow magmatic system of Kilauea volcano, Hawaii, Journal of Geophysical Research, 114, 7 p.

Bodnar, R.J., Student, J.J. (2006) Melt inclusions in plutonic rocks: petrography and microthermometry, Melt inclusions in plutonic rocks, Ed. Webster, J. D. Mineralogical Assoociation of Canada Short Course Series Vol. 36, 1-25.

Burgisser, A., Alletti, M., Scalliet, B. (2015) Simulating the behavior of volatiles belonging to the C–O–H–S system in silicate melts under magmatic conditions with the software D-Compress, Computers & Geosciences, 79, 1-14.

Burton, M.R., Sawyer, G.M., Granieri, D. (2013) Deep Carbon Emissions from Volcanoes, Reviews in Mineralogy & Geochemistry, 75, 323-354

Canil, D., O'Neill, H.St.C., Pearson, D.G., Rudnick, R.L., McDonough, W.F., Carswell, D.A. (1994) Ferric iron in peridotites and mantle oxidation states, Earth and Planetary Science Letters, 123, 205-220.

Cayol, V., Dieterich, J.H., Okamura, A.T., Miklius, A. (2000) High Magma Storage Rates Before the 1983 Eruption of Kilauea, Hawaii, Science, 288, 2343-2346

Chiodini et al (2018, this volume)

Chiodini, G., Cardellini, C., Amato, A., Boschi, E., Caliro, S., Frondini, F., Ventura, G. (2004) Carbon dioxide Earth degassing and seismogenesis in central and southern Italy. Geophysical Research Letters, 31.

Danyushevsky, L.V., Plechov, P. (2011) Petrolog3: Integrated software for modeling crystallization processes, Geochemistry, Geophysics, Geosystems, 12, 7, 32 p.

Dasgupta, R., Hirschmann, M.M., Smith, N.D. (2007) Partial Melting Experiments of Peridotite + CO2 at 3 GPa and Genesis of Alkalic Ocean Island Basalts, Journal of Petrology, 48, 11, 2093-2124.

Dasgupta, R., Mallik, A., Tsuno, K., Withers, A.C., Hirth, G., Hirschmann, M.M. (2013) Carbon-dioxide-rich silicate melt in the Earth's upper mantle, Nature, 493, 211-215.

Dixon, J., Clague, D.A., Cousens, B., Monsalve, M.L., Uhl, J. (2008) Carbonatite and silicate melt metasomatism of the mantle surrounding the Hawaiian plume: Evidence from volatiles, trace elements, and radiogenic isotopes in rejuvenated-stage lavas from Niihau, Hawaii, Geochemistry Geophysics Geosystems, 9, 9, 34 p.

Dixon, J.E. (1997) Degassing of alkalic basalts, American Mineralogist, 82, 368-378.

Dixon, J.E., Clague, D.A. (2001) Volatiles in basaltic glasses from Loihi seamount, Hawaii: evidence for a relatively dry plume component, 42, 3, 627-654.

Dixon, J.E., Clague, D.A., Wallace, P., Poreda, RR. (1997) Volatiles in Alkalic Basalts from the North Arch Volcanic Field, Hawaii: Extensive Degassing of Deep Submarine-erupted Alkalic Series Lavas, Journal of Petrology, 38, 7, 911-939.

Dixon, J.E., Stolper, E.M., and Holloway, J.R. (1995) An experimental study of water and carbon dioxide solubilities in mid-ocean ridge basaltic liquids. Part I: Calibration and solubility models. Journal of Petrology, 36 (6), 1607-1631.

Esposito, R., Bodnar, R.J., Danyushevsky, L.V., de Vivo, B., Fedele, L., Hunter, J., Lima, A., Shimizu, N. (2011) Volatile evolution of magma associated with the Solchiaro eruption in the Phlegrean Volcanic District (Italy). Journal of Petrology, 52 (12), 2431-2460.

Esposito, R., Hunter, J., Schiffbauer, J.D., Shimizu, N., Bodnar, R.J. (2014) An assessment of the reliability of melt inclusions as recorders of the pre-eruptive volatile content of magmas, Amerrican Mineralogist, 99, 976-998.

Favalli, M., Fornaciai, A., Mazzarini, F., Harris, A., Neri, M., Behncke, B., Pareschi, M.T., Tarquini, S., Boschi, E. (2010) Evolution of an active lava flow field using a multitemporal LIDAR acquisition, Journal of Geophysical Research, 115, B11203, 1-17.

Fine, G., Stolper, E. (1986) Dissolved carbon dioxide in basaltic glasses: concentrations and speciation, Earth and Planetary Science Letters, 76, 263-278.

Frezzotti, M.L., Peccerillo, A. (2007) Diamond-bearing COHS fluids in the mantle beneath Hawaii, Earth and Planetary Science Letters, 262, 273-283.

Friedlingstein, P., Houghton, R.A., Marland, G., Hackler, J., Boden, T.A., Conway, T.J., Canadell, J.G., Raupach, M.R. Ciais, P., Le Quéré, C. (2010) Update on CO_2 emissions, Nature Geoscience, 3, 811-812.

Gerlach, T.M., McGee, K.A., Elias, T., Sutton, A.J., Doukas, M.P. (2002) Carbon dioxide emission rate of Kilauea Volcano: Implications for primary magma and the summit reservoir, 107, B9, 15 p.

Ghiorso, M.S., Hirschmann, M.M., Reiners, P.W., Kress III, V.C. (2002) The pMELTS: A revision of MELTS for improved calculation of phase relations and major element partitioning related to partial melting of the mantle to 3 GPa, Geochemistry, Geophysics, Geosystems, 3, 5, 36 p.

Ghiorso, M.S., Sack, R.O. (1995) Chemical mass transfer in magmatic processes IV. A revised and internally consistent thermodynamic model for the interpolation and extrapolation of liquid-solid equilibria in magmatic systems at elevated temperatures and pressures, Contributions to Mineralogy and Petrology, 119, 2-3, 197-212.

Greenland, L.P., Rose, W.I., Stokes, J.B. (1985) An estimate of gas missions and magmatic gas content from Kilauea volcano, Geochimica et Cosmochimica Acta, 49, 125-129.

Guillot, B., Sator, N. (2011) Carbon dioxide in silicate melts: A molecular dynamics simulation study, Geochimica et Cosmochimica Acta, 75, 1829-1857.

Hager, S.A., Gerlach, T.M., Wallace, P.J. (2008) Summit CO_2 emission rates by the CO_2/SO_2 ratio method at Kilauea Volcano, Hawaii, during a period of sustained inflation, Journal of Volcanology and Geothermal Research, 177, 875-882.

Hansteen, T.H., Klügel, A. (2008) Fluid Inclusion thermobarometry as a tracer for Magmatic Processes, Reviews in Mineralogy and Geochemistry, 69, 143-177.

Harris, A., Favalli, M., Steffke, A., Fornaciai, A., Boschi, E. (2010) A relation between lava discharge rate, thermal insulation,and flow area set using lidar data, Geophysical Research Letters, 37, L20308, 1-6.

Hartley, M.E., Maclennan, J., Edmonds, M., Thordarson, T. (2014) Reconstructing the deep CO2 degassing behavior of large basaltic fissure eruptions. Earth and Planetary Science Letters, 393, 120-121.

Helo, C., Longpré, M.A., Shimizu, N., Clague, D.A., Stix, J. (2011) Explosive eruptions at mid-ocean ridges driven by CO2-rich magmas. Nature Geoscience, 4, 260-263.

Iacono-Marziano, G., Morizet, Y., Le Trong, E., Gaillard, F. (2012) New experimental data and semi-empirical parameterization of H_2O–CO_2 solubility in mafic melts, Geochimica et Cosmochimica Acta, 97, 1-23.

Javoy, M., Pineau, F. (1991) The volatiles record of a "popping" rock from the Mid-Atlantic Ridge at 14° N: chemical and isotopic composition of gas trapped in the vesicles, Earth and Planetary Science Letters, 107, 589-611.

Johnson, E.R., Wallace, P.J., Cashman, K.V., Granados, H.D., Kent, A.J.R. (2009) Magmatic volatile contents and degassing-induced crystallization at Volcán Jorullo, Mexico: Implications for melt evolution and the plumbing systems of monogenetic volcanoes, Earth and Planetary Science Letters, 269, 3-4, 478-487.

Kilburn, C.R.J., Lopes, R.M.C. (1991) General Patterns of Flow Field Growth: Aa and Blocky Lavas, Journal of Geophysical Research, 96, B12, 19721-19732.

Le Voyer, M., Kelly, K.A., Cottrell, E., Hauri, E.H. (2016) Heterogeneity in mantle carbon content from CO2-undersaturated basalts, Nature Communications, 8:14062, 1-8.

Lloyd, A.S., Ruprecht, P., Hauri, E.H., Rose, W., Gonnermann, H.M., Plank, T. (2014) NanoSIMS results from olivine-hosted melt embayments: Magma ascent rate during explosive basaltic eruptions, Journal of Volcanology and Geothermal Research, 283, 1-18.

Luth, R.W. (1999) Carbon and carbonates in the mantle. In: Fei, Y., Bertka, C.M., Mysen, B.O. (Eds.), Mantle Petrology: Field Observations and High Pressure Experimentation: A Tribute to Francis R. (Joe) Boyd, 6. The Geochemical Society, pp. 297–316.

Maclennan, J. (2017) Bubble formation and decrepitation control the CO_2 content of olivine-hosted melt inclusions, Geochemistry, Geophysics, Geosystems, 10.1002/2016GC006633.

Matthews, S., Shorttle, O., Rudge, J.F., Maclennan, J. (2017) Constraining mantle carbon: CO2-trace element systematics in basalts and the roles of magma mixing and degassing, Earth and Planetary Science Letters, 480, 1-14.

Matzen, A.K., Baker, M.B., Beckett, J.R., Stolper, E.M. (2011) Fe-Mg Partitioning between Olivine and High-magnesian Melts and the Nature of Hawaiian Parental Liquids, Journal of Petrology, 52, 7&8, 1243-1263.

Métrich, N. and Wallace, P.J. (2008) Volatile abundances in basaltic magmas and their degassing paths tracked by melt inclusions. Reviews in Mineralogy & Geochemistry, 69, 363-402.Ruprecht & Plank (2013)

Mironov, N., Portnyagin, M., Botcharnikov, R., Gurenko, A., Hornle, K., Holtz, F. (2015) Quantification of the CO2 budget and H2O–CO2 systematics in subduction-zone magmas through the experimental hydration of melt inclusions in olivine at high H2O pressure. EPSL, 425, 1-11.Esposito thesis/paper about MI

Mironov, N.L., Portnyagin, M.V. (2011) H2O and CO2 in parental magmas of Kliuchevskoi volcano inferred from study of melt and fluid inclusions in olivine. Russian Geology and Geophysics, 52, 1353-1367.

Moore, G. (2008) Interpreting H_2O and CO_2 Contents in Melt Inclusions: Constraints from Solubility experiments and Modeling, Reviews in Mineralogy and Geochemistry, 69, 333-361.

Moore, L.R., Gazel, E., Tuohy, R., Lloyd, A.S., Esposito, R., Steele-MacInnis, M., Hauri, E.H., Wallace, P.J., Plank, T., Bodnar, R.J. (2015) Bubbles matter: An assessment of the contribution of vapor bubbles to melt inclusion volatile budgets, American Mineralogist, 100, 806-823.

Moore, L.R., Mironov, N., Portnyagin, M., Gazel, E., Bodnar, R.J. (2018) Volatile contents of primitive bubble-bearing melt inclusions from Klyuchevskoy volcano, Kamchatka: Comparison of volatile contents determined by mass-balance versus experimental homogenization, Journal of Volcanology and Geothermal Research, 358, 124-131.

Mysen, B.O., Eggler, D.H., Seitz, M.G., Holloway, J.R. (1976) Carbon dioxide in silicate melts and crystals. Part I. Solubility measurements, American Journal of Science, 276, 455-479.

Newman, S. and Lowenstern, J.B. (2002) VolatileCalc: a silicate melt–H_2O–CO_2 solution model written in Visual Basic for excel. Computers & Geosciences, 28, 597-604.

Ni, H., Keppler, H. (2013) Carbon in Silicate Melts, Reviews in Mineralogy and Geochemistry, 75, 251-287.

Oglialoro, E., Frezzotti, M.L., Ferrando, S., Tiraboschi, C., Principe, C., Groppelli, G., Villa, I.M. (2018) Lithospheric magma dynamics beneath the El Hierro Volcano, Canary Islands: insights from fluid inclusions, 79:70, 17 p.

Papale, P., Moretti, R., Barbato, D. (2006) The compositional dependence of the saturation surface of H_2O + CO_2 fluids in silicate melts, Chemical Geology, 229, 78-95.

Peterson, D.W., Moore, R.B. (1987) Geologic history and evolution of geologic concepts, Island of Hawaii, Eds. Decker, R.W., Wright, T.L., Stauffer, P.H., Volcanism in Hawaii, USGS Professional paper 1350, 149-189.

Poland, M.P., Miklius, A., Montgomery-Brown, E.K. (2014) Magma Supply, Storage, and Transport at Shield-Stage Hawaiian Volcanoes, Characteristics of Hawaiian Volcanoes, Eds. Poland, M.P., Takahashi, T.J., Landowski, C.M., USGS Prof. Paper 1801, 179-234.

Robinson, J.E., Eakins, B.W. (2006) Calculated volumes of individual shield volcanoes at the young end of the Hawaiian Ridge, Journal of Volcanology and Geothermal Research, 151, 309-307.

Robinson, J.E., Eakins, B.W. (2006) Calculated volumes of individual shield volcanoes at the young end of the Hawaiian Ridge, Journal of Volcanology and Geothermal Research, 151, 309-317.

Roedder, E. (1965) Liquid CO2 inclusions in olivine-bearing nodules and phenocrysts from basalts, The American Mineralogist, 50, 1746-1782.

Roedder, E. (1979) Origin and significance of magmatic inclusions. Bulletin de Mineralogie, 102, 467-510.

Roedder, E. (1984) Fluid Inclusions. Mineralogical Society of America, Reviews in Mineralogy, v. 12, 644 p.

Rollinson, H. (2014) Using geochemical data: evaluation, presentation, interpretation, Routledge, New York, NY, USA, 384 p.

Rosenthal, A., Hauri, E.H., Hirschmann, M.M. (2015) Experimental determination of C, F, and H partitioning between mantle minerals and carbonated basalt, CO2/Ba and CO2/Nb systematics of partial melting, and the CO2 contents of basaltic source regions, Earth and Planetary Science Letters, 412, 77-87.

Ryan, M.P. (1988) The Mechanics and Three-Dimensional Internal Structure of Active Magmatic Systems: Kilauea Volcano, Hawaii, Journal of Volcanology and Geothermal Research, 93, 5B, 4213-4248.

Saal, A.E., Hauri, E.H., Langmuir, C.H., Perfit, M.R. (2002) Vapour undersaturation in primitive mid-ocean-ridge basalt and the volatile content of Earth's upper mantle, Nature, 419, 451-455.

Shimizu, K., Saal, A.E., Meyers, C.E., Nagle, A.N., Hauri, E.H., Forsyth, D.W., Kamenetsky, V.M., Niu, Y. (2016) Two-component mantle melting-mixing model for the generation of mid-ocean ridge basalts: Implications for the volatile content of the Pacific upper mantle, Geochimica et Cosmochimica Acta, 176, 44-80.

Sides, I.R., Edmonds, M., Maclennan, J., Swanson, D.A., Houghton, B.F. (2014) Eruption style at Kilauea Volcano in Hawai`i linked to primary melt composition, Nature Geoscience, 7, 464-469.

Sobolev, A.V., Hofmann, A.W., Sobolev, S.V., Nikogosian, I.K. (2005) An olivine-free mantle source of Hawaiian shield basalts, Nature, 434, 590-597.

Steele-MacInnis, M., Esposito, R., and Bodnar, R.J., (2011) Thermodynamic model for the effect of post-entrapment crystallization on the H2O-CO2 systematics of vapor-saturated, silicate melt inclusions. Journal of Petrology, 52, 2461-2482.

Stolper, E., Holloway, J.R. (1988) Experimental determination of the solubility of carbon dioxide in molten basalt at low pressure, Earth and Planetary Science Letters, 87, 397-408.

Trull, T., Nadeau, S., Pineau, F., Polvé, M., Javoy, M. (1993) C-He systematics in for mantle carbon hotspot xenoliths: Implications contents and carbon recycling, 118, 43-64.

Tuohy, R. (2013) Olivine crystallization depths within Kilauea's lower east rift zone: The use of rehomogenized melt inclusions to interpret magma transport, storage and energetic fountaining. M.S. thesis, University of Oregon.

Van ark, E., Lin, J. (2004) Time variation in igneous volume flux of the Hawaii-Emperor hot spot seamount chain, Journal of Geophysical Research, 109, 1-18.

Vidal, V., Bonneville, A. (2004) Variations of the Hawaiian hot spot activity revealed by variations in the magma production rate, Journal of Geophysical Research, 109, 1-13.

Walker, G.P.L. (1973) Lengths of Lava Flows, Philosophical Transactions of the Royal Society of London. Series A, Mathematical and Physical Sciences, 274, 1238, 107-118.

Wallace, P.J. (2005) Volatiles in subduction zone magmas: concentrations and fluxes based on melt inclusion and volcanic gas data. Journal of Volcanology and Geothermal Research, 140, 217-240.

White, W.M. (2013) Geochemistry, Wiley-Blackwell, UK, 672 p.

Wirth, R., Rocholl, A. (2003) Nanocrystalline diamond from the Earth's mantle underneath Hawaii, Earth and Planetary Science Letters, 211, 357-369.

Witham, F., Blundy, J., Kohn, S.C., Lesne, P., Dixon, J., Churakov, S.V., Botcharnikov, R. (2012) SolEx: model for mixed COHSCl-volatile solubilities and exsolved gas compositions in basalt, Computers & Geosciences, 45, 87-97.

Wright, R., Blake, S., Harris, A.J.L., Rothery, D.A. (2001) A simple explanation for the space-based calculation of lava eruption rates, Earth and Planetary Science Letters, 192, 2, 223-233.

Figures

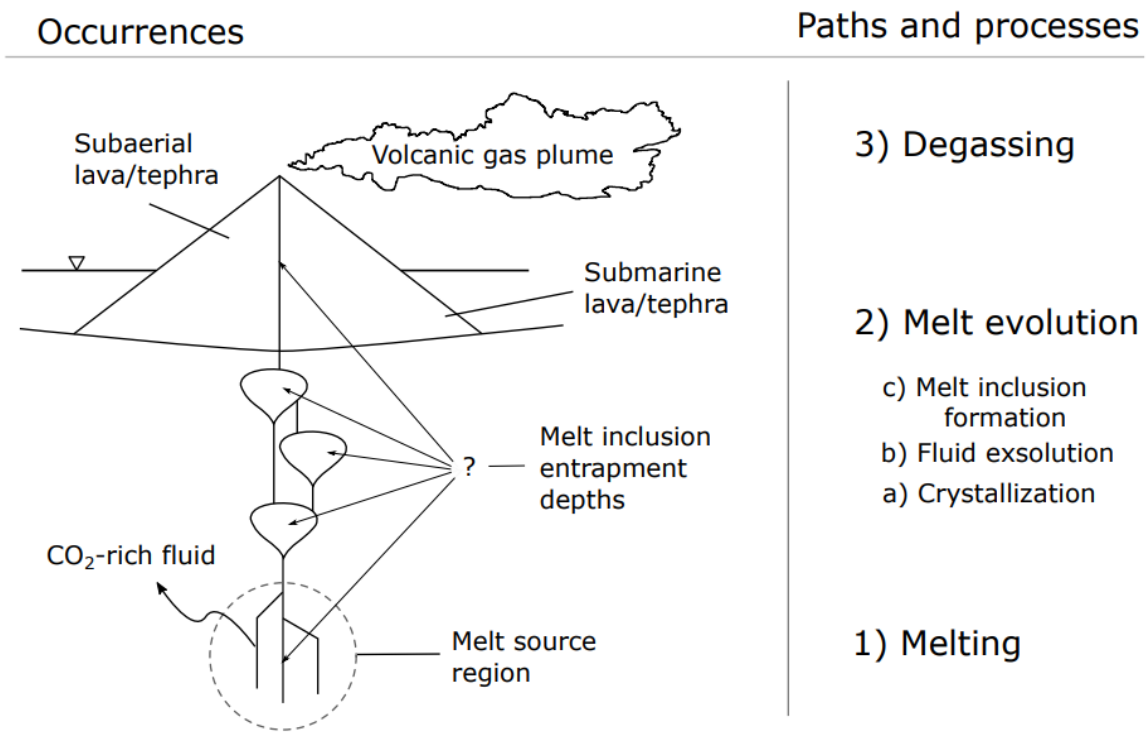

Figure 1: A schematic illustration of the distribution of CO2 in the volcanic system and processes that control the CO2 budget of a magma. CO2 is transferred into the melt by melting a source material that contains carbon. As the melt ascends toward the surface, the CO2 concentration may be enriched as a result of fractional crystallization or depleted as a result of fluid exsolution. Melt inclusions in crystallizing minerals may trap samples of the melt at different stages in this evolution, but determining the depth at which the inclusions were trapped is often challenging. At the surface, submarine or subaerial lava and tephra samples may be used to determine CO2 concentration of the melt after it has degassed at hydrostatic or atmospheric pressure. Remote sensing methods can be used to determine the CO2 flux from the volcanic gas plume, which is related to the CO2 concentration of the degassing melt and the melt production rate.

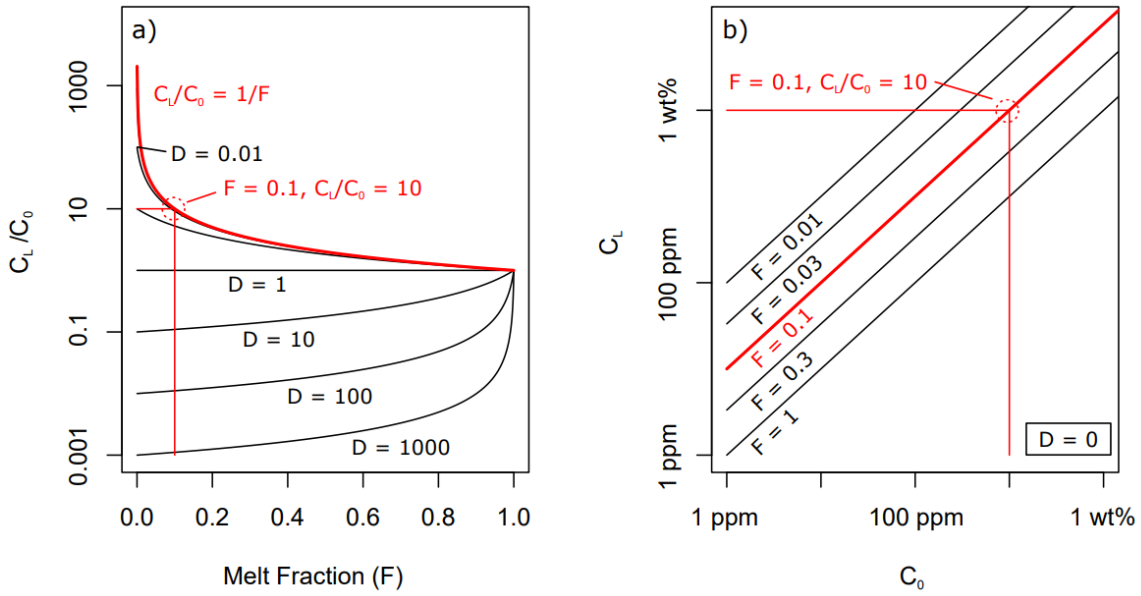

Figure 2: The concentration of dissolved components in the melt (C_L) as a function of the concentration of that component in the source material (C_0) during batch melting (Eq. 1). a) The curved solid red line corresponds to conditions at which $D = 0$ and $\frac{C_L}{C_0} = \frac{1}{F}$ representing a highly incompatible component. If the melt fraction (F) is 0.1, the concentration of the component in the resulting melt will be enriched by a factor of 10 relative to its concentration in the source material. b) Relationship between the concentration of a highly incompatible component ($D = 0$) in the source material (C_0) and its concentration in the resulting melt (C_L), for various melt fractions. The melt generated by 10% melting ($F = 0.1$) of a source material containing 1000 ppm of a component will contain 10,000 ppm (1 wt%) of that component.

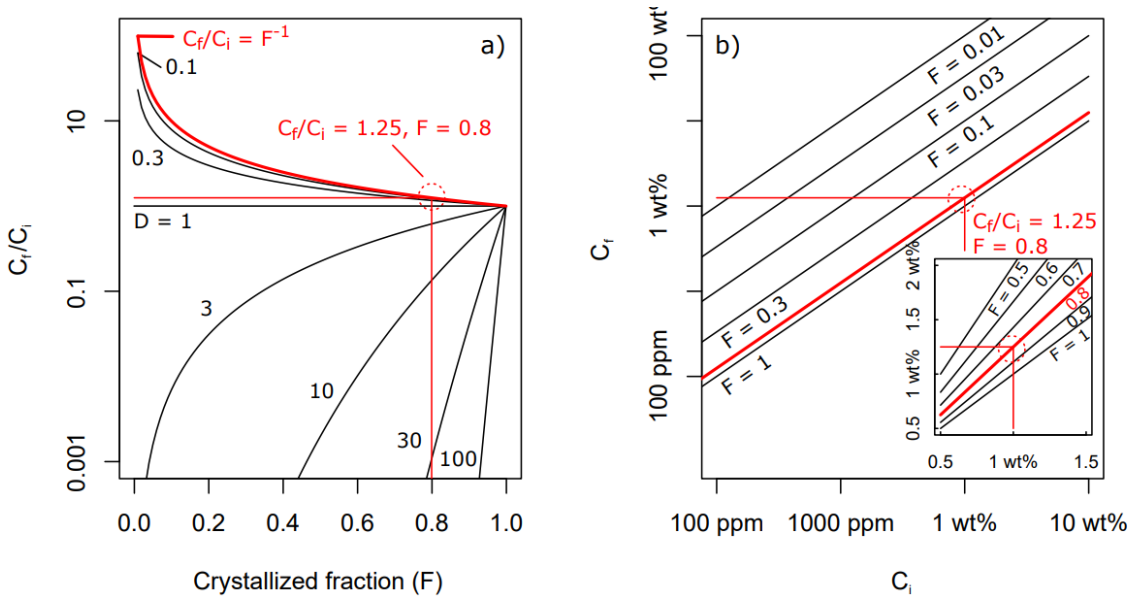

Figure 3: The concentration of a dissolved component in the melt before and after fractional crystallization (C_i and C_f respectively). a) The curved red line indicates the case in which $D = 0$ and $\frac{C_f}{C_i} = F^{-1}$, which applies to CO_2 in a silicate melt. When 20% of the melt has crystallized ($F = 0.8$), the resulting melt is enriched in CO_2 (C_f) relative to the concentration before crystallization (C_i) by a factor of 1.25. b) Contours show the relationship between C_i and C_f for an extremely incompatible element ($D = 0$). The red lines show that the concentration of CO_2 in the melt increases from 1 wt% to 1.25 wt% when 20% crystallization has occurred.

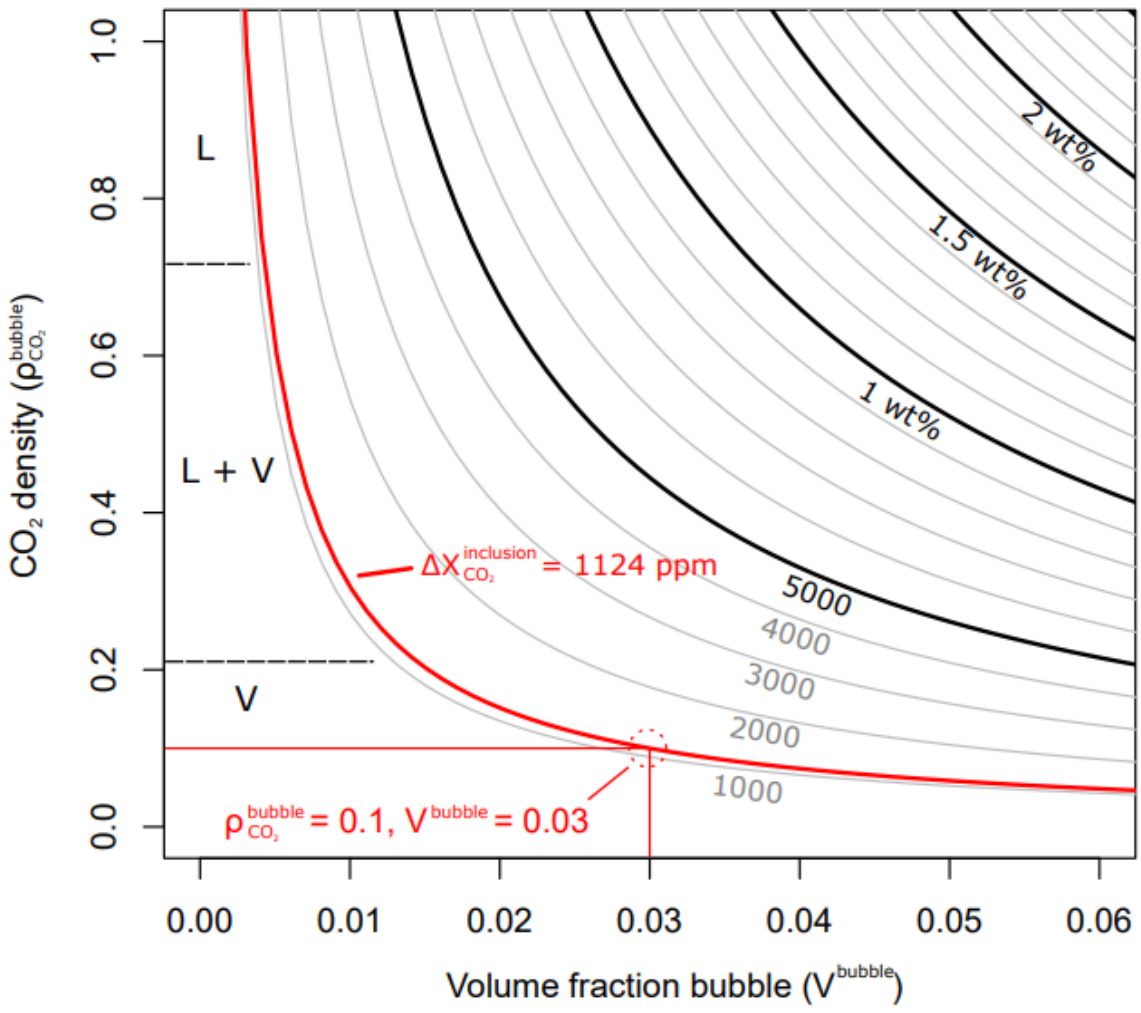

Figure 4: CO_2 contained in melt inclusion fluid bubbles ($\Delta X_{CO_2}^{inclusion}$) calculated as a function of the bubble volume fraction (V^{bubble}), the density of CO_2 in the bubble ($\rho_{CO_2}^{bubble}$; Eq. 7), and the density of the glass ($\rho^{glass} = 2.75\ g/cm^3$). Dashed lines indicate the range of CO_2 densities that correspond to liquid and vapor CO_2. Red lines indicate the amount of CO_2 typical in melt inclusions from Kilauea (Moore et al., 2015). When the CO_2 contained in a bubble occupying 3% of the inclusion volume and containing CO_2 vapor with a density of 0.1 g/cm^3 is added to the CO_2 dissolved in the glass, the total CO_2 concentration of the inclusion is increased by 1124 ppm

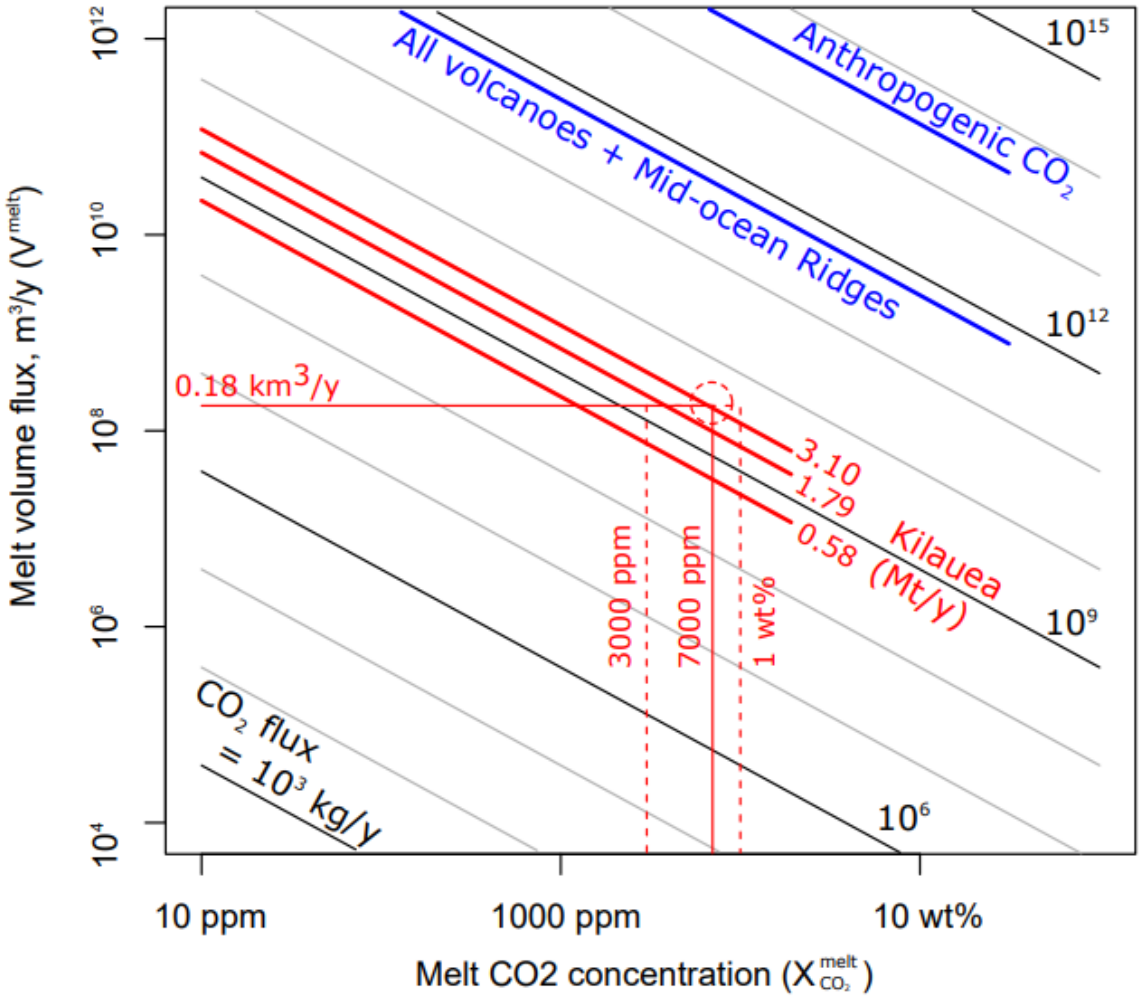

Figure 5: The relationship between volcanic CO_2 fluxes, melt volume flux, and melt CO_2 concentration. Vertical lines indicate melt CO_2 concentrations associated with Kilauea, the horizontal line indicates the melt volume flux estimate from Cayol et al. (2000), and diagonal lines (red) indicate CO_2 fluxes estimated for Kilauea based on remote sensing methods (Greenland et al., 1985; Gerlach et al., 2002; Hager et al., 2008). Anthropogenic CO_2 flux (Friedlingstein et al. 2010) and total volcanic CO_2 flux (Burton et al; 2013) are also shown for reference. Given a melt volume flux of 0.18 km^3/y, the 3.1 Mt/y CO_2 flux of Kilauea corresponds to a CO_2 concentration of ~7000 ppm (Eq. 8). Given the same melt volume flux, the melt CO_2 concentration of 3000 ppm estimated from melt inclusions is consistent with a lower volcanic CO2 flux than 3.1 Mt/y, and the concentration of 1 wt% from used the previous examples is consistent with a higher CO_2 flux.

Chapter 2: Volatile contents of primitive bubble-bearing melt inclusions from Klyuchevskoy volcano, Kamchatka: Comparison of volatile contents determined by mass-balance versus experimental homogenization

Abstract

Primitive olivine-hosted melt inclusions provide information concerning the pre-eruptive volatile contents of silicate melts, but compositional changes associated with post-entrapment processes (PEP) sometimes complicate their interpretation. In particular, crystallization of the host phase along the wall of the melt inclusion and diffusion of H^+ through the host promote CO_2 and potentially S or other volatiles to exsolve from the melt into a separate fluid phase. Experimental rehomogenization and analysis of MI, or a combination of Raman spectroscopy, numerical modeling, and mass balance calculations are potentially effective methods to account for PEP and restore the original volatile contents of melt inclusions. In order to compare these different approaches, we studied melt inclusions from a suite of samples from Klyuchevskoy volcano (Kamchatka Arc) for which volatile compositions have been determined using experimental rehydration, Raman spectroscopy, and numerical modeling. The maximum CO_2 contents of melt inclusions are in agreement (~3600-4000 ppm), regardless of the method used to correct for CO_2 in the bubble, but significantly more uncertainty is observed using mass balance calculations. This uncertainty is largely due to the lack of precision associated with the petrographic method of determining bubble volumes and may also be related to the presence of daughter minerals at the glass-bubble interface.

Introduction

Information concerning the pre-eruptive volatile contents of magmas provides important constraints on local volcanic processes and global cycling of various elements in the Earth system. For example, the pre-eruptive concentrations of CO_2 and H_2O in the melt affect the depth and intensity of volcanic degassing and the explosivity of volcanic eruptions (Metrich & Wallace, 2008). Mantle temperatures can be estimated based on the H_2O concentration in the melt (Sobolev and Danyushevsky, 1994; Portnyagin et al., 2007; Gazel et al., 2012), and the CO_2 content of a melt may be related to the

composition of the source lithology (e.g. anhydrous vs carbonated peridotite). The CO_2 concentrations of early-forming melts also have implications regarding the amount of CO_2 subducted into the mantle (e.g. Wallace et al., 2005), how deep carbon-bearing phases are subducted (Dasgupta et al., 2013), and how much subducted carbon eventually outgasses into the atmosphere (Burton et al., 2013). Much of our knowledge about magmatic volatile budgets comes from remote sensing and *in situ* sampling at active volcanoes (Burton et al., 2013). While these methods are effective for active volcanic systems, they cannot be applied to extinct or dormant volcanic systems. Furthermore, studies of diffuse degassing (e.g. Chiodini et al., 2004) suggest that volatile fluxes from a single point-source may significantly under-estimate the total volcanic degassing flux. As an alternative, melt inclusions preserve samples of pre-eruptive melt and provide a valuable tool for determining the volatile contents and degassing behavior of magmas (Roedder, 1979; Roedder, 1984).

Although melt inclusions can be a robust source of information, various post-entrapment processes (PEP) can modify the composition of the melt inclusions (e.g. glass, fluid) and complicate the interpretation of melt inclusion data to determine the volatile budget of the melt that was trapped in the inclusion. As a result, it is often difficult to determine whether compositional variations within a group of (presumably) coeval melt inclusions reflect local variations in melt chemistry during trapping or reflect processes that have occurred after the melt inclusion formed. For example, when a melt inclusion is trapped, post-entrapment crystallization (PEC) leads to depletion of elements that are compatible in the host mineral (Roedder, 1979; Danyushevsky et al., 2002). Furthermore, because the relative change in molar volume (or density) of the host mineral is less than that of the melt during cooling, the volume change associated with crystallization results in the formation of a "shrinkage bubble," depressurization within the inclusion, and degassing of volatile components (particularly CO_2) into the bubble (Roedder, 1979; Esposito et al., 2011; Moore et al., 2015; Aster et al., 2016). Additionally, it has also been shown that H_2O can be lost from olivine-hosted melt inclusions as the inclusion cools (Roedder, 1979; Sobolev & Danyushevsky, 1994) as a result of diffusion of H^+ across point defects in the host mineral (Mironov & Portnyagin, 2011; Gaetani et al., 2012). Thus, it is necessary to correct the volatile concentrations of

melt inclusions to obtain the original concentration in the trapped melt, and a range of experimental and numerical methods have been used to do this. These include reversing changes that occurred during cooling experimentally by re-heating the melt inclusion and using a combination of microanalytical techniques, numerical modeling, and mass balance calculations to reconstruct the bulk composition of the trapped melt.

In the experimental approach, melt inclusions are heated and homogenized (dissolution of all solid and volatile phases to produce a homogeneous melt/glass, in ideal cases) under controlled temperature, pressure, and oxygen fugacity. This may include optical monitoring of the melt inclusion during heating on a microscope-mounted heating stage, heating in a tube furnace at one atmosphere, or heating in either a cold-seal or internally-heated pressure vessel (Student and Bodnar, 1999). While experimental homogenization works well for inclusions trapped at temperatures less than ~1000°C and hosted in quartz (Bodnar and Student, 2006), melt inclusions trapped at higher temperatures and hosted in olivine and some other phases are often problematic – especially for inclusions that are relatively H_2O-rich (see Esposito et al., 2012). It has been shown that melt inclusions lose more H_2O during longer heating experiments (Massare et al., 2002; Severs et al., 2007; Bucholz et al., 2013). The change in density of the melt resulting from H^+ diffusion causes depressurization to occur, promotes the formation of shrinkage bubbles, and results in a homogenization temperature that exceeds the original trapping temperature (Danyushevsky et al., 2002). Thus, a consequence of H^+ diffusion is that H_2O-rich olivine-hosted melt inclusions often contain a bubble after 1 atm reheating experiments, and overheating the inclusion beyond the trapping temperature would compromise the composition of the inclusion by dissolving excess olivine into the melt. To solve this problem, Mironov et al. (2015) describe a method in which melt inclusions are heated in a pressure vessel in the presence of a hydrous glass under conditions similar to those presumed to be present when the melt inclusions were trapped (Mironov & Portnyagin, 2011). Because of the experimentally-generated water fugacity gradient, H_2O diffuses into the melt inclusions and rehydrates the melt to its original H_2O content, and samples are rapidly quenched (~150°C/s) to prevent diffusive loss of H_2O following the experiment. As a result, CO_2 and other volatiles dissolve back into the melt at the temperature of trapping and do not require overheating.

As an alternative to the experimental approach, it is sometimes desirable to reconstruct the bulk compositions of melt inclusions without reheating them, such as when there is a need to avoid damaging a precious sample (e.g. Harvey & McSween et al., 1992; Goodrich et al., 2013), to preserve chemical gradients that record information about kinetically-limited processes, (e.g. Newcombe et al., 2014), or because the equipment required for controlled heating experiments are unavailable. In these cases, the composition of the trapped melt can be reconstructed by determining the compositions and relative proportions of the various phases in the inclusion and estimating the bulk composition of the melt inclusion using a mass balance approach. Then, a numerical approach may be used to account for the effects of post-entrapment crystallization by incrementally adding host phase back into the melt until the calculated composition of the melt is in equilibrium with the host. This method works best with samples erupted as fine-grained tephras because H_2O loss is limited by the relatively rapid cooling (Lloyd et al., 2013) and inclusions that contain only glass ± vapor. It has been demonstrated in several recent studies that the CO_2 content of glassy, bubble-bearing melt inclusions can be determined based on Raman analysis (Esposito et al., 2011; Hartley et al., 2014; Moore et al., 2015; Aster et al., 2016) or cryometric analysis (Naumov et al., 2006) of the vapor bubble combined with other *in situ* microbeam analyses to determine the major, trace, and volatile composition of the glass. Additionally, the composition and density of the fluid exsolved into the bubble over the cooling interval between trapping and eruption can be estimated by numerical modeling (e.g. Anderson & Brown, 1993, Wallace et al., 2015; Aster et al., 2016).

Because of the benefits listed above, the approach of using mass-balance calculations to restore the CO_2 contents of unheated melt inclusions erupted in tephras is gaining acceptance, but there are a few notable disadvantages associated with this approach. For example, uncertainties incurred by mass-balance calculations associated with the method are not well understood. Previous studies have reported that minerals containing C, H, S, F, and Cl commonly form at the glass-vapor interface in melt inclusions (e.g. Kamenetsky et al., 2002; Esposito et al., 2016), but these minerals are rarely considered in studies to determine the composition of the vapor phase and/or the volatile content of melt inclusions (Kamenetsky et al., 2007; Moore et al., 2015; Esposito

et al., 2016). Additionally, restricting sampling to fresh tephras and lavas with rapidly-quenched inclusions limits the availability, quality, and representativeness of sample material. For these reasons, it is useful to compare the compositions of unheated melt inclusions to inclusions that have been experimentally treated, but there are few studies have directly compared results from the Raman mass-balance approach with compositions determined after experimental homogenization (e.g. Wallace et al., 2015). To explore the relative merits of both approaches, we used Raman analyses and a mass balance approach following the methods described by Moore et al. (2015) to analyze melt inclusions from a suite of samples from the Klyuchevskoy volcano, (Kamchatka). Previous studies (Mironov & Portnyagin, 2011; Mironov et al., 2015) determined the compositions of these same and similar melt inclusions after experimentally rehydrating and homogenizing the inclusions. We also use the method described by Wallace et al. (2015) to numerically estimate the amount of CO_2 exsolved into the bubbles.

Sample description

The melt inclusions analyzed in this study are hosted by olivine (Fo > 84) from lava and tephra samples from the eruption that formed the ~3 ka Bulochka cinder cone (V. Ponomavera, personal communication) on the flank of Klyuchevskoy volcano in the Kamchatka arc. The inclusions in this study are separated into three groups according to their host lithology and method of study: 1) unheated (as found) inclusions in olivines that had been separated from tephra samples, 2) recrystallized melt inclusions in olivine from a lava flow that were heated at 1 atm under dry conditions (Mironov & Portnyagin, 2011), and 3) inclusions from the same lava flow that were heated at ≥300 MPa in the presence of a hydrous glass (Mironov et al., 2015). Hereafter, these samples are referred to as *unheated, dry reheated*, and *experimentally rehydrated,* respectively. The proportion of CO_2 contained in the bubble was determined for all three groups using Raman spectroscopy. We present new analyses of the inclusion glass in the unheated group only; previously reported glass compositions are used for dry reheated and experimentally rehydrated groups (Mironov & Portnyagin, 2011 and Mironov et al., 2015 respectively).

Melt inclusions from the *unheated* tephra samples were prepared by polishing olivine crystals to expose the glass without breaching the bubble, as described by Moore et al. (2015). The splitting of the Fermi diad (Δ, cm^{-1}) could be quantified in approximately 95% of the inclusions analyzed. Vapor bubbles were analyzed by Raman spectroscopy in the Fluids Research Laboratory at Virginia Tech. The major element composition of the glass was determined by electron probe microanalysis in the Electron Beam Laboratory at Virginia Tech. The host olivines in the unheated group have a mean composition of Fo 86.2 and a range of 84.6 to 87.5, which is less primitive than olivines analyzed by Mironov & Portnyagin (2011) and Mironov et al. (2015). The volatile composition of the glass was determined by secondary ion mass spectrometry (SIMS) using the Cameca 1280 ion microprobe at the Woods Hole Oceanographic Institute and the glass standards and calibration protocol described by Shimizu et al. (2009). The program *Petrolog3* (Danyushevshy & Plechov, 2011) was used to apply a correction to the unheated inclusions for Fe-loss and PEC. CO_2 concentrations reconstructed to include CO_2 in the bubble were determined using mass balance calculations as described in Moore et al. (2015).

The major element and volatile composition of the glass phase in *dry reheated* melt inclusions are reported by Mironov & Portnyagin (2011). The studied olivines (Fo 88.5-90.6) were collected from lavas and contain only recrystallized melt inclusions; glassy inclusions that could be analyzed "as found" without reheating were not present. Melt inclusions in olivines from these samples were heated at 1 atm (as described by Mironov & Portnyagin 2011) and contain bubbles after reheating above 1300°C. Unfortunately, the melt inclusions from the original dry reheated group described by Mironov & Portnyagin (2011) were subsequently analyzed using laser ablation by and destroyed. The dry reheated inclusions analyzed by Raman in this study are not the same inclusions for which glass compositions are available from Mironov & Portnyagin (2011), nonetheless they are from the same sample suite and had also been previously reheated as described in that study. The splitting of the Fermi diad (Δ, cm^{-1}) could be quantified in approximately 70% of the inclusions analyzed, and the lower rate of CO_2 quantification may be because the inclusions were in an epoxy multi-grain mount that was not specifically prepared to minimize the depth of the bubbles below the surface.

Major element, volatile contents and host olivine (Fo 85.3-90.9) compositions of the *experimentally rehydrated* melt inclusions are reported by Mironov et al. (2015). Some of the inclusions contain small bubbles because the melt inclusions were variably rehydrated, and we analyzed these using Raman spectroscopy. The experimentally rehydrated melt inclusions were not analyzed (destroyed) using laser ablation and, as a result, we were able to analyze the same inclusions described by Mironov et al. (2015). The amount of CO_2 in the bubble could be quantified in a fewer than half of these inclusions.

A full description of the analytical methods and tables containing melt inclusion compositions used in this study can be found in the supplementary material.

Results and discussion

Volatiles contained in the bubble

In general, bubbles in the dry reheated inclusions are the largest (~4-10 volume percent), bubbles in the experimentally rehydrated inclusions are the smallest (~0-2 volume percent), and bubbles in the unheated melt inclusions are of intermediate size (~2-5 volume percent). The relative uncertainty of the bubble volume is approximately 50% (2σ) based on repeated measurements of the relative bubble volume. For unheated melt inclusions with vapor bubbles occupying 2-5 volume percent of the inclusion, we assume an absolute uncertainty of ±2 volume percent to account for both the uncertainty associated with measuring the dimensions of the inclusion petrographically and the additional uncertainty associated with assuming the unknown third dimension of the inclusion. In some cases, it is reasonable to assume that bubbles larger than about 5 volume percent of the inclusion represent inclusions that have partially decrepitated, trapped a separate vapor phase along with the melt or, alternatively, that the melt inclusion and/or vapor bubble is relatively "flat" (tabular) in shape such that the relationship between the relative area of the bubble and the volume proportion observed under the microscope is different than if the bubble were spherical. For example, a given vapor bubble to total inclusion area that corresponds to 2 volume percent if the bubble and inclusion are both spherical corresponds to 7.4 area percent if the inclusion and bubble are flat (i.e., circles with no third dimension). However, because we did not observe any flattened melt inclusions (i.e. as viewed from the side), and because the bubbles in the dry reheated inclusions are systematically larger than bubbles from the other two groups (Figure 1a), the larger volume fraction of vapor for the inclusions is more likely a result of the nearly complete H_2O loss from the inclusions during their slow cooling in a lava flow and subsequent reheating (Portnyagin et al., 2008; Mironov & Portnyagin, 2011).

The highest CO_2 density is found in bubbles in the experimentally rehydrated inclusions (about 0.2-0.25 g/cm^3), the dry reheated samples tend to have lowest density (about 0.01-0.15 g/cm^3), and the unheated melt inclusions have an intermediate CO_2 density (about 0.1-0.2 g/cm^3). The uncertainty of the CO_2 density is approximately ±0.02 g/cm^3 (2σ) based on replicate analyses, but this value depends on the optical quality of

each sample. Most of the CO_2 densities cluster near or just below the maximum possible density (0.21 g/cm^3) for pure CO_2 vapor at room temperature (Figure 1b).

While the volatile component most often (and easily) detected in the vapor bubbles is CO_2, other volatile components were also recognized. During petrographic examination of the melt inclusions, we often observed small solid phases present at the bubble-glass interface (Figure 2b). Crystals at the bubble-glass interface are often not recognized during normal transmitted light petrography (Figure 2a) and are more easily recognized during petrographic examination in reflected light and/or with cross-polarized light (Figure 2b). We attempted to identify the solid phases using Raman spectroscopy by focusing the laser beam on areas that are visibly covered by crystals and comparing the Raman spectra to known mineral spectra in the RRUFF mineral database (Lafuente et al., 2015). We analyzed the solids at the bubble-glass interface in 15 of the unheated melt inclusions. In three inclusions, a carbonate mineral (likely magnesite) was identified, and in 14 of the bubbles native S, sulfides, and/or sulfates were detected. Figure 2c shows Raman spectra of two melt inclusions in which C- and S-bearing phases were identified. We note that this method of mineral identification provides results that are inconclusive, but our results are consistent with previous observations of daughter minerals in melt inclusions (e.g. Kamenetsky et al., 2002; Esposito et al., 2016). It is not possible to precisely determine the portion of the C and S in the melt inclusions that is contained within crystals that formed at the bubble-glass interface because these crystals have dimensions that approach the limit of optical resolution (≤ 500 nm).

Volatiles contained in the glass

After correcting for PEC, unheated melt inclusions are estimated to contain 54-862 ppm CO_2 (with an outlier at 1528 ppm) and up to ~2.5 wt% H_2O in the glass. The CO2 content is significantly higher than that of the glass in melt inclusions from dry reheated lavas (84-300 ppm CO_2) reported by Mironov & Portnyagin (2011) and lower than the co2 content of the glass in unheated melt inclusions in tephras (979-1198 ppm CO_2) reported by Mironov et al. (2015). H_2O and CO_2 concentrations in the glass show a reasonably good correlation (Figure 3a), which agrees with the conceptual framework described by Mironov et al. (2015) for interpreting compositions of melt inclusions that

have experienced a combination of post-entrapment changes that result in depletion of both H_2O and CO_2 in the glass. According to this model, the CO_2 content of the melt (glass) decreases during post-entrapment crystallization owing to decompression within the inclusion and associated loss of CO_2 to the shrinkage bubble. Dehydration as a result of H^+ diffusion out of the melt inclusion causes the melt to lose both CO_2 and H_2O because CO_2 becomes less soluble and exsolves into the fluid bubble as H_2O is removed from the melt (Mironov & Portnyagin, 2011; Bucholz et al., 2013). These combined effects produce glass compositions that fall within a triangular region in H_2O-CO_2 space where the top corner of the shaded area shown in Figure 3a represents a possible composition of the melt that was originally trapped.

Model reconstruction of volatile contents

Previous studies have described a method to restore volatile contents of bubble-bearing melt inclusions using numerical modeling (Anderson & Brown, 1993; Wallace, 2015; Aster et al., 2016). In this study, we use this approach to provide an independent method for comparison with CO_2 contents obtained using Raman spectroscopy, but this method could be used in other cases to quantify the amount of CO_2 exsolved into bubbles when Raman spectroscopy is unavailable. Therefore, to evaluate this method as a potential alternative for the Raman-mass balance method or experimental rehydration, we used a numerical approach adapted from Wallace et al (2015) to calculate the volatile content of the bubbles in the unheated melt inclusions that were analyzed using Raman spectroscopy.

The inputs for the modeling approach are 1) the major and volatile element composition of the glass, 2) the composition of the host olivine (Fo #), and 3) the whole rock total FeO content of the tephra (Mironov et al., 2015). The program Petrolog3 was used to calculate the temperature interval over which PEC occurred and to calculate the composition of the melt before PEC. We used the olivine-melt model of Ford et al. (1983) and a NNO redox buffer for the PEC calculations. The melt-volatile solubility model of Iacono-Marziano et al. (2012) was used to determine the inclusion pressure and composition of the exsolving fluid at the end of PEC. This is assumed to represent the conditions when diffusion of volatiles into the bubble ceased. We used the empirically

calibrated equation of state (EOS) of Duan & Zhang (2006) to calculate the molar volume of the mixed H_2O-CO_2 fluid. Molar volume and expansivity data for major element oxides (Lange & Carmichael, 1990; Lange, 1997) and experimentally-determined olivine expansivity data (Bouhifd et al., 1996) were used to calculate the differential volume change of the melt and olivine, respectively, over the PEC temperature interval (i.e. the volume of the exsolved fluid at the end of the cooling interval over which PEC occurs). Finally, the fluid composition, molar volume, and melt/host volume change were used to calculate the amount of CO_2 in the bubble.

The uncertainty associated with this numerical model was estimated by propagating the analytical uncertainty of the melt inclusion glass, host, and bulk rock compositions using a "Monte Carlo" approach. This yielded a propagated uncertainty of ~130 ppm, although this should be considered an underestimate because it does not account for other sources of uncertainty (e.g. experimentally-determined molar volumes, melt-volatile solubility relationships, or other factors such as the rate of CO_2 diffusion in the melt as conditions approach the glass transition).

To evaluate the model results, we compared the amount of CO_2 calculated for each inclusion using the Raman method to the same value calculated using the numerical method while ignoring the concentration of CO_2 measured in the glass (i.e. comparing the contribution of CO_2 from the bubbles only) – this was done to avoid introducing an autocorrelation effect. While the correlation between the calculated and observed CO_2 contents is low ($R^2 = 0.1$), the calculated CO_2 contents are within the analytical uncertainty of those determined by Raman spectroscopy in 14 out of 20 cases. This is based on the assumption that the uncertainty of the Raman method is approximately ±0.1 wt%, and this propagated uncertainty can be mostly attributed to errors associated with determining bubble volumes petrographically. These results suggest that the numerical approach may be used to provide a reasonable estimate of the amount of CO_2 in melt inclusion fluid bubbles if Raman analysis or experimental heating are unavailable. However, 17 of the 20 melt inclusions have calculated CO_2 contents that are lower than the CO_2 content determined using the Raman method, and this may indicate that the model does not account for a significant amount of CO_2 exsolution to the bubble that occurs during quenching. Because the uncertainty associated with petrographically-

determined bubble volumes is a factor that limits our ability to evaluate the model results, we recommend that this uncertainty could be minimized either by 1) rotating the host crystals during polishing so that the inclusions can be viewed from two orthogonal angles to estimate the third dimension, or 2) by using X-ray microtomogrophy (e.g. Gaetani et al., 2017) do determine the volume proportions of bubble-bearing inclusions more precisely, or 3) by using the spindle stage to observe the MI from various orientations (Anderson and Bodnar, 1993).

Discussion

When the melt inclusion compositions are restored to include CO_2 in the bubble, the CO_2 contents of all three groups of samples have maximum CO_2 contents that are approximately 0.4 wt % (Figure 5) which is close to the CO_2 content of completely homogenized inclusions reported by Mironov et al. (2015). In the unheated inclusions, 50-90% of CO_2 is contained in the bubble. In the dry reheated melt inclusions, about 90% of the CO_2 is contained in the bubble assuming an average concentration of 162 ppm CO_2 in the glass as reported by Mironov & Portnyagin (2011); this assumption has a negligible impact on the total CO_2 concentration calculated for the inclusions because the CO_2 concentrations in the glass do not exceed 300 ppm for any of the dry reheated inclusions. In the experimentally rehydrated melt inclusions, 10-20% of the CO_2 is contained in the bubble for those inclusions in which the bubbles have not been completely redissolved into the melt during homogenization. The volumes, densities, and thus the proportion of CO_2 in the melt inclusions contained in the bubble are correlated with the H_2O concentration in the glass (Figure 1), which also supports the hypothesis that the amount of CO_2 remaining in the glass is controlled by H^+ diffusion.

Although the maximum CO_2 contents of unheated, dry reheated and experimentally rehydrated melt inclusions are similar, many of the unheated inclusions contain significantly less CO_2 than the experimentally rehydrated inclusions, even after the CO_2 in the bubble has been added to the glass. This discrepancy may reflect either a post-entrapment process involving formation of carbonates at the bubble-glass interface (thus sequestering some of the CO_2 as carbonate) or a pre-entrapment effect like

degassing of the melt between the time when the experimentally rehydrated and unheated melt inclusions were trapped.

To evaluate the possibility that CO_2 in the unheated melt inclusions was sequestered by carbonates, we systematically analyzed the surface of each bubble using Raman spectroscopy. Carbonates were only detected in ~20% of the inclusions analyzed, and there was no observed correlation between the presence of a carbonate peak and the calculated CO_2 content. Furthermore, if carbonate daughter crystals were pervasive in the unheated melt inclusions, then we would expect that the amount of CO_2 calculated by the numerical model would be significantly higher than the CO_2 content determined from Raman analysis, but this was not the case. For these reasons, it is unlikely that the lower CO_2 contents observed in the unheated melt inclusions can be attributed solely to formation of carbonate daughter crystals.

Alternatively, it is possible that the unheated melt inclusions could have been trapped after a significant amount of degassing had occurred. The olivine host compositions of the experimentally rehydrated and dry reheated lava samples are slightly more primitive than the unheated tephra samples (Figure 3b). This suggests that a small amount of crystallization and degassing could have occurred before the unheated melt inclusions were trapped (as discussed by Mironov & Portnyagin, 2011). Unfortunately, to evaluate this possibility more fully, it would be necessary to compare the relationships of other volatile components, which in this case have been compromised by H_2O loss and the formation of S-bearing (and potentially Cl-bearing) daughter crystals.

Summary and Recommendations

Three different methods have been tested to reconstruct the volatile contents of melt inclusions in olivine from the Klyuchevskoy volcano, including analysis of (1) unheated (as found) inclusions in olivines from tephra samples (referred to as *unheated MI*), 2) inclusions in olivine from a lava flow that were heated at 1 atm under dry conditions (referred to as *dry reheated MI*), and 3) inclusions from the same lava flow that were heated at ≥300 MPa in the presence of a hydrous glass (referred to as *experimentally rehydrated MI*). In the case of this study, our results indicate that all three methods are effective for determining the original CO_2 contents of bubble-bearing melt

inclusions, but there are clear advantages and disadvantages associated with each of these approaches (listed in Table 1). Because of these differences, we suggest that a robust melt inclusion dataset will include both melt inclusions that have been analyzed "as found" and melt inclusions that have undergone experimental treatment. Uncertainties associated with mass balance calculations are particularly problematic, and further work will be necessary to increase the precision with which the relative proportions and glass and fluid can be determined. For example, Gaetani et al. (2017) recently demonstrated that it is possible to precisely determine the volumes of the vapor bubble and the glass using X-ray microtomography. This approach is promising and should be adopted when possible. The presence of volatile-bearing daughter minerals is also problematic: even in cases where melt inclusions are quenched quickly, carbonates and other daughter minerals that form on the surface of the bubble may alter the volatile element distribution within the inclusion. It is likely that reheating inclusions (dry reheating or rehydration) will cause these daughter minerals to re-dissolve in the melt, but is not clear 1) whether these daughter minerals may re-form during or after quenching, and 2) whether other volatile elements may remain as a fluid phase after reheating (e.g. SO_2). Thus, we recommend additional studies to compare the volatile compositions of naturally quenched and reheated melt inclusions from rapidly cooled tephra samples to determine the stability limits of these daughter crystals and the kinetics of their formation during and after cooling. Finally, while numerical modeling may be a good alternative for *in situ* analysis of fluid bubbles, further sensitivity analysis and validation of the model using melt inclusions with a greater range of compositions will be necessary to improve this approach.

Acknowledgements

This work was supported by NSF grants EAR-1802012, EAR-1249412, and OCE-1756349 to EG and 1624589 to RJB. A contribution from the Vernadsky Institute core funding to NM and MP (theme AAAA-A16-116030110015-7) is kindly acknowledged. Charles Farley provided technical assistance with Raman analyses. Brian Monteleone and Nobu Shimizu provided technical assistance with SIMS analyses. Luca Fedele and Robert Tracy provided technical assistance with EPMA analyses. LM wishes

to thank Jarek Trela for his help and support during SIMS and EPMA analyses. We thank Leonid Danyushevsky and an anonymous reviewer for their suggestions, which greatly improved the quality of this manuscript.

References

Anderson, A.J., Bodnar, R.J. (1993) An adaptation of the spindle stage for geometric analysis of fluid inclusions, American Mineralogist, 78, 657-664.

Anderson, A.T. and Brown, G.G. (1993) CO_2 contents and formation pressures of some Kilauean melt inclusions. American Mineralogist, 78, 794-803.

Aster, E.M., Wallace, P.J., Moore, L.R., Watkins, J., Gazel, E., Bodnar, R.J. (2016) Reconstructing CO_2 concentrations in basaltic melt inclusions using Raman analysis of vapor bubbles. JVGR, 323, 148-162.

Bodnar, R.J. and Student, J.J. (2006) Melt inclusions in plutonic rocks: Petrography andmicrothermometry. Melt Inclusions in Plutonic Rocks (J. D. Webster, ed.), Mineralogical Association of Canada, Short Course 36, 1-26.

Bouhifd, M.A., Fiquet, A.G., and Richet, P. (1996) Thermal expansion of forsterite up to the melting point. Geophysical Research Letters, 23, 10, 1143-1146.Bouhifd, M. A., Besson, P., Courtial, P., Ge´rardin, C., Navrotsky, A., and Richet, P. (2007) Thermochemistry and melting properties of basalt. Contributions to Mineralogy and Petrology, 153, 689–698.

Bucholz, C.E., Gaetani, G.A., Behn, M.D., and Shimizu, N., (2013) Post-entrapment modification of volatiles and oxygen fugacity in olivine-hosted melt inclusions. Earth & Planetary Science Letters, 374, 145-155.

Burton, M.R., Sawyer, G.M., Granieri, D. (2013) Deep Carbon Emissions from Volcanoes. Reviews in Mineralogy and Geochemistry, 75, 323-354.

Chiodini, G., Cardellini, C., Amato, A., Boschi, E., Caliro, S., Frondini, F., Ventura, G. (2004) Carbon dioxide Earth degassing and seismogenesis in central and southern Italy. Geophysical Research Letters, 31.

Danyushevsky L.V., McNeill, A.W., and Sobolev, A.V. (2002) Experimental and petrological studies of melt inclusions in phenocrysts from mantle-derived magmas: an overview of techniques, advantages and complications. Chemical Geology, 183, 5-24.

Danyushevsky, L.V. and Plechov, P. (2011) Petrolog3: Integrated software for modeling crystallization processes." Geochemistry, Geophysics, Geosystems, 12, 7, 32 p.

Dasgupta, R. (2013) Ingassing, Storage, and Outgassing of Terrestrial Carbon through Geologic Time. Reviews in Mineralogy and Geochemistry, 75, 183-229.'

Duan, Z.H., Zhang, Z.G. (2006) Equation of state of the H_2O-CO_2 system up to 10 GPa and 2573K: Molecular dynamics simulations with ab initio potential surface. Geochim. Cosmochim. Acta., 70 (9): 2311-2324.

Esposito, R., Bodnar, R.J., Danyushevsky, L.V., de Vivo, B., Fedele, L., Hunter, J., Lima, A., and Shimizu, N. (2011) Volatile evolution of magma associated with the Solchiaro eruption in the Phlegrean Volcanic District (Italy). Journal of Petrology, 52 (12), 2431-2460.

Esposito R., Klebesz, R., Bartoli, M., Klukin, Y., Moncada, D., Doherty, A., Bodnar, R.J. (2012) "Application of the Linkam TS1400XY heating stage to melt inclusion studies" Cent. Eur. J. Geosci, 4(2), p. 208-218.

Esposito, R., Lamadrid, H.M., Redi, D., Steele-MacInnis, M., Bodnar, R.J., Manning, C.E., De Vivo, B., Cannatelli, C., Lima, A. (2016) "Detection of liquid H_2O in vapor bubbles in reheated melt inclusions: Implications for magmatic fluid composition and volatile budgets of magmas?" American Mineralogist, 101, 1691-1695.

Ford, C.E., Russell, D.G., Craven, J.A., and Fisk, M.R. (1983). Olivine-liquid equilibria; temperature, pressure and composition dependence of the crystal/liquid cation partition coefficients for Mg, Fe2+, Ca and Mn. Journal of Petrology 24, 256-265.

Gaetani, G.A., Le Roux, V., Klein, F., Moore, L.R., Bodnar, R.J., Maclennan, J. (2017) "X-ray microtomography-based reconstruction of total CO_2 in olivine-hosted melt inclusions" Goldschmidt 2017 Abstract.

Gaetani, G., O'Leary, J., and Shimizu, N. (2012) Post-entrapment changes to H_2O and CO_2 in olivine-hosted melt inclusions. Mineralogical Magazine, 75, 879.

Goodrich, C.A., Treiman, A.H., Filiberto, J., Gross, J., Jercinovic, M. (2013) K2O-rich trapped melt in olivine in the Nakhla meteorite: Implications for petrogenesis of nakhlites and evolution of the Martian mantle. Meteoritics & Planetary Science, 12, 2371-2405.

Hartley, M.E., Maclennan, J., Edmonds, M., and Thordarson, T. (2014) Reconstructing the deep CO_2 degassing behavior of large basaltic fissure eruptions. Earth and Planetary Science Letters, 393, 120-121.

Harvey, R.P., McSween, H.Y. (1992) The parent magma of the nakhlite meteorites: Clues from melt inclusions. EPSL, 111, 467-482.

Iacono-Marziano, G., Morizet, Y., Le Trong, E., Gaillard, F. (2012) New experimental data and semi-empirical parameterization of H_2O–CO_2 solubility in mafic melts, Geochimica et Cosmochimica Acta, 97, 1-23.

Kamenetsky, V.S., Davidson, P., Mernagh, T.P., Crawford, A.J., Gemmell, J.B., Portnyagin, M.V., and Shinjo, R. (2002) Fluid bubbles in melt inclusions and pillow-rim glasses: high-temperature precursors to hydrothermal fluids? Chemical Geology, 183, 349-364.

Kamenetsky, V.S., Pompilio, M., Metrich, N., Sobolev, A.V., Kuzmin, D.V., and Thomas, R. (2007) Arrival of extremely volatile-rich high-Mg magmas changes explosivity of Mount Etna. Geology, 35 (3), 255-258.

Lafuente, B., Downs, R.T., Yang, H., Stone, N. (2015) The power of databases: the RRUFF project. In: Highlights in Mineralogical Crystallography, T Armbruster and R M Danisi, eds. Berlin, Germany, W. De Gruyter, pp 1-30.

Lange, R.A. (1997) "A revised model for the density and thermal expansivity of K_2O-Na_2O-CaO-MgO-Al_2O_3-SiO_2-liquids from 700 to 1900 K: Extension to crustal magmatic temperatures" Contributions to Mineralogy and Petrology, 130, 1-11.

Lange, R.A., Carmichael, I.S.E. (1990) "Thermodynamic properties of silicate liquids with emphasis on density, thermal expansion, and compressibility." Reviews in Mineralogy, 24, 25-59.

Lloyd, A.S., Plank, T., Ruprecht, P., Hauri, E.H., and Rose, W. (2013) Volatile loss from melt inclusions in pyroclasts of differing sizes. Contributions to Mineralogy and Petrology, (published online) online 28 September 2012.

Massare, D., Metrich, N., and Clocchiatti, R. (2002) High-temperature experiments on silicate melt inclusions in olivine at 1 atm: inference on temperatures of homogenization and H_2O concentrations. Chemical Geology, 183, 87-98.

Metrich, N. and Wallace, P.J. (2008) Volatile abundances in basaltic magmas and their degassing paths tracked by melt inclusions. Reviews in Mineralogy & Geochemistry, 69, 363-402.

Mironov, N.L., Portnyagin, M.V. (2011) H_2O and CO_2 in parental magmas of Kliuchevskoi volcano inferred from study of melt and fluid inclusions in olivine. Russian Geology and Geophysics, 52, 1353-1367.

Mironov, N., Portnyagin, M., Botcharnikov, R., Gurenko, A., Hornle, K., Holtz, F. (2015) Quantification of the CO_2 budget and H_2O–CO_2 systematics in subduction-zone magmas through the experimental hydration of melt inclusions in olivine at high H_2O pressure. EPSL, 425, 1-11.

Moore, L.R., Gazel, E., Tuohy, R., Lloyd, A.S., Esposito, R., Steele-MacInnis, M., Hauri, E.H., Wallace, P.J., Plank, T., Bodnar, R.J. (2015) Bubbles matter: An assessment of the contribution of vapor bubbles to melt inclusion volatile budgets, American Mineralogist, 100, 806-823.

Naumov, V.B., Portnyagin, M.V., Tolstykh, M.L., Yarmolyuk, V.V. (2006) Chemical Composition and Crystallization Conditionsbof Trachybasalts from the Dzhida Field, Southern Baikal Volcanic Area: Evidence from Melt and Fluid Inclusions, Geochemistry International, 44, 3, pp. 286-295.

Newcombe, M.E., Fabbrizio, A., Zhang, Y., Ma, C., Le Voyer, M., Guan, Y., Eiler, J.M., Saal, A.E., Stolper, E.M. (2014) Chemical zonation in olivine-hosted melt inclusions, Contrib. Min. Pet., 168, 1030.

Portnyagin, M.V., Hoernle, K., Plechov, P.Y., Mironov, N.L. and Khubunaya, S.A., 2007. Constraints on mantle melting and composition and nature of slab components in volcanic arcs from volatiles (H_2O, S, Cl, F) and trace elements in melt inclusions from the Kamchatka Arc. Earth Planet. Sci. Lett., 255(1-2), 53-69.

Portnyagin, M., Almeev, R., Matveev, S., Holtz, F. (2008) Experimental evidence for rapid water exchange between melt inclusions in olivine and host magma, EPSL, 272, p. 541-552.

Roedder, E. (1979) Origin and significance of magmatic inclusions. Bulletin de Mineralogie, 102, 467-510.

Roedder, E. (1984) Fluid Inclusions. Mineralogical Society of America, Reviews in Mineralogy, v. 12, 644 p.

Severs M.J., Azbej, T., Thomas, J.B., Mandeville, C.W., Bodnar, R.J. (2007) Experimental determination of H_2O loss from melt inclusions during laboratory heating: Evidence from Raman spectroscopy, Chemical Geology, 237, 358–371.

Shimizu, K., Shimizu, N., Komiya, T., Suzuki, K., Maruyama, S., Tatsumi, Y., (2009) "CO_2-rich komatiitic melt inclusions in Cr-spinels within beach sand from Gorgona Island, Colombia" Earth and Planetary Science Letters, 288, 33–43.

Sobolev, A.V., Danyushevsky, L.V. (1994) Petrology and geochemistry of boninites from the north termination of the Tonga Trench: constraints on the generation conditions of primary high-Ca boninite magmas. Journal of Petrology, 35, 1183-1211.

Student, J.J., Bodnar, R.J. (1999) Synthetic Fluid Inclusions XIV: Coexisting Silicate Melt and Aqueous Fluid Inclusions in the Haplogranite–H_2O–NaCl–KCl System. Journal of Petrology, 40, 10, 1509-1525.

Wallace, P.J. (2005) Volatiles in subduction zone magmas: concentrations and fluxes based on melt inclusion and volcanic gas data. Journal of Volcanology and Geothermal Research, 140, 217-240.

Wallace, P.J., Kamenetsky, V.S., Cervantes, P. (2015) Melt inclusion CO_2 contents, pressures of olivine crystallization, and the problem of shrinkage bubbles, American Mineralogist, 100, 787–794.

Figures

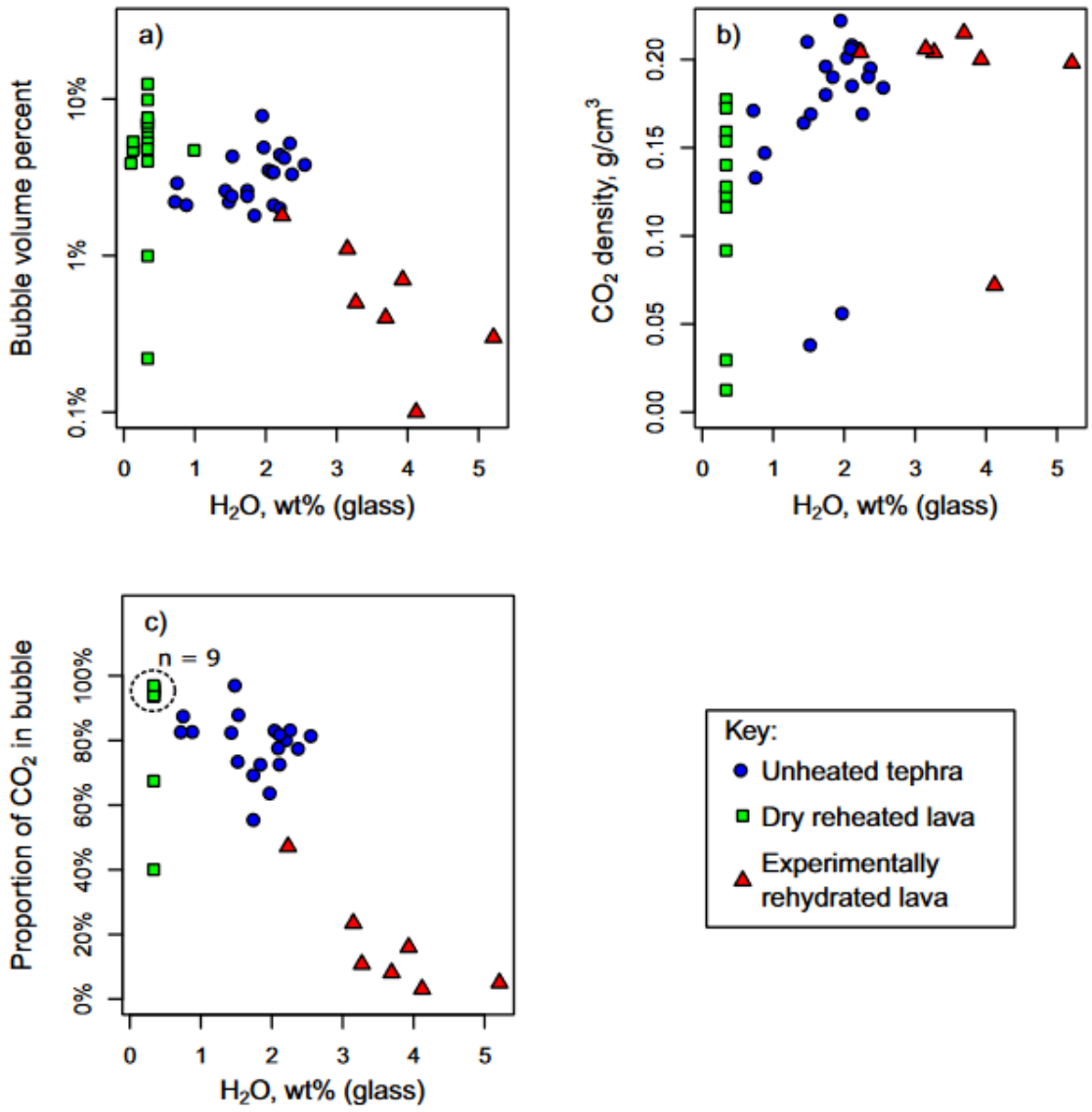

Figure 1: Bubble volume (a), CO_2 fluid density (b), and proportion of total CO_2 in the melt inclusion that is contained in the bubbles (c), plotted as a function of the H_2O concentration in theglass. For dry reheatedinclusions, average glass compositions from Mironov and Portnyagin (2011) were used because inclusion glasses were not analyzed in this study.

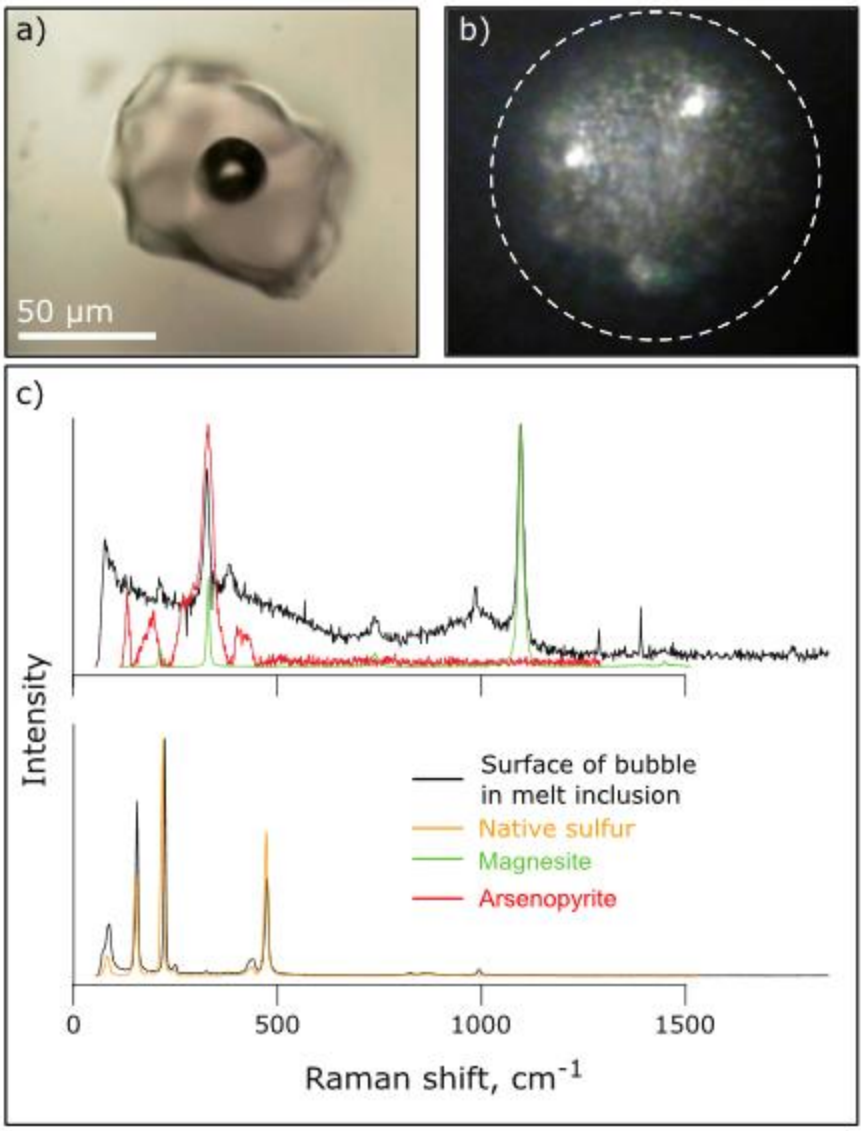

Figure 2: Detection and identification of daughter crystals in unheated melt inclusions. a) A representative photomicrograph of an unheated melt inclusion from this study. b) Photomicrograph of a bubble contained in an unheated melt inclusion from this study. The dashed circle (diameter = 30µm) indicates the outer edge of the bubble. Crystals at the edge of melt inclusion bubbles (on the "top" of the bubble in the photograph) are most easily recognized when viewed under reflected, cross-polarized light as shown. c) Raman spectra of daughter crystals at the bubble-glass interface in unheated melt inclusions. Spectra collected from melt inclusions are shown in black. Spectra of magnesite (green), arsenopyrite (red), and native sulfur (orange) from the RRUFF database (Lafuente et al., 2015) are shown for comparison.

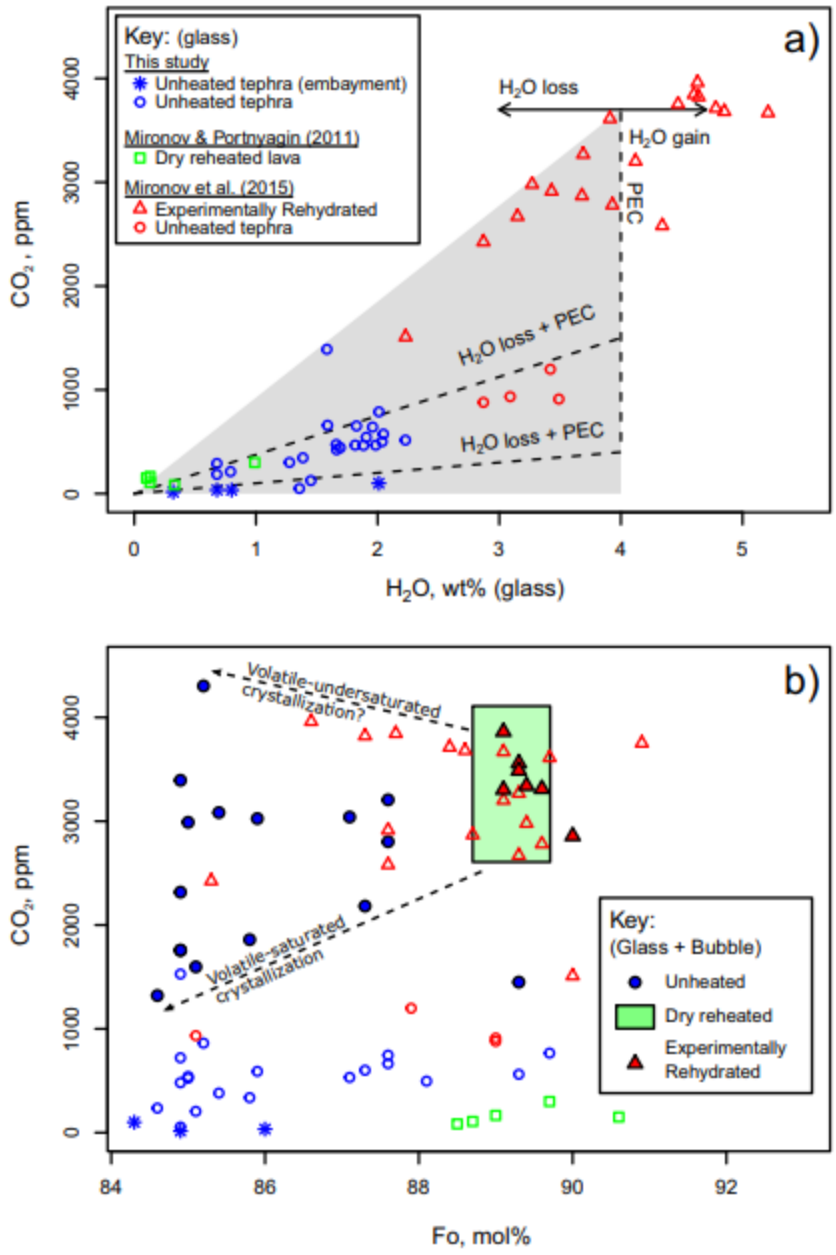

Figure 3: a) H_2O vs CO_2 concentrations of glass in unheated, dry reheated, and experimentally rehydrated melt inclusions and embayments. Arrows qualitatively indicate the direction of compositional change associated with H_2O loss and H_2O gain. The shaded region and black dashed lines show the glass compositions that would be produced after trapping a melt with 4 wt% H_2O and 3800 ppm CO_2 after a combination of post-entrapment crystallization (PEC) and H_2O loss, and CO_2 exsolution into the bubble as described by Mironov et al. (2015). b) Forsterite vs CO_2 concentrations of glass in unheated, dry reheated, and experimentally rehydrated melt inclusions and

embayments. The shaded green box indicates the interquartile range of dry reheated melt inclusion and host forsterite compositions, which were not analyzed for the same inclusion-host pairs.

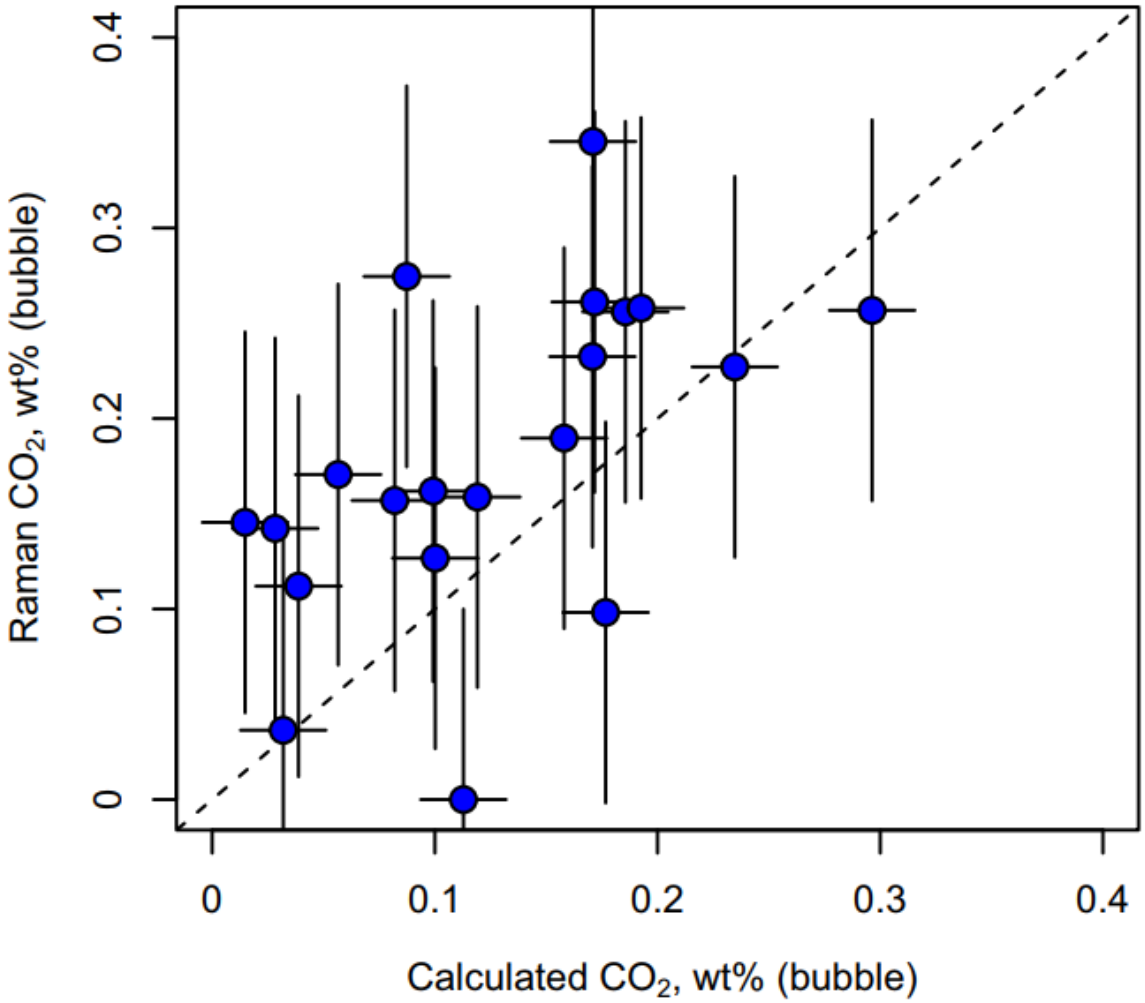

Figure 4: Total CO_2 contents of unheated melt inclusions restored using both Raman spectroscopy and numerical modeling (calculated). Vertical error bars (2σ) represent combined uncertainty from petrographic determination of bubble volumes (± 2 vol%) and CO_2 fluid density from Raman spectroscopy (±0.025 g/cm^3). Horizontal error bars indicate propagated uncertainties from model inputs including melt inclusion glass, host, and bulk rock compositions.

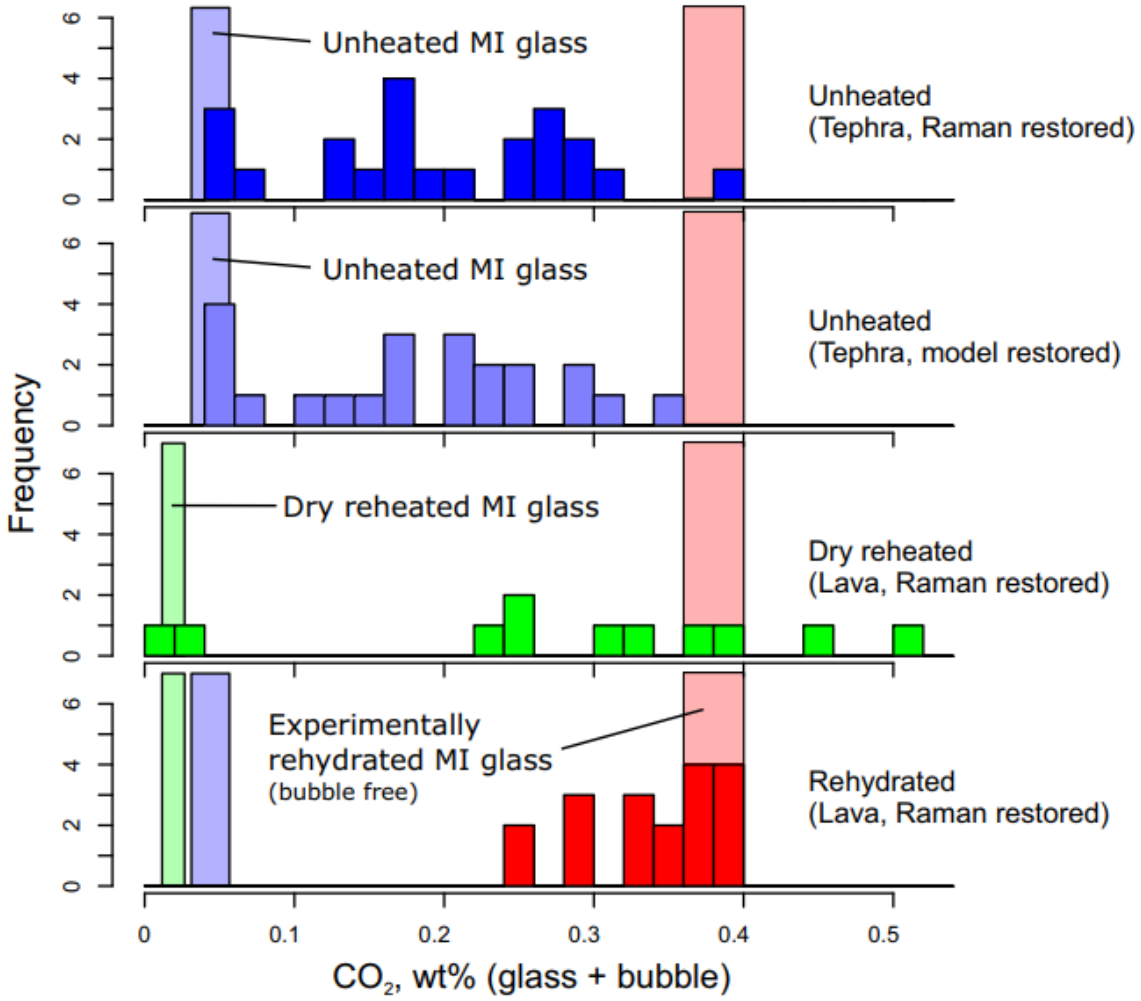

Figure 5: Comparison of CO_2 contents in the glass and CO_2 contents restored using experimental and mass balance methods. Blue and green shaded bars in the background show typical values for CO_2 concentrations in melt inclusion glasses for dry reheated and unheated melt inclusions (interquartile range). Red shaded bars in the background show the range of CO_2 concentrations in bubble-free experimentally-rehydrated melt inclusions reported by Mironov et al. (2015).

Tables

Table 1: Advantages and disadvantages of the various methods used.

Method	Advantages	Disadvantages
Unheated melt inclusions: Identify glassy melt inclusions and analyze "as found"	• Requires minimal sample preparation. • No experimental apparatus or significant experimental expertise are required. • Inclusions are less likely to experience post-entrapment processes and will therefore preserve the original melt composition. • Preserves chemical gradients that provide information about diffusion kinetics	• Requires samples of fresh tephras or lavas with rapidly-quenched inclusions, and may limit the availability of sample material. • Large uncertainties may be associated with CO_2 contents restored using mass balance calculations. • Daughter minerals at the bubble-glass interface may sequester a significant portion of the volatile elements that must be accounted for.
Dry reheated melt inclusions: Identify glassy or recrystallized melt inclusions, reheat at ambient pressure, and analyze	• If, following reheating, the inclusion contains only glass (no crystals or bubbles), initial CO_2 (as well as S and Cl) content of the homogenized inclusion can be determined with high precision using SIMS or FTIR analysis of the glass. • Potentially re-dissolves any carbonates or sulfur-bearing phases that may have formed at the bubble-glass interface back into the melt. • Requires less time and expertise, and does not require sophisticated equipment for high-pressure experiments.	• Requires a one-atmosphere furnace to heat the inclusions and a sealed environment to limit sample oxidation. • Original H_2O contents and chemical gradients that provide information about diffusion kinetics may not be preserved. • Large uncertainties may be associated with CO_2 contents restored using mass balance calculations if a bubble remains after quenching. • Sample material may be damaged or destroyed during the reheating and quenching process. • Significantly dehydrated inclusions usually fail to homogenize.
Experimentally Rehydrated melt inclusions: Identify glassy or recrystallized melt inclusions, reheat under controlled P-T-f_{O2}-a_{H2O}, and analyze	• If, following rehydration, the inclusion contains only glass (no crystals or bubbles), the volatile content of the homogenized inclusion can be determined with high precision using SIMS or FTIR analysis of the glass. • Can be applied to either glassy or partially crystallized MI. • Can be applied to homogenize completely dehydrated inclusions. • Potentially re-dissolves any carbonates or sulfur-bearing phases that may have formed at the bubble-glass interface back into the melt.	• Requires access to a high temperature, high pressure experimental laboratory to conduct rehydration experiments. • To achieve complete homogenization, requires independent estimate of potential P-T-f_{O2}-a_{H2O} conditions of melt inclusion entrapment, or multiple experiments at variable conditions may be required. • Original H_2O contents and chemical gradients that provide information about diffusion kinetics may not be preserved. • Sample material may be damaged or destroyed during the reheating and quenching process.

Supplementary Methods

Samples of unheated melt inclusions were selected and polished at Virginia Tech. Inclusion-bearing grains were selected from pre-separated olivine phenocrysts provided by Maxim Portnyagin, and grains were polished to expose the inclusion glass without breaching the bubble. In some cases in which the bubble was oriented close to the upper edge of the inclusion, the bubble was brought to within ~5 μm of the surface by a first iteration polishing, and then after Raman analysis, the glass and bubble were exposed by a second iteration of polishing. There was no observed correlation between the quality of the CO_2 peaks in the Raman spectrum and whether the glassy part of the inclusion had been exposed.

The volumes of unheated, dry reheated, and experimentally-rehydrated inclusions and their contained bubbles were determined from photomicrographs using image analysis software (as described by Moore et al., 2015). Bubbles were assumed to be spherical, and the volumes were estimated using an average of two orthogonal measurements made through the center of the bubble. Inclusions were assumed to have the shape of an oblate spheroid with the third dimension equal to the shorter of the two measured axes, and volumes were estimated using one measurement made along the longest dimension of the inclusion, and a second measurement made perpendicularly to and halfway along the first. Bubble volume proportions calculated using this method are slightly higher (i.e. the calculated inclusion volume is lower) than if melt inclusions are assumed to be spherical. Our use of an assumed spheroid shape for melt inclusions differs from the approach of Mironov & Portnyagin (2011) in which a spherical shape was assumed, but this discrepancy has a negligible effect on the bubble volume given the relatively large uncertainty associated petrographic estimates of bubble volumes (±1-2 volume percent).

Raman analyses of bubble-bearing unheated, dry reheated, and experimentally rehydrated melt inclusions were conducted using a JY-Horiba LabRam Raman HR spectrometer at the Vibrational Spectroscopy Laboratory at the Virginia Tech Department of Geosciences. Bubbles were analyzed using a 514 nm argon laser focused on the sample using a 150 μm wide slit and 400 μm confocal hole, and a 100x objective lens. A synthetic silicon wafer was used to calibrate the instrument using a peak with a known

Raman shift of 520.5 cm^{-1}. Spectra were collected in a single collection window (i.e. without moving the spectrometer during or between analyses). Raman shifted light was diffracted using an 1800 grooves/mm grating and spectra were collected using a 1024x256 pixel CCD. Raman spectra of daughter crystals at the glass-bubble interface were collected using a 600 grooves/mm grating. The centers of the CO_2 peaks (Fermi diad) in the Raman spectra were determined by using a linear baseline to correct the spectra and then fitting the peaks to a Gaussian curve. The equation of Fall et al. (2011) was used to calculate the CO_2 density from the splitting of the Fermi diad (Δ, cm^{-1}). The uncertainty of our reported densities is estimated to be 0.025 g/cm^3 (2σ) based on replicate analyses of vapor bubbles of different densities.

The H_2O, CO_2, S, Cl, and F concentrations of unheated melt inclusion glasses were determined using secondary ion mass spectrometry (SIMS) at the Woods Hole Oceanographic Institute, Department of Geology and Geophysics, using a Cameca 1280 ion microprobe following the methodology described by Shimizu et al. (2009). Olivine grains containing exposed melt inclusion glass were pressed into an indium medium in a 1-inch diameter aluminum sample holder with a polished piece of the glass standard 529-4-1 and then coated with a 1 nm layer of Au using plasma deposition. Melt inclusion glasses were analyzed using a Cs^+ ion primary beam with a current of 1 nA that was restricted to a 10 µm-wide area using an aperture plate. Counts of ^{12}C, $^{16}O^1H$, ^{32}S, ^{35}Cl, and ^{19}F were normalized to ^{30}Si and converted to H_2O, CO_2, S, Cl, and F concentrations using a linear regression of analyses of 11 glass standards and one nominally volatile-free synthetic forsterite standard. SIMS analyses were checked for drift using replicate analyses of the glass standard 519-4-1. Calibration curves are shown in Figure S1.

Major element concentrations of unheated melt inclusion glasses and host olivine grains were determined by electron probe microanalyses (EPMA) using a Cameca SX-50 Electron Probe Microanalyzer at the Electron Beam Laboratory at the Virginia Tech Department of Geosciences. After SIMS analyses, indium-mounted samples were cleaned and carbon coated using a graphite electrode. EPMA analyses were calibrated using mineral standards and checked for accuracy and corrected for instrument drift using glass standards BCR-2G, BIR-1G, and BHVO-2G. Samples were analyzed using a 15 kV accelerating voltage and by rastering a 10 µm diameter spot. Olivine grains were

analyzed at 3-5 points adjacent to the melt inclusion using a 20 nA beam. Melt inclusion glasses were analyzed using a 10 nA beam to prevent volatilization of alkali elements.

Melt inclusion compositions were corrected for the effects of post-entrapment crystallization (PEC) and Fe-loss using the program *Petrolog3* (Danyushevsky and Plechov, 2011). Calculations used the Ford et al. (1983) olivine-melt model, Lange and Carmichael (1987) melt density model, and a NNO buffer.

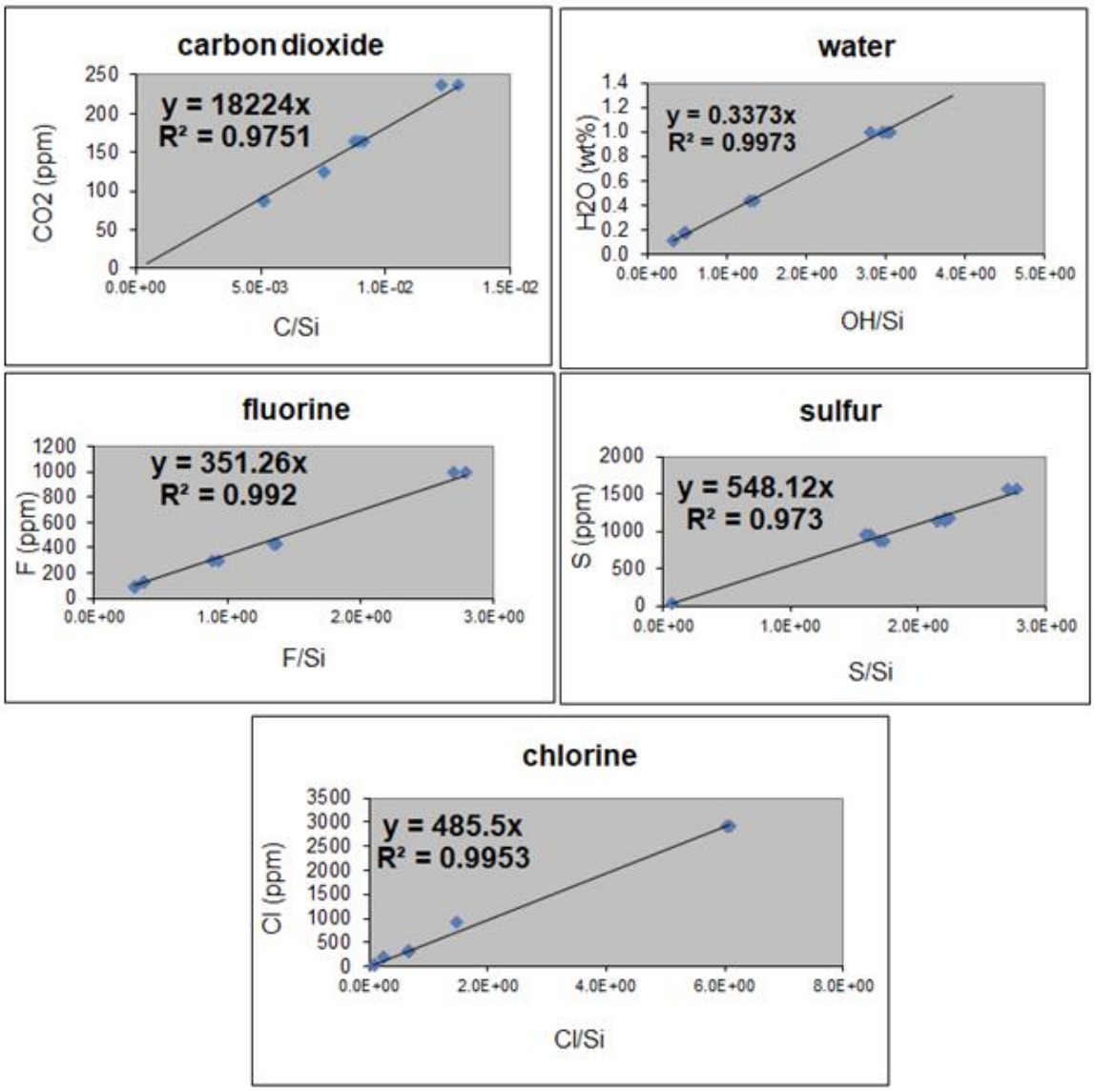

Figure S1: Calibration curves for SIMS analyses based on glass standards described by Shimizu et al. (2009).

Chapter 3: The volatile budget of Hawaiian Magmatism: constraints from melt inclusions from Haleakala Volcano, East Maui, Hawaii

Abstract

Pre-eruptive volatile contents recorded by melt inclusions from ocean island settings such as Hawaii are useful for estimating the extent of deep Earth outgassing on geologic timescales by mantle plume activity. However, melt inclusions trapped from a partially degassed magma will not reflect the original volatile content of the primary melt, and relatively silicic (≳ 45 wt% SiO2) shield-stage tholeiites are more likely to have been affected by degassing during fractionation at shallow depths. In contrast, magmas associated with post-shield volcanoes erupt volatile-rich melts that ascend quickly from the source region and crystallize in deep reservoirs. As a result, melt inclusions from post-shield volcanoes may be more likely to preserve undegassed melt compositions which can be used to determine the primary melt and source volatile contents. In this study, we analyzed melt inclusions from Haleakala Volcano (East Maui, Hawaii) to estimate the volatile budget of Hawaiian post-shield volcanism. Melt inclusions from Haleakala contain up to 1.3 wt% CO_2, 1.2 wt% H_2O, and about 2000 ppm S. We calculate that melts from Haleakala were derived from a primary melt with ~0.7 wt% H_2O and ~0.7 wt% CO_2 and experienced ~15-40% polybaric, fluid-saturated crystallization starting at 5-7 kbar. Post-shield melt inclusions from Haleakala have higher H_2O/Ce and CO_2/Nb compositions than shield-stage melt inclusions from Kilauea, and this suggests that primary melts from Haleakala are derived from a more volatile-rich portion of the composite plume source, compared to those at Kilauea. Integration of our data with geodynamic models suggests that this portion may originate from a sheath around, and at a distance of ~40 km from, the center of plume conduit. Models predict that this material bypasses the main-shield melting zone and supports low-degree (<1%) melting of enriched material at 150~170 km beneath the post-shield volcanoes.

Introduction

Mantle plumes are thought to transfer volatiles from the deep Earth to the surface, and thus represent an important mechanism of planetary outgassing (Dasgupta &

Hirschmann, 2010; Dasgupta, 2013). Many oceanic island volcanoes are situated above mantle plumes which are inferred to rise from the deep lower mantle to the base on the lithosphere to feed hot-spot melting (French & Romanowicz, 2015), and the compositions of the related ocean island basalts (OIBs) have been used to assess the composition of deep mantle materials (Hofmann & White, 1982; Hofmann, 2003). Additionally, alkaline basalts from OIB settings may be derived from partial melting of a CO_2-rich, ultramafic mantle source (Edgar, 1987; Hémond et al., 1994; Dasgupta et al., 2007). Therefore, understanding the nature of plume melting and volcanism – especially alkaline volcanism from OIBs – is crucial to understanding planetary degassing.

Hawaii is perhaps the best-characterized volcanic setting on the planet and is a natural laboratory for studying plume melting. As the Pacific plate moves across the hot spot below Hawaii, the islands that form evolve through a progression of volcanic stages which are characterized by changes in eruptive volume, eruptive style, and melt composition (Peterson & Moore, 1987). Island growth begins with a "pre-shield" seamount stage, which is characterized by a relatively low volume of alkaline melt. This is followed by a voluminous "shield stage" during which most of the volume of the island is generated by the eruption of tholeiitic lava. The output volume of the volcano progressively decreases with time, and erupted melts become more alkaline as the island transitions into a "post-shield" or "capping" stage as deeper and more ephemeral magma chambers develop (Frey, 1990). Volcanic activity may cease entirely after this stage, and the volume of the island decreases with time because material removed by erosion is not replenished by new volcanic material. Intermittent volcanic activity may continue during or after this erosion-dominated period, and islands that have experienced low-volume eruptions of highly alkaline, silica-undersaturated lava after a significant amount of erosion has occurred are said to be in the "rejuvenated" or "post-erosional" stage (Clague & Dalyrimple, 1987).

In addition to geochemical and petrologic variation in volcanic behavior, the Hawaiian plume is also isotopically heterogeneous over space and time. Volcanic edifices have bimodal Pb isotope compositions divided into two parallel groups along the island chain (KEA and LOA compositions; Abouchami et al., 2005). In addition to the LOA and KEA endmember compositions shared by shield-stage melts, rejuvenated and post-shield

stage melts also contain a proportion of an isotopically-depleted, rejuvenated endmember component (DRC; after Bizimis et al., 2013; Phillips et al., 2016), which increases with time based on stratigraphic position and with distance from the hot spot (Garcia et al., 2010; Clague & Sherrod, 2014). Proposed explanations for isotopic variations include progressive incorporation of external oceanic material into the plume with time (e.g. Frey, 1990), or randomly- or laterally-distributed regions of isotopically distinct material within the plume (e.g. Ito & Mahoney, 2005; Hofmann & Farnetani, 2013) which are preferentially sampled depending on the degree of melting (e.g. Garcia et al., 2010), orientation of the plume relative to plate motion (Jones et al., 2017), or temporal variations related to internal mixing within the plume (Ballmer et al., 2013).

While the combined volcano-stage model and geodynamic plume models together provide a robust framework which can explain the geologic and geochemical properties of the Hawaiian islands, the transitions between each stage of growth and their causes are not as well understood. The gradual changes in melt composition between the pre-shield, shield, and post-shield stages can be explained by variable degrees of melting as a function of distance from the hot spot (Liu & Chase, 1991). In contrast, explaining the eruptive hiatus from the post-shield stage to the rejuvenated stage requires additional processes such as crustal flexure (Bianco et al., 2005) and/or secondary melting of mantle source material (Ribe & Christiansen, 1999). However, the transitions between the stages of volcanic activity are gradual rather than punctuated (Clague & Sherrod, 2014), and inferred changes in melt supply may also be accompanied by changes in source composition – even within the same volcanic edifice (Chen et al., 1991; Blichert-Toft et al., 2003; Xu et al, 2005; Garcia et al., 2010).

Geodynamic modelling has suggested that differences in both eruptive behavior and isotopic heterogeneity are related to compositional variation within the plume, which can give rise to complex upwelling behavior and variable melt output (Ballmer et al., 2013) due to the presence of a recycled eclogite component within the plume (Hofmann & Jochum, 1996; Hauri, 1996). This recycled eclogite component is thought to begin melting at depths below ~150 km (Sobolev et al., 2005) and contribute to concentric chemical zonation of the plume observed in the geographic distribution of trace element enrichment of erupted melts (Dixon et al., 2001). In particular, it is thought that the outer

surface of the Hawaiian plume is enriched in volatiles as a result of metasomatism by fluids derived from deep eclogite melting (Dixon et al., 2001; Dixon et al., 2008), and this zonation should be reflected in the volatile budgets of magmas crystallizing at different distances from the center of the plume.

Constraining the volatile budget of melts from the Hawaiian plume is challenging owing to the strong pressure dependence of volatile solubility in silicic melts and the depth at which degassing begins within the volcanic "plumbing system" (e.g. Dixon & Clague, 2001). Multiple remote sensing methods have been deployed to determine the flux of volatiles from Kilauea, but these methods cannot be applied to volcanoes on the older islands, which are not active. The older volcanoes on Hawaii preserve an extensive stratigraphic record of subaerial lava flows and tephra deposits, but bulk samples do not preserve information about the pre-eruptive volatile abundances of the melts. Because of this, dredged submarine basalts have been used to estimate the volatile budget of volcanism at the edge of the Hawaiian plume, but even dredged lavas are generally found to have degassed to a state of equilibrium at the hydrostatic pressure of the seafloor (Dixon et al., 2008). Additionally, interpreting volatile data from submarine samples is challenging because of the potential for seawater assimilation (Dixon et al., 2001).

An alternative approach is to analyze melt inclusions trapped in minerals that crystallized deeper in the lithosphere, which would not have been contaminated by ocean water and which are more likely to preserve information regarding the volatile content of the melt before shallow degassing occurred. In cases where melt inclusions are trapped during degassing at fluid-saturated conditions, the volatile contents of melt inclusions can be used to determine the pressure at the time of crystallization using an experimentally defined volatile-melt solubility relationship. While melt inclusions have been used to estimate the pre-eruptive volatile contents of shield and post-shield stage melts from Hawaii (e.g. Sobolev et al., 2011; Sides et al., 2015; Tucker et al., 2019), obtaining accurate volatile contents is challenging because of CO_2 lost to bubbles which form in the inclusion after trapping (Roedder et al., 1979; Anderson & Brown, 1993; Steele MacInnis et al., 2011; Moore et al., 2015). Tucker et al. (2019) recently reported analyses of melt inclusions from several Hawaiian volcanoes with CO_2 contents determined by using an equation of state to estimate the amount of CO_2 contained in the bubble. In this study, we

use Raman spectroscopy to measure the CO_2 content of melt inclusion bubbles *in situ* to avoid uncertainties associated with nonequilibrium volume exsolution related to contraction of the bubble during eruption as discussed by Wallace et al. (2015) and Moore et al. (2015, 2018). Further details are discussed below and in supplementary material.

To explore the relationship between the volatile budget of Hawaiian volcanoes at different growth stages, we used melt inclusions from Haleakala Volcano to estimate the source volatile content and melt degassing behavior during crystallization. Haleakala is a ~2 million-year old volcanic complex on East Maui that has experienced all of the stages of volcanic growth through the end of the post-shield stage (Sherrod et al., 2003; 2007). The most recent volcanism in Haleakala (~1 Ma to present) consists of monogenetic volcanic vents that cut across a deeply incised erosional surface. However, detailed stratigraphic age dating indicates that Haleakala has yet to experience an eruptive hiatus that is indicative of the transition from post-shield to rejuvenated volcanism, but can be considered to be approaching the end of its post-shield stage based on the duration of post-shield volcanism present on other Hawaiian islands and discrete lapses in volcanic activity evident in the stratigraphic record (Sherrod et al., 2003). Additionally, isotopic compositions of melts from Haleakala's Hana and Kula post-shield volcanism suggest a mixed composition between a KEA-like composition and a depleted composition (Phillips et al., 2016). Haleakala therefore represents the oldest and most distal site of post-shield volcanism on Hawaii with respect to the center of the plume, with a composition influenced by an isotopically-defined depleted rejuvenated mantle endmember component (DRC; e.g. after Bizimis et al., 2013) which also provides opportunities to sample melt inclusions from fresh, monogenetic cinder cones. This is important because rapidly-quenched melt inclusions are less likely to have experienced significant post-entrapment crystallization (Roedder, 1979; Bodnar and Student, 2006; Steele MacInnis et al., 2011) and H_2O loss (Danyushevsky et al., 2002; Lloyd et al., 2013). Because melts from Haleakala are both relatively alkalic and crystallize deep within the lithosphere (Hammer et al., 2016), melt inclusions are more likely to trap a melt that is unaffected by significant degassing. Haleakala is therefore an ideal location to find recently-erupted and unmodified, primitive melt inclusions that sampled melts

derived by partial melting of a volatile-enriched source. The goals of this study are to estimate the conditions under which degassing occurs in the "plumbing system" below Haleakala, to assess whether melt inclusions from Haleakala record evidence of a transition to a volatile-enriched plume source, and to apply information about the volatile content of the source material that is preserved by melt inclusions to improve upon existing models of Hawaiian island evolution.

Materials and Methods

Ash and lapilli samples were collected from post-shield lava flows and monogenetic cinder cones at Haleakala Volcano on Maui, specifically targeting fresh, unaltered material that was likely to contain olivine phenocrysts. Fresh tephra samples were collected from Haleakala crater (Figure 1), and lava samples were collected from Hana volcanic flows (Qhn6) on the southwestern coast of East Maui and from Lahaina Volcanic unit Qlhl on West Maui (Figure 1 inset). Two of the tephra samples (HA-16-6 and HA-16-7; Hana volcanics) were found to contain abundant olivine phenocrysts containing glassy melt inclusions, and these samples were selected for melt inclusion analysis. GPS locations and sample description provided in Table S7 (Supplementary Materials)

Whole rock and melt inclusion samples were crushed, washed in an ultrasonic bath with deionized water, and oven dried at 120°C. Approximately 30 g of the cleaned bulk sample material was hand-picked under a binocular microscope to remove altered material and the cleaned material was analyzed for major and trace elements at Washington State University. Whole rock samples were analyzed using a combination of X-ray fluorescence (XRF) and solution inductively coupled plasma mass spectrometry (methods described by Johnson et al., 1999). New whole rock major and trace element compositions are listed in supplementary tables S1 and S2 respectively.

The remaining sample material was sieved to identify the grain size fraction containing the most abundant olivine grains, and these grains were hand-selected under a binocular microscope. All melt inclusions contained glass and fluid bubbles with some also containing small (< 0.1 volume percent) opaque particles that are likely sulfide globules or spinel crystals. Bubbles were analyzed by Raman spectroscopy at Virginia

Tech using the methods described by Moore et al. (2015). Following Raman analyses, crystals containing melt inclusions were polished to expose the glass at the surface and pressed into a 1-inch diameter indium mount. Volatile concentrations of melt inclusion glasses were determined using Secondary Ion Mass Spectrometry (SIMS) at the Woods Hole Oceanographic Institute (methods described by Shimizu et al., 2009), and major element concentrations of melt inclusion glasses were determined using electron probe microanalyses (EPMA) at Syracuse University. Finally, melt inclusion and host olivine grains were analyzed at Virginia Tech using laser ablation inductively coupled plasma mass spectrometry (LA-ICP-MS) to determine trace element concentrations. Melt inclusion and host olivine major and trace element compositions are listed in supplementary tables S3 and S4, respectively. Volatile contents of melt inclusions are listed in supplementary table S5.

Melt inclusion compositions were corrected for post-entrapment crystallization using the Petrolog3 program (Danyushevsky & Plechov, 2011). For these calculations, we used the Ford et al. (1983) olivine-melt model, the Lange & Carmichael (1990) melt density model, and a QFM buffer to control oxygen fugacity. To correct for Fe-loss, we used the total Fe concentration from whole rock analyses. Melt f_{O2} was estimated for melt inclusions using the V partitioning proxy described by Canil (2002).

After analyzing melt inclusions using LA-ICP-MS, we used the PEC-corrected Al_2O_3 concentration for each inclusion as the internal standard so that the calculated trace element concentrations would reflect a PEC-corrected value. Because of the small size of the melt inclusions (~50 µm), and because the melt inclusions had been previously exposed to the surface by polishing, several of the laser ablation analyses included a mixture of glass and ablated host olivine, and these analyses were discarded as a precaution and because the LA-ICP-MS signal processing algorithm used in this study does not support deconvolution of a mixed host/inclusion signal.

Additional information regarding sample preparation and analytical methods is included in the supplementary methods description.

Results

Major elements

Major element compositions of whole rock samples from Haleakala are consistent with previously analyzed samples from Haleakala (Figure 2) and with other Hawaiian post-shield-stage volcanoes. The compositions are alkalic and plot within the basalt, trachybasalt, and basanite fields on a total alkali vs silica (TAS) diagram. Forsterite contents [Fo# = 100 × molar Mg/(Mg+Fe)] of olivine host phenocrysts range from 68-87, and melt inclusions from one tephra sample (HA-16-6, Fo# 79-87, mean = 82) are significantly more primitive than the other (HA-16-7, Fo# 73-87, mean = 75). Melt inclusions generally experienced ~2-15% (interquartile range) post-entrapment crystallization (PEC), and inclusion major element compositions after correcting for PEC are consistent with the range of whole rock compositions obtained in this study. An exception is that TiO_2 concentrations of melt inclusions are significantly lower than those observed in whole rock analyses, and it is likely that this is the result of TiO_2 partitioning into spinel crystals which were commonly observed within melt inclusions.

Trace elements

Trace element concentrations of lava and tephra whole rock samples from Haleakala are consistent with previous studies of Haleakala and other post-shield-stage volcanoes from Hawaii (Figure 3). Both sample types are enriched in light rare earth elements, which is typical of an OIB derived from a low degree of partial melting. This is in contrast to melts from Haleakala's shield stage, which are generally interpreted to have originated from a higher degree of melting (Chen et al., 1991). Whole rock and melt inclusion samples also show depleted heavy rare earth concentrations, which are generally interpreted to reflect a garnet-bearing source (Wagner et al., 1998; Ren et al., 2004).

Trace element concentrations of melt inclusions are consistent with those observed from whole rock samples (Figure 3). However, the melt inclusion data are significantly more variable than whole rock data. Additionally, two melt inclusions show consistently low trace element concentrations. It is not clear whether these anomalously depleted melt inclusion compositions are a result of olivine host contamination or evidence of a depleted melt composition. Depleted melt inclusion compositions have

been previously reported for melt inclusions from Mauna Loa by Sobolev et al (2011), and were interpreted to reflect interaction between melts derived from recycled oceanic crust and depleted peridotitic mantle. Because the variability of the trace element abundances in melt inclusions increases with increasing compatibility in olivine, it is likely that some of the uncertainty may be related to contamination of the analytical volume by host olivine. Evaluating the effects of these processes on the observed heavy rare earth element concentrations is beyond the scope of this study, and therefore we limit our discussion to exclude the heavy rare earth element concentrations of individual melt inclusions .

Volatile components

Melt inclusions from Haleakala contain 500-2500 ppm F, 200-800 ppm Cl, 700-2500 ppm S, 0.2-1.2 wt% H_2O, and 0.3-1.3 wt% CO_2 (after correcting melt inclusion CO_2 compositions to account for exsolution into shrinkage bubbles, Figure 4a). We note that other volatile components, such as S and H_2O, may have exsolved into fluid bubbles as has been reported previously (e.g. Esposito et al., 2016; Moore et al., 2018), but evidence of other exsolved components either as daughter crystals precipitated on the glass/fluid interface or as a component in the fluid was not observed during Raman analyses of the inclusions considered in this study. We also note that the CO_2-bearing fluid bubbles contained a mixture of liquid and vapor, and melt inclusions were analyzed at ~35 °C so that the fluid analyte would be homogenous during Raman analysis. Further details of this approach are discussed in the supplementary material.

To determine the extent to which the melt had degassed prior to trapping, melt inclusion volatile contents were compared to an incompatible element that is not likely to have been partitioned into a mineral or fluid phase given the compositional range over which olivine-hosted melt inclusions were being trapped. Fluorine was selected as the incompatible element for comparison because it was collected simultaneously with the other volatile elements during SIMS analyses. Cl and F are highly correlated: it is therefore unlikely that the compositions of either of these elements were depleted by degassing during fractional crystallization. S and H_2O are well-correlated with F for inclusions with less than 1000 ppm F and poorly correlated for inclusions with greater

than 1000 ppm F: we interpret this to indicate that both S and H_2O were initially enriched in the melt by fractional crystallization and then depleted by degassing when the melt became volatile-saturated. Additionally, the good correlation between H_2O and F suggests that melt inclusions experienced little diffusive loss of H_2O. Assessing whether CO_2 concentrations of melt inclusions were affected by degassing is more difficult because of the large (~50% relative) uncertainty associated with determining the volume of shrinkage bubbles petrographically. Thus, the variation in CO_2 could potentially be explained either by propagated analytical error or by degassing, and additional information is required to determine whether the population of melt inclusions with F < 1000 ppm trapped a volatile-saturated melt.

The range of volatile contents that we observe is significantly larger than is observed for the shield stage. For comparison, Sides et al. (2014) report that melt inclusions from Kilauea contain to 0.8 wt% H_2O, up to 400 ppm F, 50-250 ppm Cl, and up to 1800 ppm S. Moore et al. (2015) report that melt inclusions from Kilauea contain up to 0.2 wt% CO_2 when the CO_2 contained in shrinkage bubbles is included. This difference in volatile abundances is likely related to a combination of melt inclusion trapping at greater depths (higher pressures), and a less polymerized (i.e. more alkalic) melt composition. It is likely that the concentrations of (incompatible) volatile components in the melt would have been initially higher than those in the shield stage owing to a lower degree of partial melting or the participation of a different source, and then subsequently enriched by fractional crystallization. These processes are evaluated further, as described below.

Oxygen fugacity

To estimate the oxygen fugacity of melts from Haleakala, we used the olivine-melt V-partitioning oxybarometer described by Canil et al (2002), in which the oxygen fugacity of melts is correlated with the V olivine/melt partition coefficient (D_V). For melt inclusions from Haleakala, the range of D_V is ~0.02-0.04, which corresponds to approximately ΔQFM -1 to +0.5 (relative to quartz + fayalite + magnetite buffer at 1200°C) or a ratio of ferric to total Fe ($Fe^{3+}/\Sigma Fe$) of 0.15 to 0.25 (Figure 5). This range is consistent with previous measurements of Fe speciation for Kilauea (Moussallam et al,

2016) and Mauna Kea (Brounce et al., 2017) determined using X-ray absorption spectroscopy. D_V is positively correlated with the composition of the host olivine and is negatively correlated with incompatible elements F and Cl, and poorly correlated with volatile components H_2O, S, and CO_2. This suggests that the oxidation state of the melt, as recorded by the D_V proxy, is controlled by preferential incorporation of Fe^{2+} into crystallizing olivine, and is not significantly affected by degassing.

Primary melt composition modeling

To reconstruct the composition of primary melts derived from initial melting of the mantle source below Haleakala, we used the silica activity thermobarometer of Lee et al. (2009) to incrementally add equilibrium olivine until the calculated melt composition is in equilibrium with mantle olivine. We excluded samples with MgO < 8 wt% from the calculation to assure that only melts crystallizing olivine would be used in our model. We assumed a molar Fe^{3+}/Fe_{total} = 0.2 based on the calculated fO_2 from the D_V oxybarometer described above, $K_d^{Fe/Mg}$ = 0.3, and an assumed mantle Fo# = 90, which is consistent with the most primitive olivines from Maui (Ren et al., 2004). For whole rock samples, we assumed an H_2O concentration of 1.2 wt% based on the range of H_2O concentrations determined for melt inclusions, and crystallizing olivine compositions calculated using the correlation between melt inclusion host olivine composition and Al_2O_3 concentration. Primary melt compositions calculated from whole rock and melt inclusion samples are consistent, and indicate that ~5-30 wt% of olivine fractionation had occurred before melt inclusions were trapped. We used new mass of melt that is based on the calculated amount of olivine addition to the melt to correct volatile and trace element concentrations of primitive (MgO > 8) samples for olivine fractionation assuming perfect incompatibility with respect to the crystallizing melt. This assumption appears to be valid based on linear correlations observed between trace element concentrations and MgO concentration, and a lack of observed correlation between trace element rations and MgO (Figure 6). The observed input and calculated output compositions involved in this calculation are listed in supplementary Table S6. Table 1 lists the average primary melt composition calculated using the Lee et al (2009) thermobarometer, and this composition was used as the (initial) parental melt composition for MELTS models of fractional

crystallization. The average corrected (primary melt) volatile component composition is 400 ppm Cl, 1500 ppm S, 7000 ppm H_2O, and 7000 ppm CO_2.

Discussion

Mineral and fluid fractionation assessment

Previous studies of material erupted from Haleakala suggest that the observed range in major element compositions reflects olivine and pyroxene fractionation at various depths within the lithosphere (Bergmanis et al., 2000; Hammer et al., 2016). We used the program RhyoliteMELTS (Ghiorso et al., 1994) to calculate the range of major element compositions produced by fractional crystallization at conditions appropriate for the Haleakala system. Melt liquid lines of descent (LLDs) were calculated using the parental composition shown in Table 1 and an oxygen fugacity buffered by QFM (within the range estimated using D_V). The starting pressures for the calculations were 3, 5, 7, and 9 kbar, with a decompression rate of 75 bar/°C. Of the various input parameters, the trajectory of the LLDs for a given parental melt composition was most dependent on the initial pressure and decompression rate, while the H_2O concentration of the melt and oxygen fugacity had a minimal impact on the results.

To compare the melt inclusion trapping conditions to the conditions simulated by the model, we used the volatile-melt solubility model of Iacono-Marziano et al. (2012), which is calibrated for alkaline melt compositions similar to those observed in this study, to calculate saturation pressures for the range of observed melt inclusion compositions and compared the results to other pressure constraints. Calculated volatile-melt saturation pressures are ~2 to 7 kbar, which correspond to depths of ~7 to 24 km assuming a 3.5 km/kbar lithostatic pressure gradient. The volatile-melt saturation pressures that we calculate for our melt inclusions are correlated with the forsterite contents of the phenocrysts which host them, and this correlation can be directly compared to the LLDs calculated using RhyoliteMELTS. The LLDs showing olivine composition as a function of pressure calculated based on a 75 bar/°C decompression rate from 3 and 5 kbar starting pressures are consistent with the range of inclusion/host pairs (Figure 4b). Because the crystallization model is both dependent on pressure and consistent with the major element

compositions of the whole rock and melt inclusion samples that we have analyzed, it is likely that the pressures supplied to the model are valid.

To further evaluate whether the melt was volatile saturated when melt inclusions were trapped, we compare our fractional crystallization modeling results and calculated volatile-melt saturation pressures to previous results reported for Haleakala. Previous studies have used petrologic modeling (Bergmanis et al., 2000) and clinopyroxene geobarometry (Chatterjee et al., 2005; Hammer et al., 2016) to determine crystallization depths for magma reservoirs in the lithosphere below Haleakala. Based on petrologic modeling, Bergmanis et al. (2000) report crystallization pressures of ~3 kbar, but Chatterjee et al. (2005) report pyroxene crystallization pressures up to 10 kbar. More recently, Hammer et al. (2016) used an X-ray mapping technique to relate calculated trapping pressures to petrographic features within individual clinopyroxene phenocrysts and grain morphology and report a range of saturation pressures from 3.6 to 7.1 kbar. Furthermore, Hammer et al. (2016) also demonstrate that pressures obtained from pyroxene geobarometry are highly model-dependent, and pyroxene/melt compositions reported by Hammer et al. (2016) and by Chatterjee et al. (2005) yield mutually consistent pressures (up to ~9.5 kbar) when the same model is used.

The range of pressures obtained from pyroxene geobarometry and petrologic modeling described above is consistent with our petrologic modeling results and volatile-melt saturation pressures based on melt inclusions. Thus, the mutual consistency between calculated volatile-melt saturation pressures, pyroxene crystallization pressures, and the observed and modeled range of major element compositions (which are also a function of pressure) strongly suggests that the volatile-melt saturation pressures reflect melt inclusion trapping pressures. If this is the case, then the melt trapped by the melt inclusions must have been volatile-saturated, and it is likely that the volatile concentrations that we report represent the concentrations after some portions of the original volatile budget was lost through degassing.

Source composition constraints from volatile component/trace element ratios

Ratios of volatile components and incompatible trace elements are useful for comparing the volatile contents of melts derived from different environments. H_2O is

thought to have a degree of incompatibility that is similar to that of Ce (Michael et al., 1998). Similarly, Nb is thought to exhibit a similar degree of incompatibility to CO_2 (Saal et al., 2002), but recent experimental evidence suggests that CO_2 may be more incompatible than Nb and have an average mineral/melt partition coefficient in basalts that is closer to that of Ba (Rosenthal et al., 2015). Given that the bulk melt partition coefficients of these volatile/trace element pairs are similar, it is possible to compare the volatile contents of different melt sources in a manner that is not affected by different degrees of melting and crystal fractionation by normalizing volatile elements to an incompatible element with a similar solid/melt partition coefficient. Melts with volatile contents that have been affected by degassing will have depleted volatile/trace element ratios, and this method therefore allows one to estimate the degree to which a melt has been affected by degassing. However, volatile/trace element ratios of melt inclusions from Haleakala (Figure 7) are positively correlated with the forsterite content of the olivine. Because we observe no corresponding relationship between the forsterite content of host olivine crystals and the H_2O and CO_2 contents of melt inclusions, the correlation between volatile/trace element ratios is likely to be a result of enrichment of Ce, Nb, and Ba in the melt by crystal fractionation. This suggests that the volatile/trace element ratios of only our most primitive melt inclusions are suitable for comparing different possible source compositions, and the assumption that these ratios are unaffected by crystal fractionation may not be entirely appropriate in this case.

H_2O/Ce ratios for our melt inclusions are correlated with host Fo content, and approach an average value of ~300 at the host olivine composition Fo# = 90. This ratio is consistent with the range predicted by Dixon et al. (1997) for undegassed basanite and nephelinite North Arch lavas, greater than that of melt inclusions from the East Pacific Rise (EPR) reported by Wanless & Shaw (2012), and greater than the H_2O/Ce ratio of melt inclusions from Kilauea (Sides et al., 2014). The observation that melt inclusions from Haleakala have H_2O/Ce ratios significantly higher than melt inclusions from Kilauea and EPR lavas is consistent with the hypothesis of a more H_2O-rich melt source for Haleakala magmas.

Similarly, CO_2/Nb ratios for our melt inclusions approach a value of ~500, and this is slightly above the range for EPR lavas, and between the ranges for basanite and

alkali olivine basalt from North Arch lavas, and higher than the ratios of melt inclusions from Kilauea with corrected CO_2 concentrations of 2000 ppm (Moore et al., 2015). In contrast, CO_2/Ba for our melt inclusions approaches a value of ~50, and this is consistent with the lower end of CO_2/Ba for basanitic North Arch lavas, and approximately equal to the CO_2/Ba of both EPR lavas and melt inclusions from Kilauea.

Combined with our previous assessment that the melt trapped by our melt inclusions had previously lost CO_2 to degassing (i.e. that CO_2/Nb and CO_2/Ba are likely a minimum constraint on the source composition), the observation that our melt inclusions have CO_2/Nb and CO_2/Ba contents intermediate between the alkali olivine basalt and basanite ranges is consistent with the conclusion that the volatile content of the source material from Haleakala is enriched in volatiles relative to the source of shield-stage melts. However, it is not possible to determine the original CO_2 content of the melt. If, as in the case for H_2O/Ce, the melt inclusions from Kilauea have a similar CO_2/Nb to that predicted by Dixon et al., (1997) for North Arch alkali olivine basalts while the undegassed CO_2/Nb ratio for melt inclusions from Haleakala is closer to that of the North Arch basanites and nephelinites, then the CO_2 content of the melt would have to be higher than our estimate for the primary melt by a factor of ~2 (i.e. 1.4 wt% instead of 0.7 wt% CO_2 in the primary melt). However, this is not consistent with the similarity between the CO_2/Ba ratio that we observe for Haleakala melt inclusions and the CO_2/Ba ratios of EPR lavas and melt inclusions from Kilauea with both groups having been affected by degassing.

The conclusion that melt inclusions from Haleakala have higher CO_2/Nb ratios than melt inclusions from Kilauea is consistent with melting of a CO_2-rich source material. However, the elevated CO_2/Nb ratio could also be explained by increased volatile solubility as a function of melt composition and pressure. CO_2 is significantly more soluble in alkaline melts than in tholeiitic melts (Dixon et al., 1995; 1997). Thus, the conditions present at Haleakala (alkaline melts; deep fractionation) permit fluid-saturated melts to have a higher CO_2 concentration than is possible at the conditions at Kilauea (relatively silicic melts; shallow fractionation), and there is insufficient evidence to reject the hypothesis that the CO_2/Nb ratio that we observe is controlled by the limit of

shallow degassing and fractional crystallization in favor of an alternative hypothesis that the elevated CO_2/Nb ratio at Haleakala is the result of melting a volatile-enriched source.

CO_2 in silica-undersaturated melts

Experimental evidence suggests that low-silica alkalic OIBs, such as those erupted at Haleakala, can be potentially derived by partial melting of a carbonated ultramafic source material (Edgar, 1987; Hémond et al., 1994; Dasgupta et al., 2007). Moreover, the major element compositions of the samples analyzed in this study suggest the influence of a CO_2-rich primary melt and mantle source. To evaluate the possibility that a carbonated mantle source was melted to produce low-silica melts at Haleakala, we compared the silica contents of our calculated melts to a compilation of experimental data (Dasgupta, 2004; Dasgupta et al., 2010; Dasgupta et al., 2013). The CO_2 concentrations of melts produced by partial melting of a carbonated peridotite source are negatively correlated with the SiO_2 concentration of the melt produced (Figure 8). This suggests that the primary melt that fractionated to produce the olivine-hosted melt inclusions analyzed in this study, which is calculated to contain 44 wt% SiO_2, would have contained ~5-10 wt% CO_2 given melting conditions similar to those in the experiments.

We used the Ba concentrations of our melt inclusions and an assumed primary CO_2/Ba of 48.3 as reported by Hauri et al. (2018) to estimate the amount of CO_2 present in an undegassed primary melt. Calculated CO_2 concentrations range from 1-2 wt%, which is significantly less than the 2-10 wt% CO_2 which would be present based on the observed correlation of CO_2 and SiO_2 concentrations in the experimental melts (Figure 8). This result indicates that either 1) primary melts below Haleakala contain only 20-50% of the CO_2 that was in the experimentally-derived melts or 2) the assumed mantle CO_2/Ba ratio used for the calculation does not describe the mantle source associated with Haleakala's post-shield volcanism. As discussed by Rosenthal et al. (2016), mineral/melt portioning of CO_2 likely depends on melt composition, and it is possible that the CO_2 concentrations in melts used by Hauri et al. (2018) to estimate the source CO_2/Ba ratio may not be appropriate for melts from Haleakala, which are likely more alkaline than those considered by Hauri et al. (2018).

An alternative possibility is that the melt inclusions originally trapped a more CO_2-rich melt, but lost CO_2 by systematic decrepitation as a result of inclusion overpressure during ascent to shallower depths in the lithosphere. This process has been invoked to explain why volatile-melt saturation pressures calculated from melt inclusions tend to systematically underestimate saturation pressures calculated from pyroxene thermobarometry (Maclennan et al., 2017). Without additional information, this possibility is difficult to assess depending on the extent to which decrepitation features, such as "haloes" of melt and fluid inclusions (e.g. Sterner et al., 1995) or radial fractures surrounding melt inclusions, are able to anneal following decrepitation. However, as described above, volatile-melt saturation pressures calculated in this study are consistent with independently-calculated pressures from pyroxene thermobarometry (Hammer et al., 2016). This suggests that the melt inclusions in this study have not lost a significant amount of CO_2 due to decrepitation, and the discrepancy that we observe between the CO_2 concentrations of melts from experimental carbonated peridotite and our results are due to degassing before melt inclusions were trapped.

Implications for the evolution of Hawaiian volcanism

The volatile and trace element concentrations obtained from olivine-hosted melt inclusions in this study indicate that the source material from Haleakala may be enriched in H_2O and CO_2 relative to source regions of the shield stage. This is consistent with isotopic evidence (Clague & Sherrod, 2014; Phillips et al., 2016), which suggests that the composition of post-shield stage melts from Haleakala are transitional between the shield and rejuvenated stage source compositions. This scenario requires a geodynamic mechanism which produces high-degree melting of isotopically-depleted and potentially volatile-poor mantle material beneath the hotspot, superseded by low-degree melting of an isotopically-enriched and potentially more volatile-rich material downstream of the hotspot.

In order to understand the potential geodynamic mechanisms, we further analyze the predictions of a published geodynamic model (Ballmer et al., 2011) of flow and melting beneath a hotspot. In this model, upwelling mantle material with a buoyancy flux similar to that of the Hawaiian Plume rises and ponds beneath the lithosphere and

sustains partial melting of (and melt extraction from) a composite source (80% depleted peridotite; 15% enriched peridotite; 5% pyroxenite) (for details, see Ballmer et al (2011)). This and similar models of plume-lithosphere interaction (e.g., Farnetani and Hofmann, 2010; Ribe and Christensen, 1999) beneath a fast-moving plate provide robust predictions of the pathways of mantle material that eventually melt in different parts of the hotspot melting zone. In all these models, melting beneath the main-shield is dominated by high-degree melting (up to ~10%) of a mostly depleted (and hence volatile-poor) source, consistent with observations.

The models by Ballmer et al. (2011) further predict that a composite source feeds post-shield volcanism. The mantle melting zone at the relevant location (100~150 km downstream of the hotspot) is subdivided into a shallow (120~140 km depth) and a deep (150~170 km depth) melting zone (Figure 9). In the former, mostly depleted peridotite that has already undergone melting in the main-shield zone continues to melt because of further decompression, reaching high degrees of melting F of 6%~9%. In the latter, mostly enriched peridotite that bypassed the main-shield melting zone undergoes magmatism at $F < 1\%$. This material is predicted to have bypassed the main-shield melting zone because it originates from the periphery of the plume conduit at a distance of ~40 km from the center. It melts as being supported by the tail end of plume-related upwelling, i.e. where the plume finishes curving around to pond at the base of the lithosphere, and the related decompression is just sufficient to allow low-degree melting of enriched heterogeneity. In contrast to that of the post-shield, models predict that the origin of rejuvenated-stage volcanism is due to secondary small-scale convection that occurs as a thermal-boundary layer instability in the hot plume pancake (also see Figure 9).

The above scenario is consistent with our geochemical data assuming that the deep post-shield melting zone is sampled preferentially compared to the shallow post-shield melting zone. Such a preferential sampling may be due to differences in melt extraction between the two zones. For example, the dihedral angle decreases with increasing volatile content (e.g. Minarik & Watson, 1995), favoring extraction of volatile-rich magmas (Keller & Katz, 2016). Also, volatile-rich magmas are less dense and less viscous, and hence ascend more readily through the lithosphere compared to

volatile-depleted magmas. Along these lines, the geochemical data points to volatile enrichment of the domain which feeds into the deep post-shield melting zone (see white dashed line in Figure 9). According to our geodynamic-flow predictions, this domain is a sheath around the hottest part of the plume conduit at a distance of ~40 km from its center, consistent with volatile transport from the center towards the periphery due to deep melting and related hybridization as proposed by Dixon et al. (2001; 2008). Such an origin from the periphery instead of the center of the plume conduit may reconcile the difference in terms of isotopic composition between the post-shield (less enriched) and the main-shield stage (more enriched).

An alternative explanation is that the source of the Hawaiian hotspot volcanism varies through time, and hence as a function of distance from Kilauea. Such a behavior might be due to pulsations of a thermochemical plume (Lin and van Keken, 2005; Kumagai et al., 2008; Ballmer et al., 2013). This hypothesis can be tested by comparing melt inclusions from different shields, or from different post-shields, along the Hawaiian Islands. However, according to geodynamic models, which consider a uniform distribution of chemical heterogeneity (e.g. Figure 9), temporal variations in source composition are not required. The predicted differences in terms of the paths of materials that feed into the main-shield vs. post-shield melting zones are sufficient to explain the observed differences in terms of primary-melt volatile compositions.

Conclusions

We analyzed olivine-host inclusions from Haleakala volcano (Hawaii) to estimate the pre-eruptive volatile content and melting and crystallization conditions at the periphery of the Hawaiian plume. Melt inclusions record evidence of volatile-saturated, polybaric fractional crystallization starting at pressures of 5-7 kbar. We estimate that the primary melt contains approximately 400 ppm Cl, 1500 ppm S, 7000 ppm H_2O, and 7000 ppm CO_2, but note that the CO_2 concentration that we estimate has likely been significantly affected by degassing of CO_2 before melt inclusion entrapment and therefore reflects a minimum estimate.

Melt inclusions from Haleakala have H_2O/Ce and CO_2/Nb ratios significantly higher than melt inclusions from Kilauea and EPR lavas, and these observations suggest

that melts from Haleakala's post-shield stage are derived from a more H_2O- and CO_2-rich melt source than the shield stage or Pacific ambient mantle. This suggests that the composition of post-shield melts from Haleakala are transitional between an isotopically enriched, volatile-poor shield component and an isotopically depleted, volatile-rich rejuvenated component. According to geodynamic models, the best candidate for the origin of the volatile-rich post-shield lavas is a zone of low-degree (<1%) melting of enriched material at 150~170 km depth and 100~150 km downstream of the hotspot, which is fed by material from the periphery of the plume conduit that bypassed the main-shield melting zone.

Acknowledgements

This work was supported by National Science Foundation grants EAR 1802012 and OCE 1756349 to EG, EAR-1624589 and OCE-1634211 to RJB, and a Geological Society of America graduate student research grant to LRM. Samples were collected under the study HALE-00134 and permit HALE-2016-SVI-0004 of the Haleakala National Park, United States Department of the Interior, National Park Services. There authors are grateful for the field support by the staff of the Haleakala National Park. The authors wish to thank Brian Monteleone for assistance with SIMS analyses, Jay Thomas and Will Nachlas for assistance with EPMA, and Luca Fedele and Eszter Sendula for assistance with LA-ICP-MS analyses.

References

Abouchami, W., Hoffmann, A.W., Galer, S.J.G., Frey, F.A., Eisele, J., Feigenson, M. (2005) "Lead isotopes reveal bilateral asymmetry and vertical continuity in the Hawaiian mantle plume," Nature, 434, 851-856.

Anderson, A.T. and Brown, G.G. (1993) "CO_2 contents and formation pressures of some Kilauean melt inclusions." American Mineralogist, 78, 794-803.

Ballmer, M.D., Ito, G., van Hunen, J., Tackley, P.J. (2011) "Spatial and temporal variability in Hawaiian hotspot volcanism induced by small-scale convection," Nature Geoscience, 4, 457-460.

Ballmer, M.D., Ito, G., Wolfe, D.J., Solomon, S.C. (2013) "Double layering of a thermochemical plume in the upper mantle beneath Hawaii," Earth and Planetary Science Letters, 376, 155-164.

Bergmanis, E.C., Sinton, J.M., Trusdell, F.A. (2000) "Rejuvenated volcanism along the southwest rift zone, East Maui, Hawai`I," Bulletin of Volcanology, 62, 4-5, 239-255.

Bianco, T.A., Ito, G., Becker, J.M., Garcia, M.O. (2005) "Secondary Hawaiian volcanism formed by flexural arch decompression," 6, 8, 1-24.

Bizimis, M., Salters, V.J.M., Garcia, M.O., Norman, M.D. (2013) "The composition and distribution of the rejuvenated component across the Hawaiian plume: Hf-Nd-Sr-Pb isotope systematics of Kaula lavas and pyroxenite xenoliths," Geochemistry, Geophysics, Geosystems, 14, 10, 4458-4478.

Blichert-Toft, J., Weis, D., Maerschalk, C., Agranier, A., Albarède, F. (2003) "Hawaiian hot spot dynamics as inferred from the Hf and Pb isotope evolution of Mauna Kea volcano," Geochemistry Geophysics Geosystems, 4, 2, 1-27.

Bodnar, R.J., Student, J.J. (2006) "Melt inclusions in plutonic rocks: Petrography and microthermometry" In Melt Inclusions in Plutonic Rocks (J. D. Webster, ed.), Mineral. Assoc. Canada, Short Course 36, 1-26.

Brounce, M., Stolper, E., Eiler, J. (2017) "Redox variations in Mauna Kea lavas, the oxygen fugacity of the Hawaiian plume, and the role of volcanic gases in Earth's oxygenation," PNAS, 114, 34, 8997–9002.

Canil, D. (2002) “Vanadium in peridotites, mantle redox and tectonic environments: Archean to present,” Earth and Planetary Science Letters, 195, 75-90.

Chatterjee, N., Bhattacharji, S., Fein, C. (2005) “Depth of alkalic magma reservoirs below Kolekole cinder cone,Southwest rift zone, East Maui, Hawaii,” Journal of Volcanology and Geothermal Research, 145, 1-22.

Chen, C.-Y., Frey, F.A., Carcia, M.O., Dalyrimple, G.B., Hart, S.R. (1991) “The tholeiite to alkalic basalt transition at Haleakala Volcano, Maui, Hawaii,” Contributions to Mineralogy and Petrology, 106, 183-200.

Clague, D.A., Dalrymple, G.B. (1987) “The Hawaiian-Emperor Volcanic Chain.” United States Geologic Survey Professional Paper, 1350, 5-54.

Clague, D.A., Sherrod, D.R. (2014) “Growth and Degradation of Hawaiian Volcanoes,” U.S. Geological Survey Professional Paper 1801, 97-146.

Danyushevsky L.V., McNeill, A.W., and Sobolev, A.V. (2002) Experimental and petrological studies of melt inclusions in phenocrysts from mantle-derived magmas: an overview of techniques, advantages and complications. Chemical Geology, 183, 5-24.

Danyushevsky, L.V., Plechov, P. (2011) Petrolog3: Integrated software for modeling crystallization processes, Geochemistry, Geophysics, Geosystems, 12, 7, 32 p.

Dasgupta, R., Hirschmann, M.M., Withers, A.C. (2004) “Deep global cycling of carbon constrained by the solidus of anhydrous, carbonated eclogite under upper mantle conditions,” Earth and Planetary Science Letters, 227, 73-85.

Dasgupta, R., Hirschmann, M.M., Smith, N.D. (2007) “Partial Melting Experiments of Peridotite + CO+ at 3 GPa and Genesis of Alkalic Ocean Island Basalts,” Journal of Petrology, 48, 11, p 2093-2124.

Dasgupta, R., Mallik, A., Tsuno, K., Withers, A.C., Hirth, G., Hirschmann, M.M. (2013) “Carbon-dioxide-rich silicate melt in the Earth’s upper mantle,” Nature Letter, 493, 10, p 211-216.

Dasgupta, R., Hirschmann, M.M. (2010) “The deep carbon cycle and melting in Earth's interior” Earth and Planetary Science Letters, 298, 1-13.

Dixon, J.E., Stolper, E.M., Holloway, J.R. (1995) “An experimental study of water and carbon dioxide solubilities in mid-ocean ridge basaltic liquids. Part I: Calibration and solubility models,” Journal of Petrology, 36, 1607-1631.

Dixon, J.E., Clague, D.A. (2001) Volatiles in basaltic glasses from Loihi seamount, Hawaii: evidence for a relatively dry plume component, 42, 3, 627-654.

Dixon, J.E., Clague, D.A., Wallace, P., Poreda, RR. (1997) Volatiles in Alkalic Basalts from the North Arch Volcanic Field, Hawaii: Extensive Degassing of Deep Submarine-erupted Alkalic Series Lavas, Journal of Petrology, 38, 7, 911-939.

Dixon, J., Clague, D.A., Cousens, B., Monsalve, M.L., Uhl, J. (2008) Carbonatite and silicate melt metasomatism of the mantle surrounding the Hawaiian plume: Evidence from volatiles, trace elements, and radiogenic isotopes in rejuvenated-stage lavas from Niihau, Hawaii, Geochemistry Geophysics Geosystems, 9, 9, 34 p.

Edgar, A.D. (1987) “The genesis of alkaline magmas with emphasis on their source regions: inferences from experimental studies,” Eds. Fitton, J.G., Upton, B.G.J., Alkaline Igneous Rocks, Geological Society Special Publication No. 30, 29-52.

Ford, C.E., Russell, D.G., Craven, J.A., and Fisk, M.R. (1983). Olivine-liquid equilibria; temperature, pressure and composition dependence of the crystal/liquid cation partition coefficients for Mg, Fe2+, Ca and Mn. Journal of Petrology 24, 256-265.

French, S.W., Romanowicz, B. (2015) “Broad plumes rooted at the base of the Earth’s mantle beneath major hotspots” Nature Letter, 525, 95-99.

Frey, F.A., Wise, W.S., Garcia, M.O., West, H., Kwon, S.-T., Kennedy, A. “Evolution of Mauna Kea Volcano, Hawaii: Petrologic and Geochemical Constraints on Postshield Volcanism,” Journal of Geophysical Research, 95, B2, 1270-1300.

Garcia, M.O., Swinnard, L., Weis, D., Greene, A.R., Tagami, T, Sano, H., Gandy, C.E. (2010) “Petrology, Geochemistry and Geochronology of Kaua‘i Lavas over 4.5 Myr: Implications for the Origin of Rejuvenated Volcanism and the Evolution of the Hawaiian Plume,” Journal of Petrology, 51, 7, 1507-1540.

Ghiorso, M.S., Sack, R.O. (1994) “Chemical Mass Transfer in Magmatic Processes. IV. A Revised and Internally Consistent Thermodynamic Model for the Interpolation and Extrapolation of Liquid-Solid Equilibria in Magmatic Systems at Elevated

Temperatures and Pressures," Contributions to Mineralogy and Petrology, 119, 197-212.

Hammer, J., Jacob, S., Welsch, B., Hellebrand, E., Sinton, J. (2016) "Clinopyroxene in postshield Haleakala ankaramite: 1. Efficacy of thermobarometry," 171, 7, 1-23.

Hauri, E.H. (1996) "Major element variability in the Hawaiian mantle plume," Nature, 382, 415-419.

Hauri, E.H., Maclennan, J., McKenzie, D., Gronvold, K., Oskarsson, N., Shimizu, N. (2018) "CO_2 content beneath northern Iceland and the variability of mantle carbon," Geology, 46, 1, p 55-58.

Hémond, C., Devey, C.W., Chauvel, C. (1994) "Source compositions and melting processes in the Society and Austral plumes (South Pacific Ocean): Element and isotope (Sr, Nd, Pb, Th) geochemistry," Chemical Geology, 115, 7-45.

Hofmann, A.H., Farnetani, C.G. (2013) "Two views of Hawaiian plume structure," Geochemistry Geophysics Geosystems, 14, 12, 5308-5322.

Hofmann, A.W., Jochum, K.P. (1996) "Source characteristics derived from very incompatible trace elements in Mauna Loa and Mauna Kea basalts, Hawaii Scientific Drilling Project," Journal of Geophysical Research, 101, B5, 11831-11839.

Iacono-Marziano, G., Morizet, Y., Le Trong, E., Gaillard, F. (2012) New experimental data and semi-empirical parameterization of H_2O–CO_2 solubility in mafic melts, Geochimica et Cosmochimica Acta, 97, 1-23.

Ito, G., Mahoney, J.J. (2005) "Flow and melting of a heterogeneous mantle:2. Implications for a chemically nonlayered mantle," Earth and Planetary Science Letters, 230, 47-63.

Johnson, D.M., Hooper P.R., and Conrey, R.M. (1999) XRF Analysis of Rocks and Minerals for Major and Trace Elements on a Single Low Dilution Li-tetraborate Fused Bead, Advances in X-ray Analysis, 41, 843-867.

Jones, T.D., Davies, D.R., Campbell, I.H., Iaffaldano, G., Yaxley, G., Kramer, S.C., Wilson, C.R. (2017) "The concurrent emergence and causes of double volcanic hotspot tracks on the Pacific plate," Nature, 545, 472-476.

Kirkpatrick, S., Gelatt, Jr., C.D., Vecchi, M.P. (1983) “Optimization by Simulated Annealing,” Science, 220, 4598, 671-680.

Keller, T., Katz, R.F. (2016) “The Role of Volatiles in Reactive Melt Transport in the Asthenosphere,” Journal of Petrology, 57, 6, 1073-1108.

Lamadrid, H.M., Moore, L.R., Moncada, D., Rimstidt, J.D., Burruss, R.C., Bodnar, R.J. (2017) “Reassessment of the Raman CO_2 densimeter,” Chemical Geology, 450, 210-222.

Lange, R.A., Carmichael, I.S.E. (1990) “Thermodynamic properties of silicate liquids with emphasis on density, thermal expansion, and compressibility.” Reviews in Mineralogy, 24, 25-59.

Lee, C-T.A., Luffi, P., Plank, T., Dalton, H., Leeman, W.P. (2009) “Constraints on the depths and temperatures of basaltic magma generation on Earthand other terrestrial planets using new thermobarometers for mafic magmas,” Earth and Planetary Science Letters, 279, 20-33.

Liu, M., Chase, C.G. (1991) “Evolution of Hawaiian basalts: a hotspot melting model,” Earth and Planetary Science Letters, 104, 151-165.

Lloyd, A.S., Plank, T., Ruprecht, P., Hauri, E.H., and Rose, W. (2013) “Volatile loss from melt inclusions in pyroclasts of differing sizes,” Contributions to Mineralogy and Petrology, 165, 1, 129-153.

Maclennan, J. (2017) “Bubble formation and decrepitation control the CO2 content of olivine-hosted melt inclusions,” Geochemistry Geophysics Geosystems, 18, 2, 597-616.

McDonough, W.F., Sun, S.-s. (1995) “The composition of the Earth,” Chemical Geology, 120, 223-253.

Metropolis, N., Rosenbluth, A.W., Rosenbluth, M.N., Teller, A.H. (1953) “Equation of State Calculations by Fast Computing Machines,” Journal of Chemical Physics, 21, 1087-1092.

Michael, P. (1995) “Regionally distinctive sources of depleted MORB: Evidence from trace elements and H_2O,” Earth and Planetary Science Letters, 131, 301-320.

Minarik, W.G., Watson, E.B. (1995) “Interconnectivity of carbonate melt at low melt fraction,” Earth and Planetary Science Letters, 133, 423-437.

Moore, L.R., Gazel, E., Tuohy, R., Lloyd, A.S., Esposito, R., Steele-MacInnis, M., Hauri, E.H., Wallace, P.J., Plank, T., Bodnar, R.J. (2015) Bubbles matter: An assessment of the contribution of vapor bubbles to melt inclusion volatile budgets, American Mineralogist, 100, 806-823.

Moore, L.R., Mironov, N., Portnyagin, M., Gazel, E., Bodnar, R.J. (2018) "Volatile contents of primitive bubble-bearing melt inclusions fromKlyuchevskoy volcano, Kamchatka: Comparison of volatile contentsdetermined by mass-balance versus experimental homogenization," Journal of Volcanology and Geothermal Research, 358, 124-131.

Moussallam, Y., Edmonds, M., Scaillet, B., Peters, N., Gennaro, E., Sides, I., Oppenheimer, C. (2016) "The impact of degassing on the oxidation state of basaltic magmas: A case study of Kilauea volcano," Earth and Planetary Science Letters, 450, 317-325.

Peterson, D.W., Moore, R.B. (1987) "Geologic history and evolution of geologic concepts, island of Hawaii," U.S. Geological Survey Professional Paper 1350, 149-189

Phillips, E.H., Sims, K.W.W., Sherrod, D.R., Salters, V.J.M., Blusztajn, J., Dulai, H. (2016) "Isotopic constraints on the genesis and evolution of basaniticlavas at Haleakala, Island of Maui, Hawaii," Geochimica et Cosmochimica Acta, 195, 201-225.

Ren, Z-Y., Takahashi, E., Orihashi, Y., Johnson, K.T.M. (2004) "Petrogenesis of Tholeiitic Lavas from the Submarine Hana Ridge, Haleakala Volcano, Hawaii," Journal of Petrology, 45, 10, 2067-2099.

Ren, Z.-Y., Shibata, T., Yoshikawa, M., Johnson, K.T.M., Takahashi, E. (2006) "Isotope compositions of Submarine Hana Ridge Lavas, Haleakala Volcano, Hawaii: Implications for Source Compositions, Melting Process and the Structure of the Hawaiian Plume," 47, 2, 255-275.

Ribe, N.M., Christensen, U.R. (1999) "The dynamical origin of Hawaiian volcanism," Earth and Planetary Science Letters, 171, 517-531.

Roedder, E. (1979) "Origin and significance of magmatic inclusions," Bulletin de Mineralogie, 102, 467-510.

Rosenthal, A., Hauri, E.H., Hirschmann, M.M. (2015) “Experimental determination of C, F, and H partitioning between mantle minerals and carbonated basalt, CO2/Ba and CO2/Nb systematics of partial melting, and the CO2 contents of basaltic source regions,” Earth and Planetary Science Letters, 412, 77-87.

Saal, A.E., Hauri, E.H., Langmuir, C., Perfit, M.R. (2002) “Vapour undersaturation in primitivemid-ocean-ridge basalt and thevolatile content of Earth’s upper mantle,” Nature, 419, 451-455.

Sherrod, D.R., Nishimitsu, Y., Tagami, T. (2003) “New K-Ar ages and the geologic evidence against rejuvenated-stage volcanism at Haleakala, East Maui, a postshield-stage volcano of the Hawaiian island chain,” GSA Bulletin, 115, 6, 683-694.

Sherrod, D.R., Sinton, J.M., Watkins, S.E., Brunt, K.M. (2007) “Geologic map of the State of Hawai’i,” US Geological Survey Open-File Report, http://pubs.usgs.gov/of/2007/1089/

Shimizu, K., Shimizu, N., Komiya, T., Suzuki, K., Maruyama, S., Tatsumi, Y., (2009) “CO_2-rich komatiitic melt inclusions in Cr-spinels within beach sand from Gorgona Island, Colombia” Earth and Planetary Science Letters, 288, 33–43.

Sides, I.R., Edmonds, M., Maclennan, J., Swanson, D.A., Houghton, B.F. (2014) “Eruption style at Kilauea Volcano in Hawai`i linked to primary melt composition,” Nature Geoscience, 7, 464-469.

Sobolev, A.V., Hofmann, A.W., Jochum, K.P. Kuzman, K.V., Stoll, B. (2011) “A young source for the Hawaiian plume,” 476, 434-437.

Sobolev, A.V., Hofmann, A.W., Sobolev, S.V., Nikogosian, I.K. (2005) An olivine-free mantle source of Hawaiian shield basalts, Nature, 434, 590-597.

Steele-MacInnis M, Esposito R & Bodnar RJ (2011) “Thermodynamic model for the effect of post-entrapment crystallization on the H_2O-CO_2 systematics of volatile-saturated silicate melt inclusions,” Journal of Petrology, 52, 2461-2482.

Sterner, S.M., Hall, D.L., Keppler, H. (1995) “Compositional re-equilibration of fluid inclusions in quartz,” Contributions to Mineralogy and Petrology, 119, 1-15.

Tucker, J.M., Hauri, E.H., Pietruszka, A.J., Garcia, M.O., Marske, J.P., Trusdell, F.A. (2019) “A high carbon content of the Hawaiian mantle fromolivine-hosted melt inclusions,” Geochimica et Cosmochimica Acta, 254, 156-172.

Wagner, T.P., Clague, D.A., Hauri, E.H., Grove, T.L. (1998) “Trace element abundances of high-MgO glasses from Kilauea, Mauna Loa and Haleakala volcanoes, Hawaii,” Contributions to Mineralogy and Petrology, 131, 13-21.

Wallace, P.J., Kamanetsky, V.S., Cervantes, P. (2015) “Melt inclusion CO2 contents, pressures of olivine crystallization, and the problem of shrinkage bubbles,” American Mineralogist, 100, 787-794.

Wanless, V.D., Shaw, A.M. (2012) “Lower crustal crystallization and melt evolution atmid-ocean ridges,” Nature Geoscience, 5, 651-655.

Xu, G., Frey, F.A., Clague, D.A., Weis, D., Beeson, M.H. (2005) “East Molokai and other Kea-trend volcanoes: Magmatic processes and sources as they migrate away from the Hawaiian hot spot” Geochemistry Geophysics Geosystems, 6, 5, 1-28.

Figures

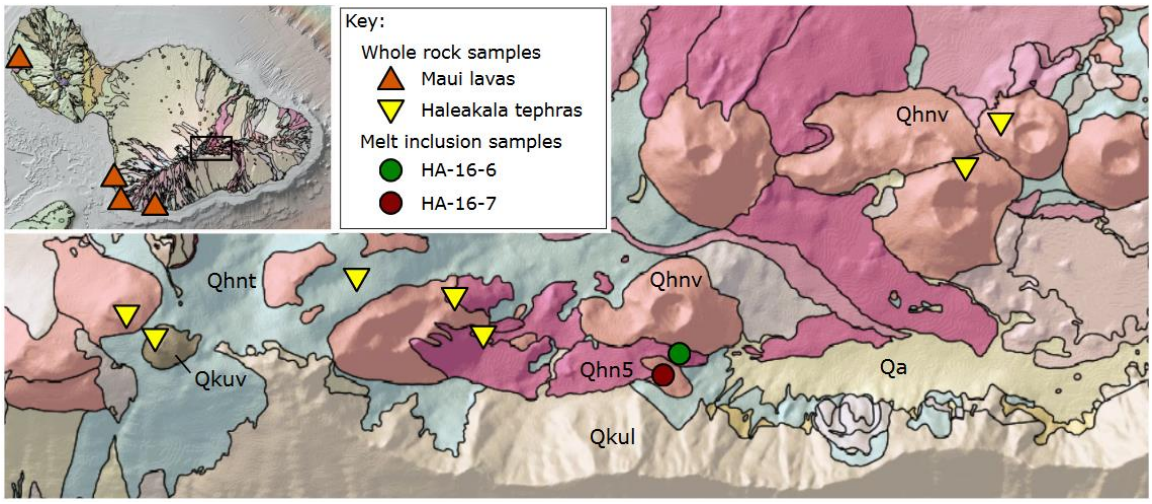

Figure 1: Geologic map of sample locations. Geologic map and lithologic unit abbreviations after Sherrod et al. (2007). Hana volcanics: Qhnt - tephras, Qhnv - vent deposits, Qhn5 – lava flows; Kula volcanics: Qkuv – vent deposits, Qkul – lava flows; Qa: Holocene alluvium. Symbols indicate sample type as in Figure 2.

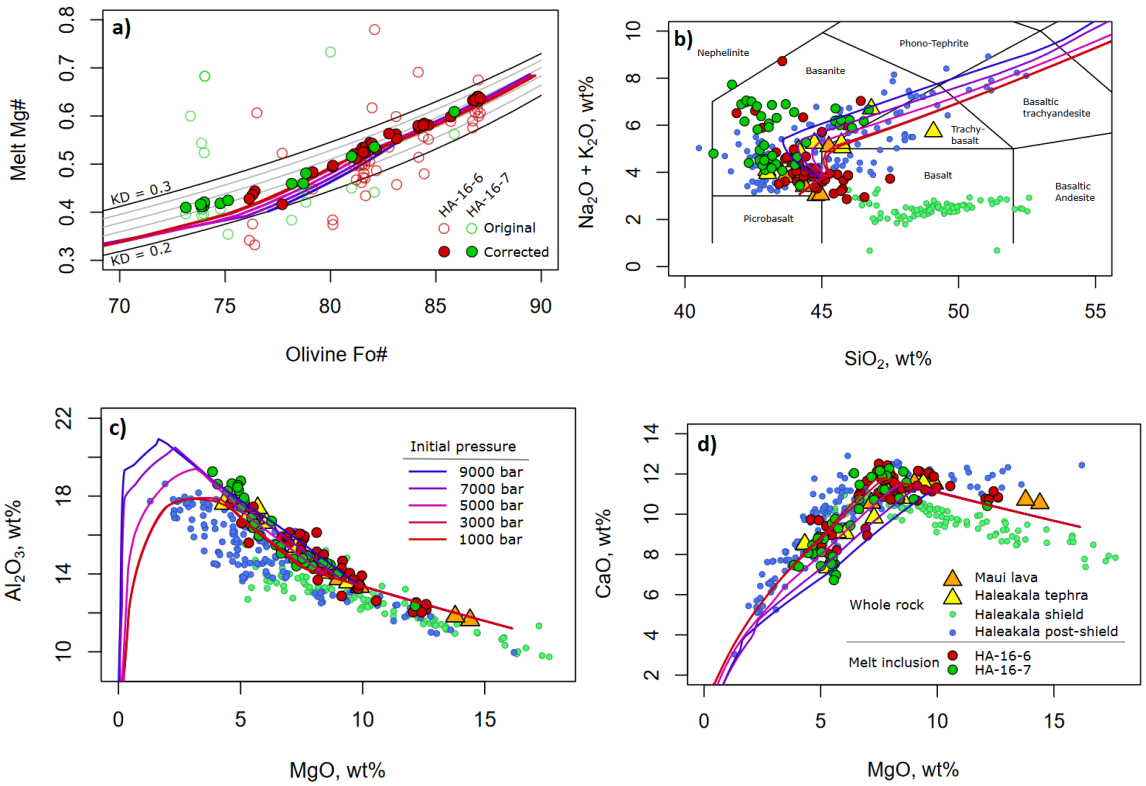

Figure 2: Whole rock and melt inclusion compositions compared with MELTS models. Haleakala shield and post-shield stage whole rock compositions from GeoRoc database (http://georoc.mpch-mainz.gwdg.de/georoc/) are shown for comparison**.**

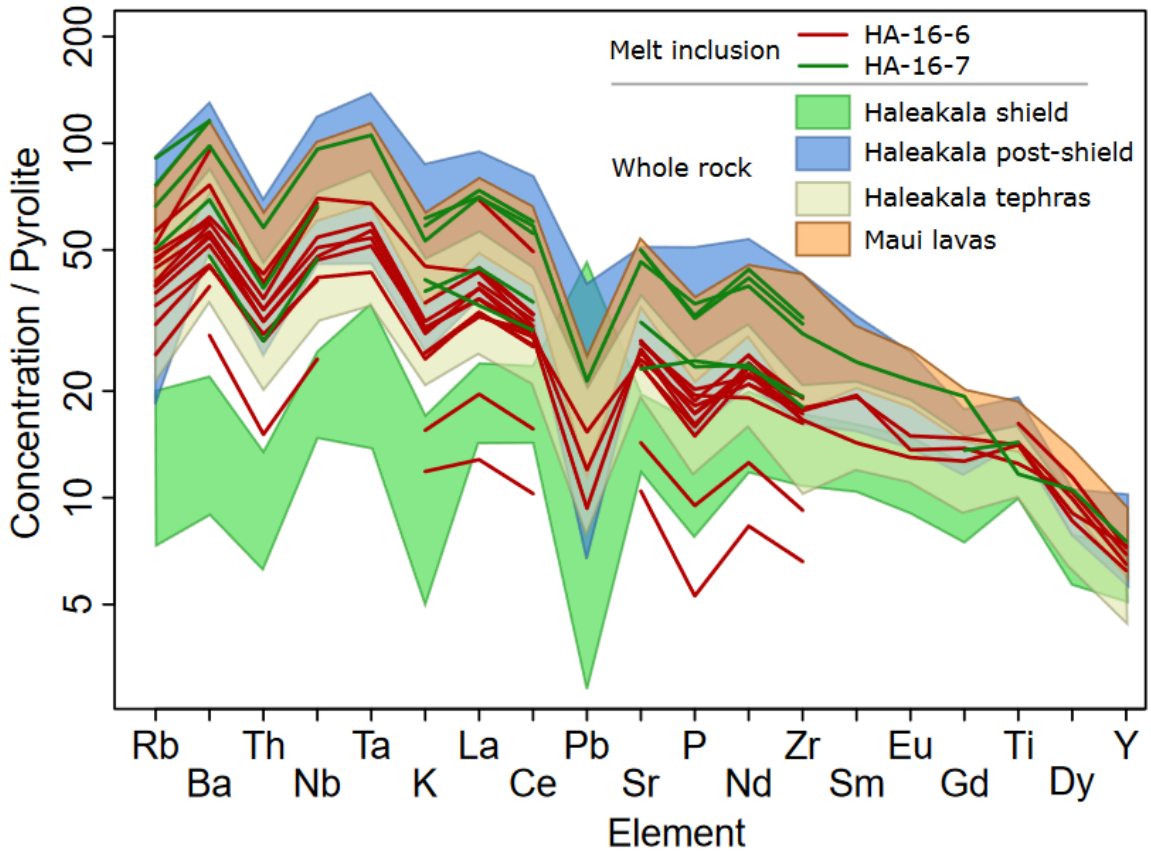

Figure 3: Trace element compositions of whole rock (yellow) and melt inclusions samples HA-16-6 (red lines) and HA-16-7 (green lines) from Haleakala. Shield stage (green) and post-shield stage compositions (blue) compiled from the GeoRoc database are shown for comparison and filtered to show only the interdecile range.

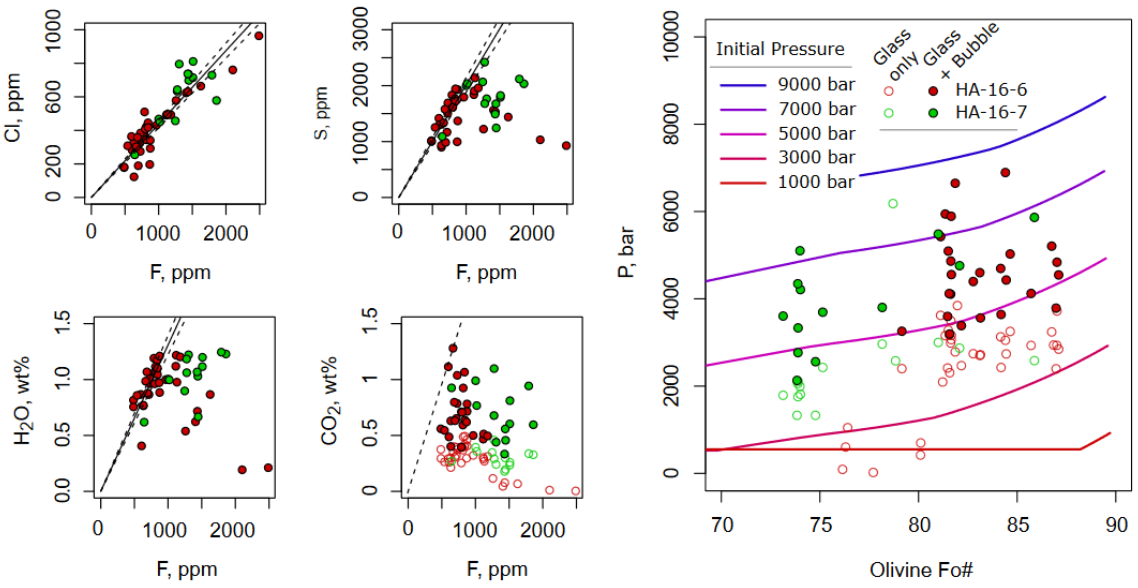

Figure 4: (a) MI volatile concentrations with linear regression of presumably undegassed volatile concentrations indicating fractional crystallization. Light-colored symbols indicate MI glass compositions not corrected to include CO_2 exsolved into bubbles. A representative error bar is shown for CO_2 vs F. (b) Volatile-melt saturation pressures and MI host compositions compared with MELTS model results. Inset shows remaining melt fraction during fractional crystallization. LLD color scale indicates decompression rate as in Figure 2.

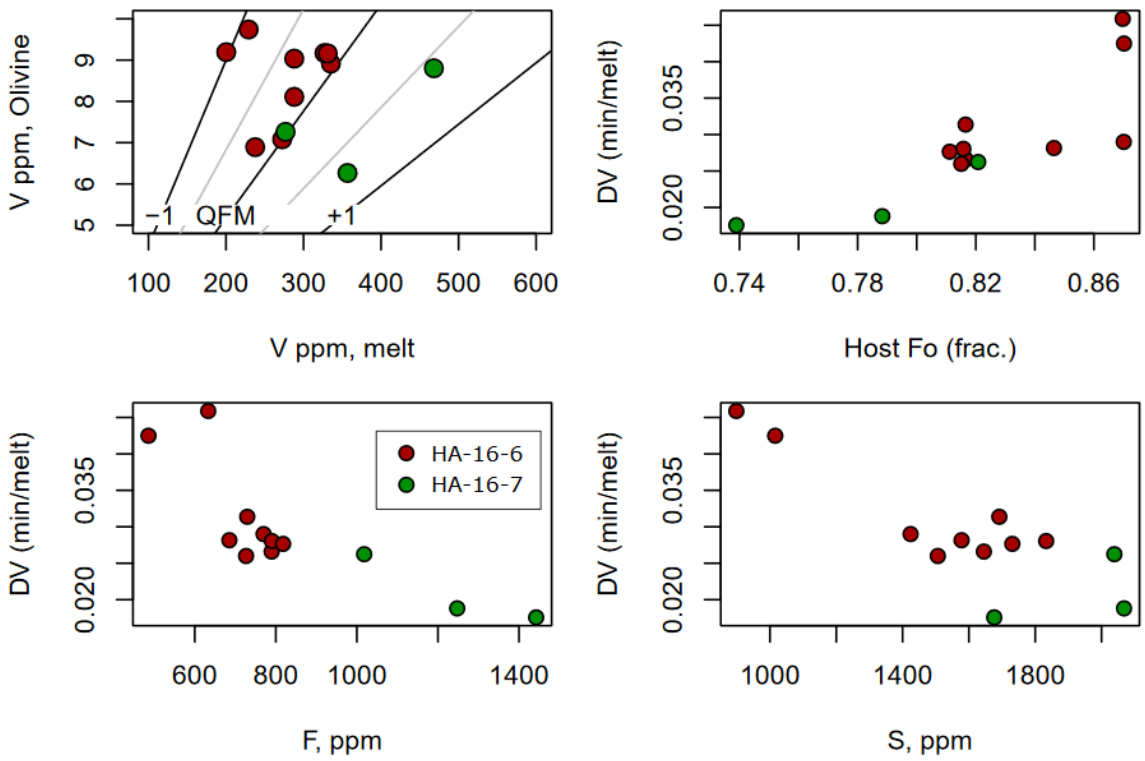

Figure 5: Olivine-melt V partitioning and calculated oxidation state for melt inclusions from Haleakala.

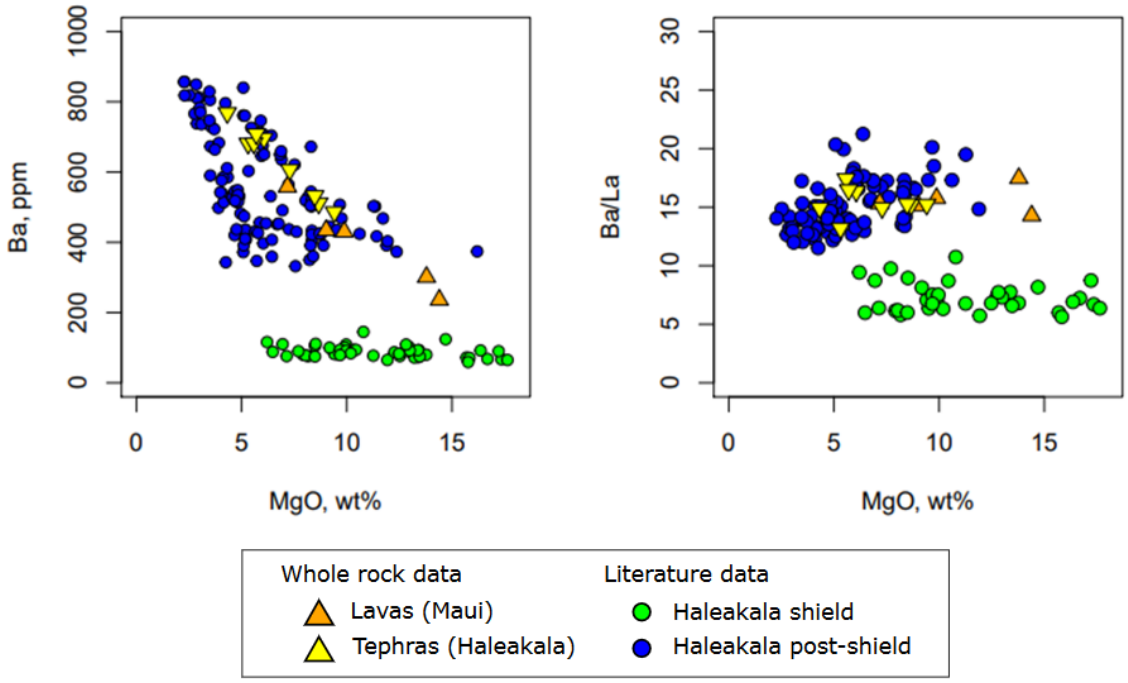

Figure 6: Trace element concentrations in whole rock samples from Maui. Haleakala shield and post-shield stage whole rock compositions from GeoRoc database (http://georoc.mpch-mainz.gwdg.de/georoc/) are shown for comparison.

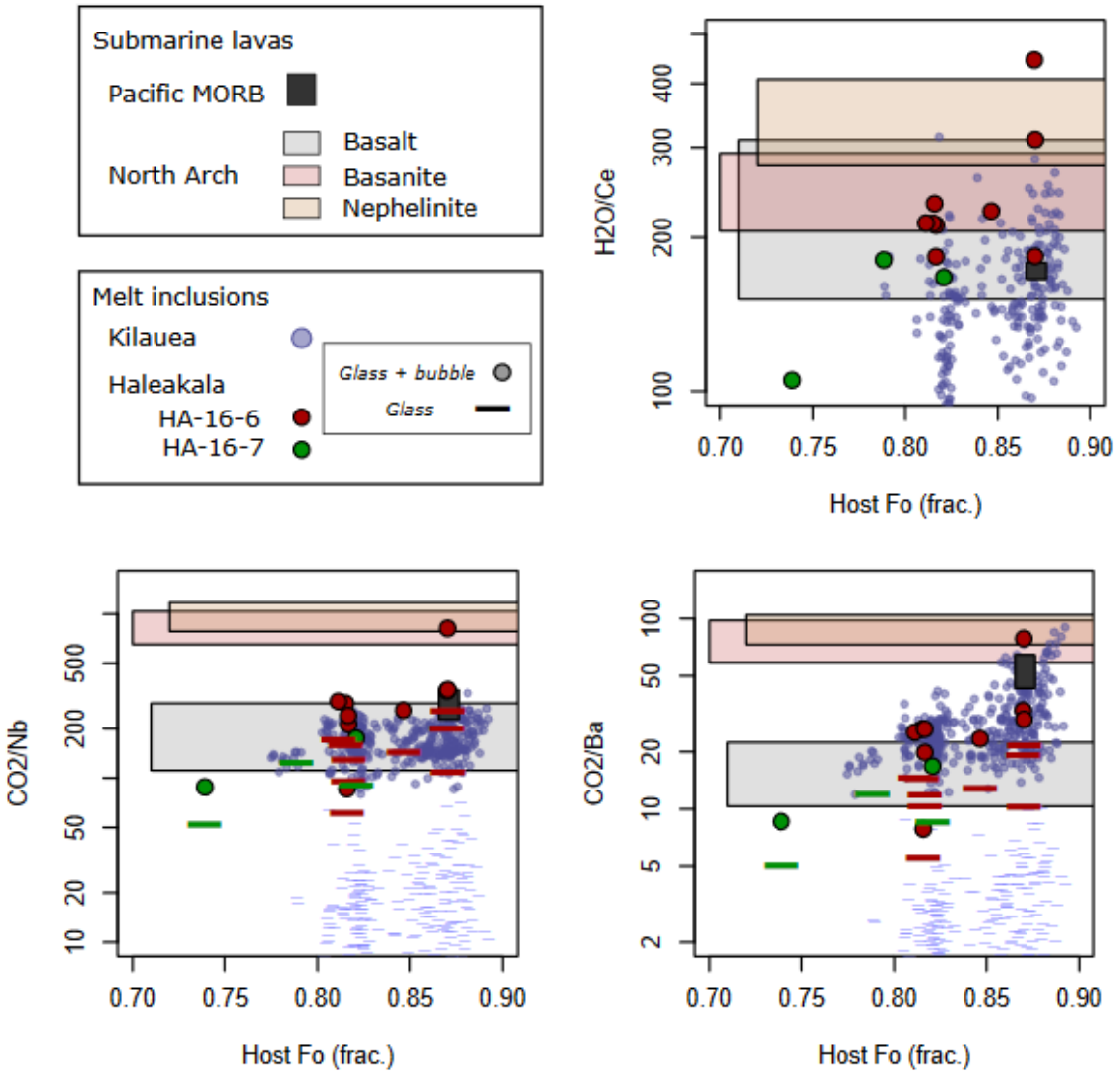

Figure 7: Volatile/light rare earth element ratios of melt inclusions and submarine lavas from Hawaii and Pacific lithosphere. Horizontal lines indicate melt inclusion compositions that have not been corrected to include CO_2 in bubbles. Kilauea melt inclusions from Sides et al. (2014), which have been corrected assuming a contribution of 2000 ppm of additional CO2 from the bubble (Moore et al., 2015), are shown for comparison. Shaded horizontal bars show range of compositions from dredged North Arch lavas reported by Frey et al. (1990) and Dixon et al. (1997) for alkali olivine basalts (gray), basanites (pink), and nephelinites (orange). The dark gray rectangle shows the compositional range of EPR host olivine and melt inclusions reported by Wanless & Shaw (2010) based on the interquartile range of Ce, Nb, Ba, H_2O and host Fo concentrations, and the upper quartile of CO_2 concentrations.

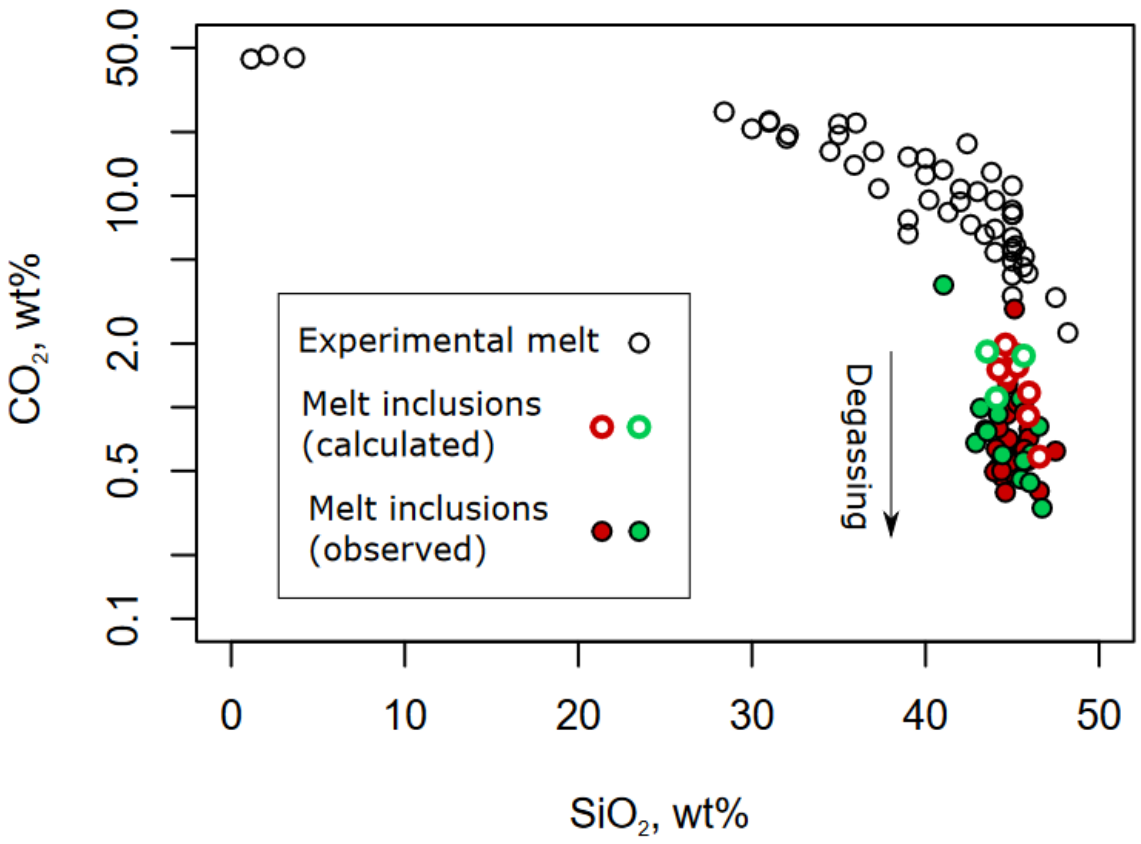

Figure 8: Primary melt CO_2 concentrations calculated from melt inclusions from Haleakala using a primary CO_2/Ba ratio of 48.5 (Hauri et al., 2018) and experimentally-derived melts from carbonated peridotite compiled from Dasgupta (2004), and Dasgupta et al (2007; 2013).

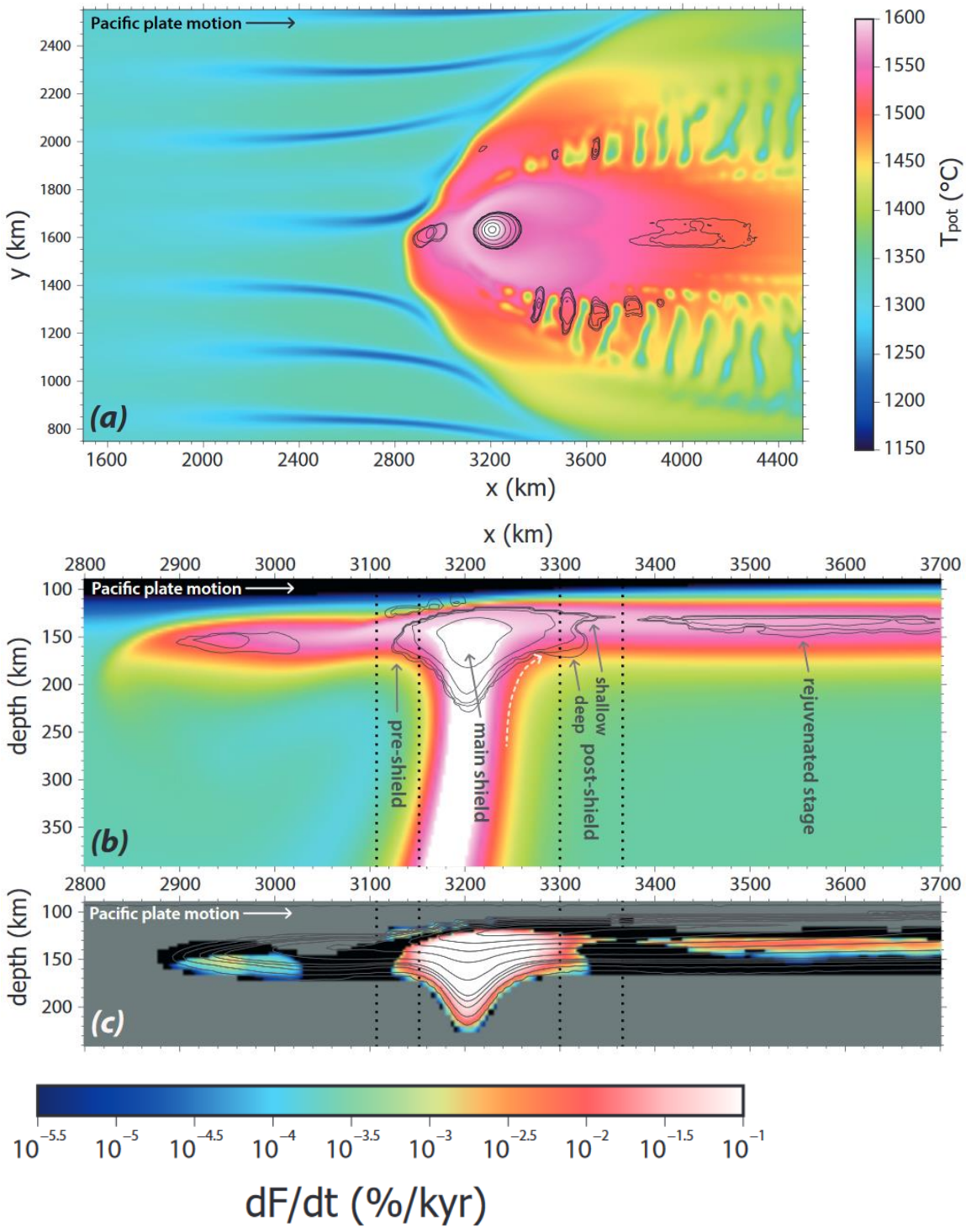

Figure 9: Geodynamic model predictions (model description and detailed results in Ballmer et al., 2011). (a) Horizontal cross-section of potential temperature with contours of melting rate (at $10^{-4.5}$, 10^{-4}, $10^{-3.5}$, 10^{-3}… %/kyr) at 150 km depth. Concentric ellipses mark the hotspot with main-shield and post-shield melting zones in its center, and

towards its right-hand side, respectively. Separate zones of melting may feed rejuvenated-stage and off-axis volcanism. (b) Vertical cross-section of potential temperature (colors) with contours of melting rate (at $10^{-4.5}$, $10^{-3.5}$, $10^{-2.5}$… %/kyr) at y = 1630 km. At 100~150 km downstream of the zone of most intense melting, the model "post-shield" melting zone is divided into a shallow (~130 km depth) and a deep melting zone (~160 km depth). Melting zones are labeled by stage, and separated by dotted lines. White dashed line is a schematic flow-line. (c) Vertical cross-section (at y = 1630 km) of melting rate (colors) with contours of depletion of enriched peridotite (0.01%, 0.1%, 0.4%, 0.7%, 1%, 2%, 4%, 6%, 8%, 10%). In the deep post-shield melting zone at 150~170 km depth, melting occurs at low degrees of melting, i.e. <1%.

Tables

Table 1: Calculated primary melt composition

SiO_2	TiO_2	$Al2O_3$	$Cr2O_3$	FeO	Fe_2O_3	MgO	MnO	CaO	Na_2O	K_2O	H_2O	CO_2
44.18	1.94	11.20	0.06	10.69	2.45	16.12	0.16	9.37	2.36	0.70	0.70	0.70

Oxide concentrations in wt%

Supplementary Methods

Melt inclusion sample preparation and microanalysis

Melt inclusion-bearing olivine phenocrysts were hand-picked under transmitted, cross-polarized light so that the phenocrysts could be identified through a coating of translucent glass. The host phenocrysts were then mounted in a 1-inch diameter epoxy disc and polished to remove the glass coating and to expose the interior of the host crystals. Melt inclusions were selected for microanalysis based on the criteria that they 1) were approximately 25 microns in diameter or larger, 2) contained a homogenous (i.e. not devitrified) glass, and 3) were not intersected by fractures in the crystal or the polished surface of the grain. Phenocrysts found to contain suitable melt inclusions were removed from the epoxy mount using a soldering iron, mounted using CrystalBond 590™ on a 1-inch diameter glass slide, and polished individually.

Raman analyses of melt inclusion bubbles were done using a 514.14 nm laser, a diffraction grating with 1800 grooves/mm, a 400 µm confocal hole, a 150 µm slit, and 3 iterations of a 45-second collection time. In many cases, a mixture of liquid and vapor CO_2 could be seen in the vapor bubble when viewed under the microscope at ambient conditions, so it was necessary to heat the samples during Raman analysis so that the fluid could be analyzed as a single phase. We used a thermoelectric plate to heat the inclusions to 35°C (above the critical temperature for CO_2) and monitored the temperature during Raman analyses using a thermocouple positioned at the edge of each host crystal. Raman spectra were calibrated and checked for drift using a Ne plasma emission lines, and CO_2 densities were calculated from the splitting of the Fermi Diad using the equation of Lamadrid et al. (2017).

After melt inclusions were analyzed using Raman spectroscopy, phenocrysts were individually polished again to expose an area of the glass large enough (~20 microns wide) to be analyzed using secondary ion mass spectrometry (SIMS) and pressed into an indium metal medium in a 1-inch diameter aluminum sample holder provided by the Woods Hole Oceanographic Institute (WHOI). The samples were gold-coated by plasma deposition and melt inclusion glasses were analyzed for volatile elements (CO_2, H_2O, F, S, Cl) using SIMS at WHOI following the method described by Shimizu et al. (2009).

Following SIMS analysis, indium grain mounts were lightly polished using a 0.3 micron alumina grit and a silk pad to remove the gold coating and as much of the pit left by ion rastering as possible. The grain mounts were then carbon-coated and melt inclusion glasses and host olivine grains were analyzed for major elements using electron probe microanalysis at Syracuse University. Analyses were done using a Cameca SXFive electron microprobe using a 15 kV accelerating voltage, and a 10 nA beam with a spot diameter of 5 microns. Na-loss was minimized by analyzing Na first in the detection sequence, and had a negligible effect on analyzed glass compositions based on comparison with basalt standard ALU 519-4-1 included in the sample mount. The host olivine composition was determined by analyzing in two spots adjacent to each melt inclusion and taking the mean.

Finally, the inclusion-bearing grains were transferred from the pressed indium mount into an epoxy mount for LA-ICP-MS analyses. This was necessary for viewing inclusions in transmitted light so that the laser beam could be positioned in the center of the inclusion to maximize the analytical volume during the laser ablation analyses. LA-ICP-MS analyses were done Melt inclusions were analyzed using an Agilent 7500ce ICPMS coupled with a Geolas 193 nm excimer laser ablation system. Samples were analyzed using a 40 mJ energy and a 5 Hz pulse rate, and a 10 ms dwell time for each element. Melt inclusions were analyzed using a variable spot size from 32-60 micron diameter, and host olivines were analyzed using a spot with a 90 micron diameter. Mass spectra were processed using the LazyBoy workbook for Microsoft Excel. Glass compositions were calculated using USGS glass standards BHVO-2g, BCR-2g, and BIR-1g, and olivine compositions were calculated using a San Carlos olivine standard. To check for accuracy, San Carlos olivine and BHVO-2g glass standards were run as unknowns. Using this approach, most calculated trace element concentrations were accurate to within 10% with the exception of Pb, which was accurate to within 20%.